# Modelling vortex-vortex and vortex-boundary interaction

Rhodri Burnett Nelson

DEPARTMENT OF MATHEMATICS
UNIVERSITY COLLEGE LONDON

A THESIS SUBMITTED FOR THE DEGREE OF
DOCTOR OF PHILOSOPHY

SUPERVISOR
Prof. N. R. McDonald

September 2009

I, Rhodri Burnett Nelson, confirm that the work presented in this thesis is my own. Where information has been derived from other sources, I confirm that this has been indicated in the thesis.

SIGNED

# Abstract

The motion of two-dimensional inviscid, incompressible fluid with regions of constant vorticity is studied for three classes of geophysically motivated problem. First, equilibria consisting of point vortices located near a vorticity interface generated by a shear flow are found analytically in the linear (small-amplitude) limit and then numerically for the fully nonlinear problem. The equilibria considered are mainly periodic in nature and it is found that an array of equilibrium shapes exist. Numerical equilibria agree well with those predicted by linear theory when the amplitude of the waves at the interface is small.

The next problem considered is the time-dependent interaction of a point vortex with a single vorticity jump separating regions of opposite signed vorticity on the surface of a sphere. Initially, small amplitude interfacial waves are generated where linear theory is applicable. It is found that a point vortex in a region of same signed vorticity initially moves away from the interface and a point vortex in a region of opposite signed vortex moves towards it. Configurations with weak vortices sufficiently far from the interface then undergo meridional oscillation whilst precessing about the sphere. A vortex at a pole in a region of same sign vorticity is a stable equilibrium whereas in a region of opposite-signed vorticity it is an unstable equilibrium. Numerical computations using contour dynamics confirm these results and nonlinear cases are examined.

Finally, techniques based on conformal mapping and the numerical method of contour dynamics are presented for computing the motion of a finite area patch of constant vorticity on a sphere and on the surface of a cylinder in the presence of impenetrable boundaries. Several examples of impenetrable boundaries are considered including a spherical cap, longitudinal wedge, half-longitudinal wedge, and a thin barrier with one and two gaps in the case of the sphere, and a thin island and 'picket' fence in the case of the cylinder. Finite area patch motion is compared to exact point vortex trajectories and good agreement is found between the point vortex trajectories and the centroid motion of finite area patches when the patch remains close to circular. More exotic motion of the finite area patches on the sphere, particularly in the thin barrier case, is then examined. In the case when background flow owing to a dipole located on the barrier is present, the vortex path is pushed close to one of the barrier edges, leading to vortex shedding and possible splitting and, in certain cases, to a quasi-steady trapped vortex. A family of vortex equilibria bounded between the gap in the thin barrier on a sphere is also computed.

# Acknowledgements

I would first and foremost like to express my heartfelt gratitude to my supervisor, Robb McDonald, for all the help and guidance he has given me throughout my time at UCL. It has been a pleasure to work with him and learn from his expertise, and I thank him for playing a big part in making my time at UCL so enjoyable.

I would like to thank the Geophysical Fluid Dynamics group for the insightful conversations and their input and in particular my predecessor, Alan Hinds, for all his help and suggestions when I began my PhD. I am indebted to the UCL graduate school for their financial assistance that has allowed me to attend some prestigious conferences during my studies and of course, I owe a great deal of gratitude to my funding body, the Natural Environment Research Council. I would also like to thank my fellow PhD students who have created such a pleasant environment at UCL, and in particular the students with whom I began my PhD, Tommy, Jo, Brian and Isidoros. I owe a big thank you to all of the administrative staff who have been so helpful throughout my PhD.

I also wish to warmly acknowledge the support of all of my friends and I would like to thank Guy and Phil for the great holidays during my PhD and Will and Francois for all of the entertainment in and around London.

I have a giant thank you to say to my girlfriend, Chierh, for her patience, kindness and warmth (and for all the great meals that have kept me fit and healthy over the past couple of weeks).

Yn olaf, hoffwn diolch fy teulu; fy Mam, Dad, Brawd, Chwaer ac fy Nain diffoddiedig, am eu cariad a cymorth trwy gydol fy addysg. Hoffwn diolch fy Mam am eu geiriau o cymorth yn y misoedd diweddar.

# Contents

# Chapter 1

# Introduction

The study of two dimensional, inviscid and incompressible flows is an important area of applied mathematics and related scientific fields and has attracted much attention over the years. Modern mathematical modeling of fluid motion dates back to the $18^{th}$ century, the original form of the equations governing inviscid flow being published in an article by Euler entitled *'Principes generaux du mouvement des fluides'* published in *Mémoires de l'Academie des Sciences de Berlin* in 1757. The more general Navier-Stokes equations governing the motion of both inviscid and viscous fluids were later written down in the $19^{th}$ century with major contributions from Claude-Louis Navier and George Gabriel Stokes.

Until recently, literature concerning the modeling of fully three dimensional fluid flows has been scarce, especially when compared to the body of work existing for the two dimensional problem. This is partly due to the difficultly of obtaining exact fully three dimensional solutions and also, from the numerical modeling perspective, the advanced numerical methods and massive computational power required for the

study of large scale three dimensional systems. However, with the development and continued advancement of numerical schemes such as the finite difference (Smith 1985), finite volume (Versteeg and Malalasekra 1995) and finite element methods (Hughes 2003), the speed of modern computers and the ability to parallelize code in a practical manner, the body of research being carried out in such areas is steadily growing.

In the geophysical arena (which has provided the motivation for the problems considered in thesis), some of the leading Navier-Stokes solvers include the Community Climate System Model (http://www.ucar.edu/communications/CCSM/), the MIT general circulation model for atmospheres and oceans (http://mitgcm.org/) and the Nucleus for European Modelling of the Ocean model(http://www.nemo-ocean.eu/). For the aforementioned models, CCSM and NEMO employ a finite difference approach and the MITgcm a finite volume approach. Also, the Imperial College Ocean model (http://amcg.ese.ic.ac.uk/index.php?title=ICOM) is an exciting finite element based ocean model under development at Imperial College London. With the computing power at their disposal, these models are capable of resolving small scale features in large domains which can sometimes span the entire globe. However, the stability of numerical schemes in large aspect ratio domains with dynamics encompassing a range of spatial length-scales is a significant problem (Webster 2006) and it is often required to make various approximations. Common approximations (in atmosphere and ocean models) include assuming the fluid is incompressible and employing the hydrostatic approximation.

Another drawback of general circulation models (GCMs) is that, due to their com-

plexity, the mathematical structure and physical processes involved in the problems under consideration are often 'lost' in the numerical scheme. That is to say, results are often difficult to interpret making such models far less 'intuitive'. Thus, in order to analyse important aspects of the dynamic processes at work in atmospheres and oceans it is often necessary and desirable to cut models down to their 'bare bones'. This allows models to be constructed in much friendlier (but still highly nonlinear and therefore challenging) mathematical frameworks and allows for far easier interpretation of results. Results from these comparatively simpler models can then often help motivate problems to investigate with GCMs and help interpret the results they yield.

However, even in the 2D motion of an inviscid and incompressible fluid governed by the Euler equations, solutions can exhibit a great deal of complexity and are very relevant to the modeling of atmospheres and oceans (Juckes and McIntyre 1987). This thesis will be restricted to the analysis of problems involving such 2D flows.

Flows considered in this thesis all involve finite regions of vorticity surrounded by otherwise irrotational flow. The mathematical formulation governing such flows is stated in chapter 2.1. The study of vortical flows (in 3D as well as 2D) dates back to Helmholtz's seminal paper published in 1858, the English translation of which is *'On integrals of the hydrodynamical equations which express vortex motion'*. Some other important contributors to the area of vortex dynamics include William Thomson (later Lord Kelvin) in the $19^{th}$ century and Philip Saffman in the last century along with many other past and contemporary scientists. Many recent results related to the problems considered in this thesis will be discussed at the beginning of the relevant

chapters. The structure of this thesis is outlined below.

Chapters 2 and 3 concern the analytical derivation and numerical computation of vortex equilibria, mainly in singly-periodic domains. The systems investigated consist of point vortices interacting with a vorticity interface, which in this work is generated by a shear flow. In chapter 2, equilibria will be found in the linear limit of small amplitude oscillations at the interface. This linear approximation facilitates the analytical derivation of equilibria and the purpose of such investigations is two-fold. First, the existence of linear equilibria can often be a good indication of the existence of non-linear equilibria and the shapes they may take. Thus, linear equilibria can motivate and aid the search for the corresponding non-linear equilibria. Second, importantly, linear theory serves as a mechanism with which to verify results of non-linear computations.

In chapter 3 the method of contour dynamics is used to investigate the corresponding non-linear equilibria to those computed in chapter 2. Contour dynamics is a Lagrangian computational method in which the boundaries of vorticity distributions are represented as a number of discrete points. Originally pioneered by Deem and Zabusky (1978), contour dynamics is a highly efficient and accurate method for computing the motion of piecewise constant vorticity distributions. In its original form, the method was restricted to cases in which the distributions of vorticity remained relatively simple. Later, with the development of contour surgery (Dritschel 1989), the method can now be applied to fluid motions of unparalleled complexity. Details of the contour dynamics algorithm in many regimes are presented in Dritschel (1989). During the preparation of this thesis, much effort has been spent adapting a

2D planar contour dynamics algorithm to work on the surface of the unit sphere and on the surface of a unit cylinder ($2\pi$ singly periodic domain). Details on implementing contour dynamics algorithms in these topographies are given in appendix A.

In chapter 4 the time dependent problem of a single point vortex interacting with a vorticity interface on the surface of the sphere is considered. The work of this chapter was presented at *'The Fifth International Conference on Fluid Mechanics'* held in Shanghai in 2007. In the first part of this chapter linear theory valid for small amplitude oscillations at the vorticity interface is used to construct an analytical system of first order differential equations governing the motion of the system. Behaviour of the linear system and the stability of stationary points (for both linear and non-linear regimes) is then considered. Finally, a spherical contour dynamics algorithm is used to examine the non-linear behaviour of the system. Contour dynamics results are verified against linear theory for systems in the linear regime and then the evolution of more non-linear systems explored.

Chapters 5 and 6 consider the motion of point and finite area vortices in bounded domains on the surface of the sphere and in a $2\pi$-singly-periodic domain respectively. Much of the work presented in chapter 5 has been published in Nelson and McDonald (2009a) and Nelson and McDonald (2009b). The work was also presented at the IUTAM Symposium *(150 Years of Vortex Dynamics)* held in the Technical University of Denmark in 2008. In these chapters, a contour dynamics algorithm is used to calculate velocity fields in the domain as if the boundaries are not present. An irrotational velocity field is then sought, such that, when added to the velocity field owing to the 'unbounded' vortex will satisfy the required boundary conditions with

the boundaries present. This method exploits the invariance of Laplace's equation under conformal mapping. Finally, conclusions and some possibilities for future work are discussed in chapter 7.

# Chapter 2

# Point vortex equilibria near a vortical interface: linear theory

Two dimensional distributions of vorticity that remain stationary in a translating or rotating frame of reference have been the subject of much interest in the literature. Such equilibrium distributions represent exact (or possibly numerical) solutions of the two dimensional Euler equations and have been given the name V-states (or vortex crystals). Many of the 'simplest' equilibria consist of specially arranged configurations of singular points of vorticity (known as 'line' or 'point' vortices). Two of the most basic examples of such equilibria include two point vortices of equal but opposite circulations, and two point vortices with equal and same signed circulations. Arranged in the first configuration, the vortices will translate at constant speed in the direction perpendicular to the line segment connecting them. In the latter configuration, the vortices rotate steadily about the centre of their connecting line segment, where the sense and angular velocity of rotation is determined by the magnitude and sense of

their circulations.

The case of two co-rotating vortices is the $N = 2$ case of $N$ identical vortices positioned at the vertices of a regular $N$ sided polygon. Vortices in such a configuration rotate with constant angular velocity given by $\Omega = \Gamma(N-1)/4\pi a^2$, where $\Gamma$ is the circulation of the vortices and $a$ is the radius of the circle connecting them (Kelvin 1878; Thomson 1883). The stability of such systems is considered in Saffman (1992). Many more 'exotic' equilibria consisting of $N$ point vortices have since been identified and examined; a range of both symmetric and asymmetric examples is presented in Aref (2007).

It is also of interest to determine point vortex equilibria in geometries other than the planar geometry: from a geophysical perspective the surface of a sphere and the singly periodic domain (or, equivalently, the surface of a cylinder) are of particular interest. For example, when considering large scale vortical structures in a planet's atmosphere or ocean, the curvature and azimuthal periodicity of the sphere can play an important role in the dynamics of the system. In systems where periodic generation of vortices occurs, for example, vortices generated from air flow over topography such as an island (DeFelice et al. 2000), it is appropriate to model the problem in a periodic strip. The observations discussed in DeFelice et al. (2000) concern the sighting of a Karman vortex street over the Southeast Pacific Ocean. Such structures are classic examples of the double rows of staggered vortices considered by von Karman and Rubach (1913) and are well known observations in flows past a cylinder. The flow in the Southern Ocean around the Antarctic continent is also azimuthally periodic and is best modelled as either a periodic domain or on the surface of the sphere.

Consider an infinite array of equal strength point vortices placed at $z_{\pm n} = \pm an$ where $n = 1, 2, 3, ..$ and $a \in \mathbb{R}$. It is clear that this is a stationary configuration since for some $n = m$, the velocity field at $z_m = am$ owing to the vortices with $n < m$ will cancel exactly with that owing to the vortices with $n > m$. This configuration is unstable with respect to small displacements of a single vortex (Saffman 1992). The idealization of the Karman vortex street is then the latter configuration with a second row of point vortices, of equal but opposite circulation to the row of vortices at $z_{\pm n} = \pm an$, added at $z_{\pm n} = \pm a(n + 1/2) + ib$, $b \in \mathbb{R}$. A treatment of the stability of this configuration is given in Lamb (1932) and is dependent on the ratio of $a$ to $b$. Let $k = b/a$, then for $k = 0.2801$ the street is stable to all infinitesimal disturbances, but not to all finite amplitude disturbances. For $k \neq 0.2801$, stability is dependent on the wavenumber of the disturbance.

The problem of three vortices in a periodic domain is reviewed in Aref et al. (2003). For the case when the circulations of the three vortices sum to zero, a method for constructing a family of translating *relative equilibria* is presented. Here *relative* is used in the sense that the configurations are not *stationary* but are invariant in a translating frame of reference. The construction is based on a mapping of the three vortex problem in a periodic strip of width $L$ onto a simpler problem where the advection of a passive particle in a field of fixed vortices is considered. A method for constructing stationary three vortex equilibria is also detailed along with the construction of stationary equilibria of more than three vortices in which the sum of the vortex circulations is non-zero. The system of four vortices in a periodic strip, two positive and two negative, all with the same absolute magnitude was first considered

by Domm (1956).

Aref et al. (2003) also review the construction of multi-vortex equilibria on the surface of a sphere. It is possible to construct a two-vortex equilibria on the sphere by placing two vortices of equal strength on the same latitudinal circle at diametrically opposite points. In this configuration the vortices will co-rotate about their latitudinal circle. Placing the vortices at opposite points of the equator results in them being 'shielded' from each other due to the curvature of the sphere and the configuration will remain stationary. For two vortices with same sign but different magnitude circulations, an equilibrium is possible through modifying the latitude (but not the longitude) of one of the vortices of the previous configuration. Both vortices will then precess steadily about their latitudinal circles. If the sign of one of the vortices is changed, an equilibrium can be constructed through placing the two vortices on the same longitudinal line but at different latitudes. If the vortices have equal circulations they will be at 'opposite' latitudes, that is, they will be equidistant from the equator. Vortices in this configuration then precess steadily about their latitudinal circles. Some other known equilibria on the sphere include single and double multi-vortex ring equilibria and equilibria with vortices at the vertices of Platonic solids (Aref et al. 2003).

The equilibria discussed so far have been constructed solely of point vortices. For many such equilibria, it is possible to 'desingularise' the point vortices into small patches of piecewise constant vorticity and find (often numerically) the corresponding non-singular equilibria. From a geophysical perspective it is often useful to consider problems involving finite area vortices and knowledge of point vortex equilibria can

often give insight into what steady configurations may exist. The advantage of considering constant distributions of vorticity as opposed to distributions of variable vorticity is that the velocity field throughout the fluid is determined by the shape of the vortex boundaries. This enables the use of some boundary integral methods (and also analytical methods - see later) such as the computational method of contour dynamics (see Dritschel 1989). Some early examples of equilibria computed using this method include rotating and translating equilibria found by Deem and Zabusky (1978) and later by Wu et al. (1984) and the family of steadily translating patches of equal but opposite vorticity computed by Pierrehumbert (1980).

Later, with geophysical applications in mind, McDonald (2002) considered the flow of a rotating, barotropic fluid with piecewise constant (potential) vorticity past a cylinder with circulation in the presence of an infinitely long escarpment. In this system, the circulation imposed around the cylinder results in fluid columns crossing the escarpment and the conservation of potential vorticity then requires these columns to acquire relative vorticity. In general, the vortical interface owing to the escarpment is capable of supporting wave motion. Such flow situations are observed in the Earth's atmosphere and oceans, for example in the Gulf Stream, where intense vortices frequently interact with strong currents. It is of interest to oceanographers whether such interactions lead to 'trapped' steadily propagating or long-lived vortical structures. For certain configurations of vorticity it is possible that the wave drag of a vortex can be made to vanish resulting in a non-radiating equilibrium (see Scullen and Tuck 1995, for the for the analogous, free-surface gravity wave situation). In Mc-Donald (2002), the escarpment separated shallow from deep water with the cylinder

lying in the deep water. It was shown that a non-radiating steady state was possible for a specific positive circulation imposed about the cylinder. The steady state contour shapes were calculated analytically in the linear limit of small amplitude waves, and the method of contour dynamics was utilized to calculate the corresponding non-linear steady states. In McDonald (2004) a similar analysis is conducted for the situation where the cylinder is replaced with two horizontally aligned point vortices with equal and positive circulations, two such point vortices being necessary to achieve a non-radiating state on the interface. This being essentially a result of destructive interference. Non-linear equilibria have also been determined in domains other than the plane, in the study of Polvani and Dritschel (1993) a number of single and multi-vortex equilibria are determined on the surface of the sphere and their stability analysed.

While much of the progress in this area has been made from utilizing numerical methods, some examples of exact non-linear desingularised solutions exist. The Lamb dipole is a well known example of such an exact solution, consisting of a steadily translating vorticity distribution in which the vorticity varies as a linear function of the streamfunction. Meleshko and Heijst (1994) give an historical overview of the Lamb dipole along with some other exact solutions involving distributed regions of vorticity. More recently, a series of papers by Crowdy (e.g. 1999; 2002a; 2002b) and Crowdy and Marshall (2004) present a range of exact multi-polar equilibria consisting of finite-area regions of constant vorticity together with a finite number point vortices. Analytical solutions are constructed through using the theory of Schwarz functions to satisfy the required steady boundary conditions. In Crowdy and Cloke (2003) similar

techniques are utilized to construct exact multi-polar equilibria on the surface of the sphere. The added step in constructing such multi-polar equilibria on the surface of a sphere is the stereographic projection of the problem into the complex plane, where the curvature of the sphere and the Gauss constraint (that is, the total vorticity on the sphere must sum to zero) introduce some subtleties into the problem. A characteristic feature of all these exact solutions is that the velocity vanishes identically outside the vortical region i.e. the equilibria have zero circulation.

Motivated by geophysical applications and the studies of McDonald (2002, 2004), here systems of vortex equilibria consisting of point vortices in the presence of a shear flow will be investigated. The shear flow gives rise to a vorticity gradient, which is modelled here as two regions of constant vorticity separated by an infinitely long interface. Many 'long-lived' vortical structures are observed in the Earth's atmosphere and oceans and in the atmospheres of the Solar System's gas giants, with some structures existing for a great many vortex turnover times. Mediterranean salt lenses have been tracked as well defined anomalies in the Atlantic Ocean for up to two years (Armi et al. 1989) and deep ocean eddies in the Greenland Sea for about a year (Gascard et al. 2002). Many of these structures reside in a background gradient of vorticity, for example, ocean eddies near intense currents such as the Gulf Stream. The shear flow structure of the Gulf Stream is capable of supporting waves and vortices moving in the presence of such vorticity gradients will invariably radiate vorticity waves. Jupiter's Great Red Spot is another famous example of a long lived vortical structure interacting with strong background shear flows. In general, a steady state will therefore requires a configuration of vortices such that the wave radiation

is eliminated.

Here, the systems considered are (1) two point vortices with equal but opposite circulation either side of a vorticity interface, (2) a row of periodic vortices in the presence of a shear flow and (3) an anti-symmetric configuration, with two vortices per period, in the presence of a shear flow (that is, the periodic analogue of (1)). This chapter will detail the derivation of analytical solutions valid in the linear limit of small amplitude disturbances at the vorticity interface. Existence of such linear equilibria is a good indication that genuine (non-linear) equilibria may exist. The shapes of linear equilibria can also give a good indication of what shapes their non-linear counterparts may take. This information is then a useful guide for preparing an algorithm to compute non-linear equilibria. In chapter 2 the corresponding non-linear equilibria will be investigated using the method of contour dynamics.

## 2.1 An anti-symmetric translating equilibrium

The equation governing the 2D flow of inviscid, incompressible fluid in the presence of a vorticity interface can be written as

$$\frac{D\omega_T^*}{Dt} = 0, \tag{2.1}$$

where

$$\omega_T^* = \omega_0^* + \nabla^2 \psi^*(x^*, y^*) + \omega^*(x^*, y^*), \tag{2.2}$$

is the total vorticity represented by the sum of three terms. Here $\psi^*$ is a stream-function representing the effect of vorticity owing to point vortices and perturbations to the interface (here the convention $u^* = -\psi_{y^*}^*$, $v^* = \psi_{x^*}^*$ is used), $\omega_0^*$ is a constant

background vorticity and $\omega^*$ is a piecewise constant jump in vorticity owing to the interface. The vorticity interface, here generated by a shear flow, can be represented as $\omega^*(x^*, y^*) = \tilde{\omega}^* H(y^*)$ where $\tilde{\omega}^*$ is the jump in vorticity across the interface and $H(y^*)$ is the Heaviside step function. Let $U^*$ be the free stream velocity such that $(u^*, v^*) \to (U^*, 0)$ as $(x^{*2} + y^{*2})^{1/2} \to \infty$. The flow also consists of point vortices: let $\Gamma^*$ be their magnitude and $L^*$ the magnitude of their distance from the interface. Taking $\tilde{\omega}^*$ and $L^*$ as the time and length scales of the problem, a nondimensionalization is carried out giving the following non-dimensional parameters

$$U = \frac{U^*}{\tilde{\omega}^* L^*}, \tag{2.3}$$

and

$$\Gamma = \frac{\Gamma^*}{\tilde{\omega}^* L^{*2}}. \tag{2.4}$$

Now, in dimensionless units, consider a shear flow with piecewise constant vorticity and jump $\tilde{\omega} = -1$ at $y = 0$ such that, (in the absence of point vortices)

$$\omega = \begin{cases} 1/2, & y > 0, \\ -1/2, & y < 0. \end{cases} \tag{2.5}$$

With a free stream velocity of $U$ imposed in the positive $x$ direction, the velocity field in the absence of point vortices is given by

$$u - iv = \begin{cases} U - y/2, & y > 0, \\ U + y/2, & y < 0. \end{cases} \tag{2.6}$$

Two point vortices of circulations $\Gamma$ and $-\Gamma$ are placed at $r_- = (-L/2, -1)$ and $r_+ = -r_-$ respectively. This gives the flow situation depicted in figure 2.1. The effect of the vortices will be to perturb the vorticity interface, thus inducing waves upon it.

Now consider the initial unperturbed shear flow. If at some initial time the vortices are then 'turned' on, this will result in some fluid being moved from $y < 0$ into $y > 0$ and vice versa. In two dimensions, the scalar vorticity associated with each fluid particle is conserved. Therefore, the problem can be viewed as the initial shear flow along with additional regions of vorticity with $\nabla^2 \psi = -1$ when fluid has crossed from $y < 0$ into $y > 0$, and $\nabla^2 \psi = 1$ when fluid has crossed from $y > 0$ into $y < 0$. In this section, linear theory is used to construct a non-radiating solution such that the velocities at the vortices vanishes and the configuration remains stationary. The parameters of the problem are $\Gamma$, $L$ and $U$.
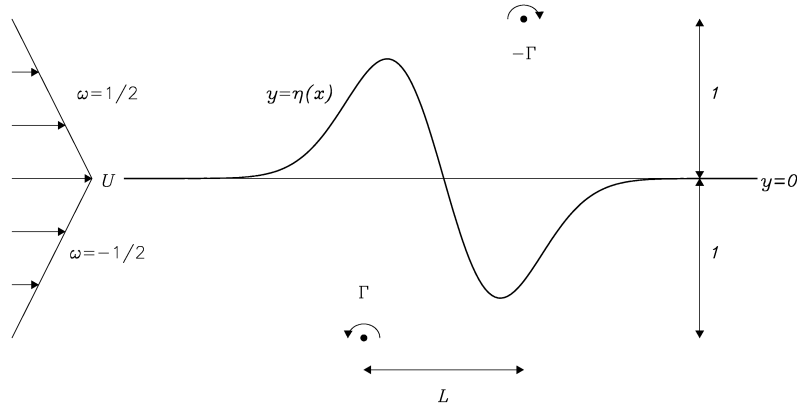


Figure 2.1: Sketch of the non-dimensional problem being considered. A shear flow is present with vorticity jump $\tilde{\omega} = -1$ such that $\omega = 1/2$ in $y > 0$ and $\omega = -1/2$ in $y < 0$ and the velocity is $U$ at $y = 0$. Two vortices are placed at $y = \pm 1$ and separated by a horizontal distance of $L$ with circulations of $\pm\Gamma$. The fluid disturbance along the vorticity interface is labelled as $y = \eta(x)$.

Denote the $y$-direction displacement of the vortical interface by $y = \eta(x)$, where

$|\eta| \ll 1$. At the vorticity interface

$$\frac{D}{Dt}(y - \eta) = 0, \tag{2.7}$$

which gives

$$v = \frac{D\eta}{Dt} = \frac{\partial \eta}{\partial t} + U \cdot \nabla \eta. \tag{2.8}$$

For a stationary configuration $\partial \eta / \partial t = 0$, therefore the linearised problem is to find $y = \eta(x)$, $|\eta| \ll 1$, by solving

$$U\frac{\partial \eta}{\partial x} = v, \text{ on } y = 0, \tag{2.9}$$

where the vertical velocity, $v$, is given by

$$v = \frac{\partial}{\partial x}\left\{ -\frac{1}{2\pi}\int_{-\infty}^{\infty}\int_{0}^{\eta(x')} \log\left[\left((x-x')^2 + (y-y')^2\right)^{1/2}\right] dy' dx' \right.$$

$$\left. + \frac{\Gamma}{2\pi}\left(\log\left[(x+L/2)^2 + (y+1)^2\right]^{1/2} - \log\left[(x-L/2)^2 + (y-1)^2\right]^{1/2}\right)\right\}, \tag{2.10}$$

and $U$ is the uniform background flow required to render the configuration stationary. The integral term in (2.10) represents the contribution to the velocity owing to the vorticity anomaly due to the displacement of $y = \eta(x)$, whereas the final two terms represent the two point vortices. The negative sign appears in front of the term owing to the vorticity anomaly is, as mentioned above, such that $\nabla^2 \psi = -1$ for $y > 0$. As it is assumed that $\Gamma > 0$, the mutual self advection of the point vortices will result in propagation in the negative $x$-direction. It is therefore expected that a stationary configuration has $U > 0$. Consistent with linear dynamics, the approximation $|\eta| \ll 1$

and $y = 0$ are made in (2.10) giving

$$v = -\frac{1}{2\pi}\int_{-\infty}^{\infty}\int_{0}^{\eta(x')}\frac{x - x'}{(x - x')^2 + y'^2}dy'dx' + \frac{\Gamma}{2\pi}\left[\frac{x + \frac{L}{2}}{\left(x + \frac{L}{2}\right)^2 + 1} - \frac{x - \frac{L}{2}}{\left(x - \frac{L}{2}\right)^2 + 1}\right]$$

$$= -\frac{1}{2\pi}\int_{-\infty}^{\infty}\frac{\eta(x')}{(x - x')}dx' + \frac{\Gamma}{2\pi}\left[\frac{x + \frac{L}{2}}{\left(x + \frac{L}{2}\right)^2 + 1} - \frac{x - \frac{L}{2}}{\left(x - \frac{L}{2}\right)^2 + 1}\right].$$

(2.11)

The Fourier Transform (FT) of $v$ is given by

$$\tilde{v} = \frac{1}{2\pi}\int_{-\infty}^{\infty}ve^{-ikx}dx,$$

(2.12)

where $k$ is a wavenumber. Taking the FT of (2.11) yields

$$\tilde{v} = \frac{1}{2\pi}\int_{-\infty}^{\infty}\left\{-\frac{1}{2\pi}\int_{-\infty}^{\infty}\frac{\eta(x')}{(x - x')}dx' + \frac{\Gamma}{2\pi}\left[\frac{x + \frac{L}{2}}{\left(x + \frac{L}{2}\right)^2 + 1} - \frac{x - \frac{L}{2}}{\left(x - \frac{L}{2}\right)^2 + 1}\right]\right\}e^{-ikx}dx$$

$$= -\frac{i}{2}\text{sgn}k\tilde{\eta} + \frac{\Gamma i}{4\pi}\text{sgn}ke^{-|k|}\left(e^{ik\frac{L}{2}} - e^{-ik\frac{L}{2}}\right).$$

(2.13)

Using (2.13) the FT of (2.9) is given by

$$Uik\tilde{\eta} = \frac{i}{2}\text{sgn}k\tilde{\eta} + \frac{\Gamma}{2\pi}\text{sgn}ke^{-|k|}\sin\left(\frac{kL}{2}\right),$$

(2.14)

where

$$\tilde{\eta} = \frac{1}{2\pi}\int_{-\infty}^{\infty}\eta e^{-ikx}dx.$$

(2.15)

Solving (2.14) for $\tilde{\eta}$ gives

$$\tilde{\eta} = -\frac{\Gamma i}{2\pi}\text{sgn}ke^{-|k|}\frac{\sin(kL/2)}{Uk - \text{sgn}k/2}.$$

(2.16)

The dispersion relation for interfacial waves, following the analysis of Bell (1990) is given by

$$\sigma = Uk - \frac{1}{2}\operatorname{sgn} k, \tag{2.17}$$

where $\sigma$ is the frequency. The phase and group velocities are

$$c_p = U - \frac{1}{2|k|}, \qquad c_g = U - \delta(k), \tag{2.18}$$

where $\delta$ is the delta function. When $U = 1/2|k|$ (2.16) has a simple pole and a steady wavetrain forms downstream of the vortices and this, in general occurs for all $U > 0$. In order for a stable configuration to exist it is required that this wave train vanishes. Physically, this is equivalent to demanding that the wave trains due to each point vortex destructively interfere. For this to be the case it is required that the simple pole of (2.16) located at $k = 1/2U$ vanishes. Setting $L/2U = 2n\pi, n = 0, 1, 2, ...$, this pole does indeed vanish and hence no wavetrain is located downstream of the vortices, since from (2.16)

$$\lim_{k \to 1/2U} \frac{\sin(2n\pi kU)}{Uk - 1/2} = (-1)^n 2n\pi, \qquad n = 0, 1, 2, \ldots \quad . \tag{2.19}$$

In the results that follow, $n$ is set to $n = 1$ giving $L = 4\pi U$, the case where the vortices are at their smallest horizontal separation. The contour shape is determined by taking the inverse FT of equation (2.14) given by

$$\eta(x) = \int_{-\infty}^{\infty} \tilde{\eta} e^{ikx} dk, \tag{2.20}$$

and therefore

$$\eta(x) = -\frac{\Gamma i}{2\pi} \int_{-\infty}^{\infty} \operatorname{sgn}k \, e^{-|k|} \frac{\sin(2kU\pi)}{Uk - \operatorname{sgn}k/(2)} e^{ikx} dk = \frac{\Gamma}{\pi U} \int_{0}^{\infty} \frac{e^{-k}\sin(2kU\pi)\sin(kx)}{k - 1/(2U)} dk. \tag{2.21}$$

Plotting (2.21) gives a contour which is anti-symmetric about $x = 0$ whose shape is determined by $U$ and $\Gamma$. The integral is computed numerically using a fourth order Runge-Kutta method for various values of $x$. Figure 2.2 shows $\eta(x)/\Gamma$ for $U = 1.0$ and $U = 0.187$.
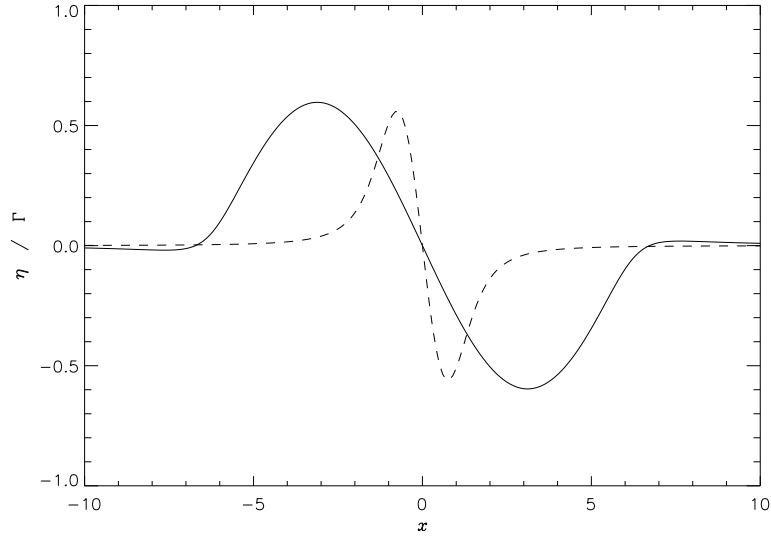


Figure 2.2: Profiles of $\eta(x)$ given by (2.21) (normalised by $\Gamma$) with the non-radiating condition $L = 4\pi U$; the solid line represents $U = 1.0$ and the dashed line $U = 0.1876$.

For a stationary configuration to be possible is also required that the $x$ and $y$ velocities at both point vortices, induced by the contour and the other point vortex, vanish for some values of $U$ and $\Gamma$. In general the $y$-direction velocity at a position $(x, y)$ due to a point vortex with circulation $\gamma$ at a position $(a, b)$ is given by

$$v = \frac{\partial}{\partial x} \frac{\gamma}{2\pi} \log \left[ (x - a)^2 + (y - b)^2 \right]^{\frac{1}{2}}. \tag{2.22}$$

In the system under consideration $\gamma = \Gamma$ at $-L/2$ and $\gamma = -\Gamma$ at $L/2$. Owing to the anti-symmetry of the problem, the $y$-direction velocity induced at each point vortex

due to the other point vortex is, using $L = 4\pi U$, given by

$$v_{loc} = \frac{U\Gamma}{2(1 + (2\pi U)^2)}.$$  (2.23)

The $y$-direction velocity at each point vortex induced by the vorticity anomalies due to the displaced contour is given by

$$v_c = -\frac{1}{2\pi} \int_{-\infty}^{\infty} \frac{\eta(x')(\pm L/2 - x')}{(\pm L/2 - x')^2 + 1} dx',$$

(2.24)

$$= \frac{\Gamma i}{4\pi^2 U} \int_{-\infty}^{\infty} \int_{-\infty}^{\infty} \frac{\mathrm{sgn}k e^{-|k|} \sin(2kU\pi) e^{ikx'}}{k - \frac{\mathrm{sgn}k}{2U}} \frac{(\pm L/2 - x')}{(\pm L/2 - x')^2 + 1} dx' dk.$$

Using the substitutions $\zeta = L/2 + x'$ when $r = r_-$ and $\zeta = -L/2 + x'$ when $r = r_+$ yields

$$v_c = \frac{\Gamma}{4\pi U} \int_{-\infty}^{\infty} \frac{e^{-|k|} \sin(2kU\pi)}{k - \frac{\mathrm{sgn}k}{2U}} e^{-|k|} e^{\mp ikL/2} dk,$$

$$= \frac{\Gamma}{2\pi U} \int_{0}^{\infty} \frac{e^{-2k}}{k - \frac{1}{2U}} \sin(2kU\pi) \cos\left(\frac{kL}{2}\right) dk,$$  (2.25)

$$= \frac{\Gamma}{4\pi U} \int_{0}^{\infty} \frac{e^{-2k}}{k - \frac{1}{2U}} \sin(4kU\pi) dk.$$

Here, $U$ is positive and hence the vortices will have zero velocity in the $y$-direction if (2.23)+(2.25)= 0. Figure 2.3 shows plots of $v_{loc}(x)/\Gamma$ and $-v_c(x)/\Gamma$ for various values of $U$. The condition that (2.23)+(2.25)= 0 is satisfied for $U = U_S \approx 0.1876$.

It has been shown that for this pair of vortices it is possible to impose a specific $U_S$ and $L(= 4\pi U_S)$ such that the vertical velocity at the vortices vanishes. It now remains to resolve the condition that renders the vortices stationary in the horizontal
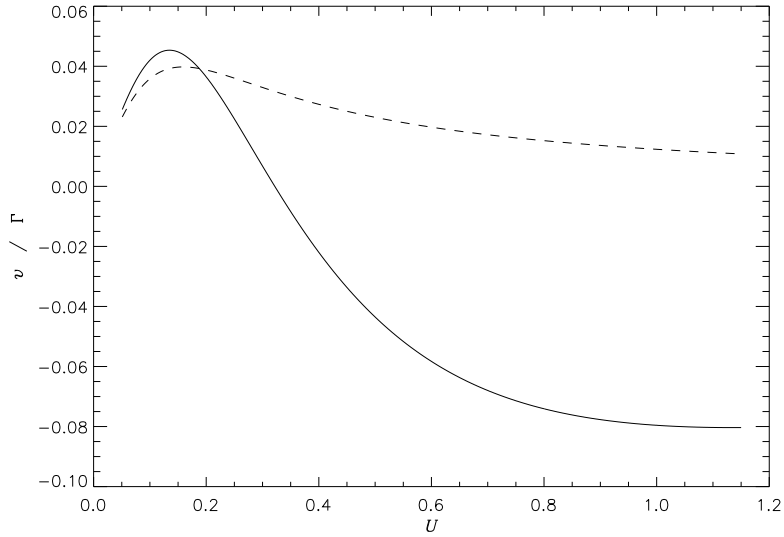
Figure 2.3: Plot of $-v_c(x)/\Gamma$ (solid line) and $v_{loc}(x)/\Gamma$ (dashed line) (vertical axis) against $U$ (horizontal axis).

direction. Now consider the $x$-direction velocities at each point vortex due to the other vortex and the contour. The $x$-direction velocity at a position $(x, y)$ owing to a vortex at $(a, b)$ is given by

$$u = -\frac{\partial}{\partial y}\frac{\gamma}{2\pi}\log\left[(x-a)^2 + (y-b)^2\right]^{\frac{1}{2}}. \tag{2.26}$$

Again, due to the anti-symmetry of the problem the $x$-direction velocities at both vortices are equal and are given by

$$u_{loc} = -\frac{\Gamma}{4\pi(4\pi^2 U^2 + 1)}. \tag{2.27}$$

Horizontal velocities at the vortices owing to the contour are given by

$$u_c = \frac{1}{2\pi}\int_{-\infty}^{\infty}\frac{\eta(x')(\pm 1 - 0)}{(\pm L/2 - x')^2 + 1}dx'. \tag{2.28}$$

Proceeding in the same way as determining (2.24), (2.28) gives

$$u_c = \frac{\Gamma}{2\pi U} \int_0^\infty \frac{e^{-2k} \sin^2(2\pi U k)}{k - \frac{1}{2U}} dk. \qquad (2.29)$$

Letting $U = U_S$, (2.27) gives $u_{loc} = -0.0333\Gamma$ and (2.29) gives $u_c = -0.0751\Gamma$. Hence, the condition for a stationary equilibrium for $y < 0$, using (2.6), is given by $-(0.0333 + 0.0751)\Gamma + U_S - 0.5 = 0$ giving $\Gamma_S = -2.882$. Figure 2.4 shows the resultant unique interface shape and point vortex locations. It is seen that for the required values of $U_S$ and $\Gamma_S$ the interface amplitude becomes large and actually crosses the point vortices rendering linear theory invalid. Even if a larger horizontal vortex separation is used, such as $L = 8\pi U$ from setting $n = 2$ in (2.19), this is still the case. It is concluded that a stationary configuration, according to linear theory, is thus not attainable for the anti-symmetric analogue of McDonald (2004). The existence (or non-existence) of linear equilibria however, only give an 'indication' of the possible existence (or non-existence) of corresponding non-linear equilibria. Although this appears to be a "null" result it does not rule out the existence of corresponding non-linear equilibria. However, as will be reported in chapter 3, no equilibria of this kind could be found numerically.

## 2.2 An infinite array of periodic vortices

In this section, the problem of an infinite periodic array of same circulation point vortices placed periodically below a vorticity jump is considered. Linear theory is used to find the interfacial shapes of vortex equilibria in the limit that the amplitude of oscillations on the interface are small. Considered first is the case when the point
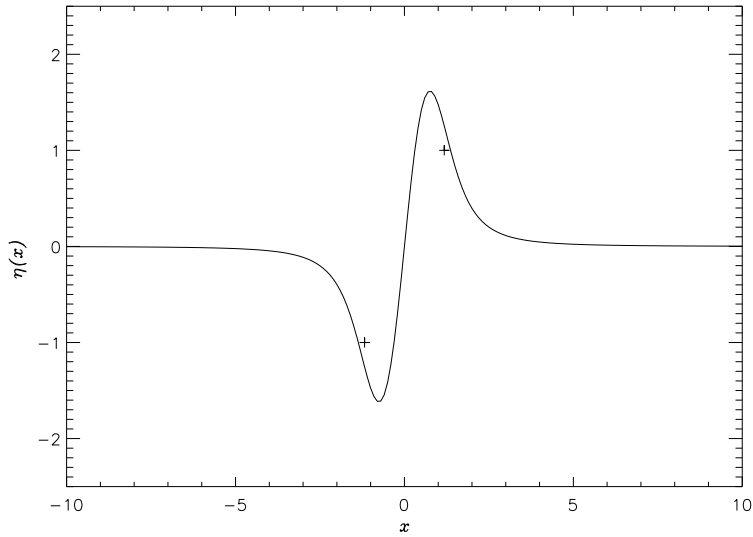
Figure 2.4: Profiles of $\eta(x)$ with $U_S = 0.1876$ and $\Gamma_S = -2.882$. The horizontal vortex equilibrium separation is given by $L = 4\pi U$ and the two $+$ signs mark the point vortex locations.

vortices are located in the irrotational region of the flow, followed by the case when the vortices are located in the rotational region. The corresponding non-linear shapes are found computationally in the following chapter.

## 2.2.1    Vortices in the irrotational flow region

The problem is initially considered in the plane and the vorticity jump is provided by a shear flow. Periodicity is expected during the solution process. As seen in section 2.1 the flow is nondimensionalized using the vorticity jump, $\tilde{\omega}^*$, and distance of the vortices from the interface, $L^*$, as the time and length scales respectively. Consider a

shear flow with a vorticity jump $\tilde{\omega} = -1$ at $y = 0$ such that

$$
\omega = \begin{cases} 1, & y > 0, \\ 0, & y < 0. \end{cases} \tag{2.30}
$$

With a free stream velocity of $U$ imposed in the positive $x$ direction, the velocity field in the absence of point vortices is given by

$$
u - iv = \begin{cases} U - y, & y > 0, \\ U, & y < 0. \end{cases} \tag{2.31}
$$

An infinite row of point vortices with circulations $\Gamma$ are placed at $r_n = (nL, -1)$ where $n \in \mathbb{Z}$. Note that the vortices lie in the irrotational region. The interfacial shape, $\eta(x)$, will therefore be an even function on $[-L/2, L/2]$ in order to ensure the vertical velocity at any given point vortex vanishes, i.e. $v_{loc} = 0$. In fact, the demand that $v_{loc} = 0$ necessarily implies this. The problem therefore consists of three parameters, $U$, $\Gamma$ and $L$. Unlike the problem considered in section 2.1, due to the periodicity of the configuration, no radiation condition is required in the current problem. Therefore a two parameter family of solutions is expected. A schematic of the problem is shown in figure 2.5.

Consider the $x$-direction velocity at a point vortex. The stream function owing to the vorticity anomalies (relative to the background vorticity distribution of the shear flow) due to the displaced contour is given by

$$
\psi_{contour} = \frac{-1}{2\pi} \int_{-\infty}^{\infty} \int_0^{\eta(x')} \log \left[ \left( (x - x')^2 + (y - y')^2 \right)^{1/2} \right] dy' dx'. \tag{2.32}
$$

The condition to ensure $u_{loc} = 0$ is given by

$$
U + \frac{\partial}{\partial y} \frac{1}{2\pi} \int_{-\infty}^{\infty} \int_0^{\eta(x')} \log \left[ \left( (x - x')^2 + (y - y')^2 \right)^{1/2} \right] dy' dx' = 0. \tag{2.33}
$$
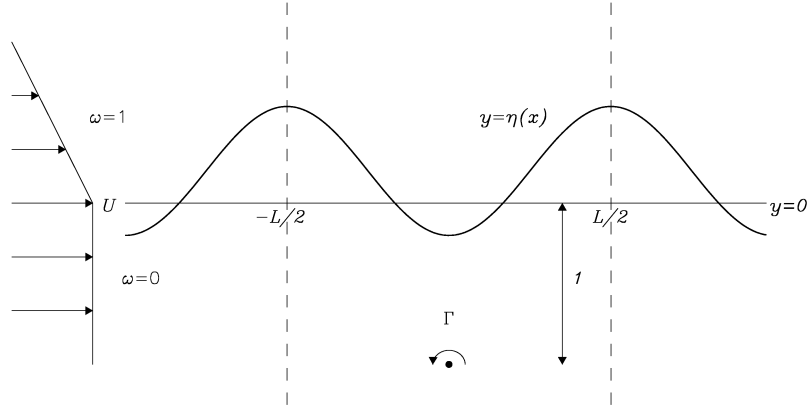
Figure 2.5: Schematic of the problem under consideration. A shear flow is present with vorticity jump $\tilde{\omega} = -1$ such that $\omega = -1$ in $y > 0$ and $\omega = 0$ in $y < 0$ and the velocity is $U$ at $y = 0$. Point vortices of circulation $\Gamma$ are arranged periodically at $x = nL$ where $n \in \mathbb{Z}$ and $y = -1$. The fluid disturbance along the vorticity interface is labelled as $y = \eta(x)$.

Evaluating (2.33) at the vortex location $(0, -1)$ and using the linear approximation $|\eta| \ll 1$ gives

$$U + \frac{1}{2\pi} \int_{-\infty}^{\infty} \int_{0}^{\eta(x')} \frac{-1}{x'^2 + 1} dx' dy' = 0, \tag{2.34}$$

and hence the condition for $u_{loc} = 0$ is given by

$$U - \frac{1}{2\pi} \int_{-\infty}^{\infty} \frac{\eta(x')}{x'^2 + 1} dx' = 0. \tag{2.35}$$

Now consider the condition at the vortical interface. As in section 2.1, the condition on the interface is given by

$$U\frac{\partial \eta}{\partial x} = v, \text{ on } y = 0. \tag{2.36}$$

Thus

$$U\frac{\partial \eta}{\partial x} = \frac{1}{2\pi}\frac{\partial}{\partial x}\left[-\int_{-\infty}^{\infty}\int_{0}^{\eta(x')}\log\left[\left((x-x')^2+(y-y')^2\right)^{1/2}\right]dy'dx'\right.$$

$$\left.+\Gamma\sum_{n=-\infty}^{\infty}\log\left[\left((x+nL)^2+(y+1)^2\right)^{\frac{1}{2}}\right]\right]$$

$$= \frac{1}{2\pi}\left[-\int_{-\infty}^{\infty}\int_{0}^{\eta(x')}\frac{x-x'}{(x-x')^2+(y-y')^2}dx'dy'+\Gamma\sum_{n=-\infty}^{\infty}\frac{x+nL}{(x+nL)^2+(y+1)^2}\right],$$

$$(2.37)$$

where the sum represents the infinite periodic array of point vortices. Consistent with linear theory, the approximations that $|\eta| \ll 1$ and $y = 0$ are once again made in (2.37) giving

$$U\frac{\partial \eta}{\partial x} = \frac{1}{2\pi}\left[-\int_{-\infty}^{\infty}\frac{\eta(x')}{x-x'}dx'+\Gamma\sum_{n=-\infty}^{\infty}\frac{x+nL}{(x+nl)^2+1}\right]. \qquad (2.38)$$

Now $\eta(x)$ is a periodic function and can thus be represented as a Fourier series. As mentioned at the beginning of the section, it is required that $\eta(x)$ is an even function on $[-L/2, L/2]$ and therefore can be written as

$$\eta(x) = \frac{a_0}{2} + \sum_{k=1}^{\infty}a_k\cos\left(\frac{2k\pi x}{L}\right), \qquad (2.39)$$

where the real constants $a_k$ are given by

$$a_k = \frac{4}{L}\int_{0}^{\frac{L}{2}}\eta(x)\cos\left(\frac{2k\pi x}{L}\right)dx. \qquad (2.40)$$

The summation term on the right hand side of (2.38), $\sum_{n=-\infty}^{\infty}\frac{x+kl}{(x+kl)^2+1}$, which is an odd extension in $\left[0, \frac{L}{2}\right]$ can also be written as a Fourier series. However, it simplifies

the problem to use a different representation of this infinite series. Here, a suitable form for the streamfunction along $y = 0$ of an infinite array of point vortices is given by

$$\psi_{loc}(x,0) = \frac{\Gamma}{2\pi} \log \left| \beta - \cos\left(\frac{2\pi x}{L}\right) \right|^{\frac{1}{2}}, \tag{2.41}$$

where $\beta = \cosh\frac{2\pi}{L}$ (see Appendix B for details). The $y$-direction velocity at the interface owing to the point vortices is thus given by

$$\frac{\partial \psi_{loc}}{\partial x} = \frac{\Gamma}{2L} \frac{\sin\left(\frac{2\pi x}{L}\right)}{\beta - \cos\left(\frac{2\pi x}{L}\right)}, \tag{2.42}$$

and equating (2.42) to the summation on the right hand side of (2.38) gives

$$\frac{\Gamma}{2\pi} \sum_{n=-\infty}^{\infty} \frac{x+kl}{(x+kl)^2+1} = \frac{\Gamma}{2L} \frac{\sin\left(\frac{2\pi x}{L}\right)}{\beta - \cos\left(\frac{2\pi x}{L}\right)} = g(x). \tag{2.43}$$

The newly introduced function, $g(x)$, can then be written as a Fourier series given by

$$g(x) = \sum_{k=1}^{\infty} b_k \sin\left(\frac{2\pi k x}{L}\right), \tag{2.44}$$

where

$$b_k = \frac{\Gamma}{2L} \int_0^{L/2} \frac{\sin\left(\frac{2\pi x}{L}\right)}{\beta - \cos\left(\frac{2\pi x}{L}\right)} \sin\left(\frac{2\pi k x}{L}\right) dx \tag{2.45}$$

$$= \frac{\Gamma}{\pi L} \int_0^{\pi} \frac{\sin z \sin kz}{\beta - \cos z} dz = \frac{\Gamma}{L} e^{-\frac{2k\pi}{L}}.$$

Substituting (2.45) into equation (2.38) (and swapping $n$ for $k$) gives

$$-\sum_{n=1}^{\infty} a_k \frac{2n\pi U}{L} \sin\left(\frac{2n\pi x}{L}\right) = \tag{2.46}$$

$$-\frac{1}{4\pi} \int_{-\infty}^{\infty} \frac{a_0}{x-x'} dx' - \frac{1}{2\pi} \sum_{n=1}^{\infty} \int_{-\infty}^{\infty} a_n \frac{\cos\left(\frac{2n\pi x}{L}\right)}{x-x'} dx' + \sum_{n=1}^{\infty} b_n \sin\left(\frac{2n\pi x}{L}\right).$$

It is now required to evaluate the two integrals (which are interpreted as Cauchy principal value integrals) on the right hand side of (2.46). The results of these two integrals are given below. The first integral yields

$$\int_{-\infty}^{\infty} \frac{a_0}{x - x'} dx' = 0. \tag{2.47}$$

The second integral can be written as

$$\int_{-\infty}^{\infty} \frac{\cos\left(\frac{2n\pi x'}{L}\right)}{x - x'} dx' = \Re \int_{-\infty}^{\infty} \frac{e^{i\frac{2n\pi x'}{L}}}{x - x'} dx'. \tag{2.48}$$

Substituting $\zeta = x' - x$ gives

$$\Re \left[ -e^{i\frac{2n\pi x}{L}} \int_{-\infty}^{\infty} \frac{e^{i\frac{2n\pi \zeta}{L}}}{\zeta} d\zeta' \right] = \pi \sin \frac{2n\pi x}{L}. \tag{2.49}$$

Note that $\mathrm{sgn}(2n\pi/L) = 1$ has been used to obtain the result of (2.49). Substituting (2.47) and (2.49) into (2.46) and equating coefficients of $\sin(2n\pi x/L)$ gives

$$a_n = \frac{b_n}{\frac{1}{2} - \frac{2n\pi U}{L}}. \tag{2.50}$$

Note that the form of (2.50) gives rise to the possibility of resonance of the $n$th mode occurring when $2n\pi U/L \simeq 1/2$. In such circumstances, there is potential for $a_n$ to become very large, resulting in large amplitude disturbances at the vorticity interface. Linear theory is clearly not expected to be a good guide in systems where such resonances occur.

In the studies of McDonald (2004) and Crowdy (1999, 2002a, b) it was shown that the equilibria necessarily had zero circulation. This result does not appear naturally in the present case. But, instead, it is insisted that the net circulation is zero. This enables $a_0$ to be determined. The zero net circulation case is, however, natural from

a geophysical point of view: a meandering current sheds eddies so that the eddy circulation and the vorticity deficit of the current must sum to zero. Considering the region $[-L/2, L/2]$, a net zero circulation equates to

$$\Gamma + \gamma \int_{-L/2}^{L/2} \eta(x) = 0. \tag{2.51}$$

Here, the vorticity jump across the contour is $-1$ giving $\gamma = -1$ and thus

$$\Gamma - \int_{-L/2}^{L/2} \left( \frac{a_0}{2} + a_n \cos \frac{2n\pi x}{L} \right) dx = 0 \tag{2.52}$$

yielding

$$a_0 = \frac{2\Gamma}{L}. \tag{2.53}$$

Equations (2.45) and (2.50) along with (2.35) and the result for $a_0$, (2.53), can now be used to calculate $U$ and thus obtain the shape of the contour $\eta$. Substituting into (2.35) gives

$$U - \frac{a_0}{4\pi} \int_{-\infty}^{\infty} \frac{dx'}{1 + x'^2} - \sum_{n=1}^{\infty} \frac{a_n}{2\pi} \int_{-\infty}^{\infty} \frac{\cos \frac{2n\pi x'}{L}}{1 + x'^2} dx' = 0. \tag{2.54}$$

Evaluating the integrals in (2.54) gives

$$\int_{-\infty}^{\infty} \frac{dx'}{1 + x'^2} = \pi, \tag{2.55}$$

and

$$\int_{-\infty}^{\infty} \frac{\cos \frac{2n\pi x'}{L}}{1 + x'^2} dx' = \pi e^{-\frac{2n\pi}{L}}. \tag{2.56}$$

Substituting (2.55) and (2.56) along with (2.50) into (2.54) gives

$$2U - \frac{\Gamma}{L} + \sum_{n=1}^{\infty} \frac{b_n}{\frac{2n\pi U}{L} - \frac{1}{2}} e^{-\frac{2n\pi}{L}} = 0, \tag{2.57}$$

where the constants $b_n$ are given in (2.45). Substituting (2.50) for $b_n$, (2.57) can be written as

$$2U + \frac{\Gamma}{L} \left( \sum_{n=1}^{\infty} \frac{e^{-\frac{4n\pi}{L}}}{\frac{2n\pi U}{L} - \frac{1}{2}} - 1 \right) = 0. \tag{2.58}$$

Values of $U$ can thus be approximated by truncating (2.58) at some $n = N$ and solving the resultant $(N + 1)^{th}$ order polynomial in $U$. For a given value of $\Gamma$ it is therefore possible for $U$ to take many different values. These possible values of $U$ will correspond to interfacial shapes of varying amplitudes and also, depending on $\Gamma$, some values of $U$ may be complex. Physically permissible solutions require $U \in \Re$ but also, within this linear analysis only solutions leading to small amplitude interfacial shapes are of interest. Note that the summation term on the left hand side of (2.58) decays exponentially with increasing $n$. Therefore, to a good approximation, two roots of $U$ can be approximated by truncating the sum at $n = 1$ and solving the resulting quadratic, or three roots by truncating at $n = 2$ and solving the resulting cubic and so on.

From the perspective of linear analysis, the roots of $U$ from (2.58) approximated as a quadratic (or possibly cubic) will be of primary interest. This is due to the fact that coefficients of higher powers of $U$ decay rapidly and the roots corresponding to these higher powers of $U$ will generally lead to resonance. Tables 2.1 and 2.2 show the solutions of (2.58) for $n$ truncated at 1,2,3,4 and $\Gamma = 0.5$ for $L = \pi$ and $L = 2\pi$ respectively. Clearly, for any value of $\Gamma$, many distinct linear equilibria exist, one for each possible value of $U$. However, from solving for the roots of $U$ for many different values of $\Gamma$ and plotting the resulting interface shapes, it was seen that only the roots corresponding to those of the quadratic gave solutions that were 'possibly' of interest. For the values of $\Gamma$ investigated, all other roots of $U$ led to resonance or were complex. (Note that 'possibly' is used here in the sense that roots of the quadratic can also lead to large amplitude interface shapes). To illustrate this, figure 2.6 shows

the shapes of $\eta(x)$ for the roots of $U$ obtained by truncating (2.58) at $n = 4$. The roots corresponding to those of the quadratic are $U = 0.017$ and $U = 0.249$. Here, the only root of interest is $U = 0.017$: this root leads to a small amplitude interface shape which is expected for small values of $U$. The interface in this case is nearly flat which is owing to the fact that the interface only needs to 'provide' a velocity field of $-0.017$ in the $x$-direction at the point vortex to render it stationary.

Therefore, in the analysis that follows, the shapes of $\eta(x)$ will be plotted for the roots of $U$ given from truncating the sum in (2.58) at $n = 1$ and solving the resulting quadratic. However, to ensure these roots are accurate to at least 3 decimal places, the corresponding 5th order polynomial will also be solved and the roots checked against this solution.

| $L = \pi$, $\Gamma = 0.5$ | | | | |
|---|---|---|---|---|
| n | 1$^{\text{st}}$ | 2$^{\text{nd}}$ root | 3$^{\text{rd}}$ root | 4$^{\text{th}}$ root | 5$^{\text{th}}$ root |
| 1 | 0.0839667 | 0.245611 | - | - | - |
| 2 | 0.0841344 | 0.124831 | 0.245612 | - | - |
| 3 | 0.0834575 | 0.0840103 | 0.124831 | 0.245612 | - |
| 4 | 0.0625001 | 0.0834575 | 0.0840102 | 0.124831 | 0.245612 |

Table 2.1: Table listing the roots of (2.58) for $L = \pi$ and $\Gamma = 0.5$ when $n$ is truncated at $1, 2, 3$ & $4$.

| $L = 2\pi$, $\Gamma = 0.5$ | | | | |
|---|---|---|---|---|
| n | 1$^{\text{st}}$ | 2$^{\text{nd}}$ root | 3$^{\text{rd}}$ root | 4$^{\text{th}}$ root | 5$^{\text{th}}$ root |
| 1 | 0.0518031 | 0.487986 | - | - | - |
| 2 | 0.0537108 | 0.24805 | 0.488028 | - | - |
| 3 | 0.0540137 | 0.166357 | 0.248055 | 0.48803 | - |
| 4 | 0.0540627 | 0.12495 | 0.166357 | 0.248055 | 0.488031 |

Table 2.2: Table listing the roots of (2.58) for $L = 2\pi$ and $\Gamma = 0.5$ when $n$ is truncated at $1, 2, 3$ & $4$.
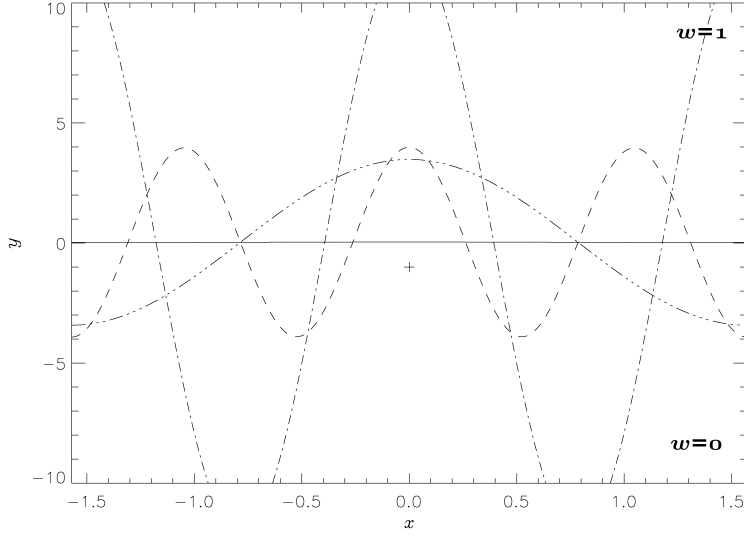
Figure 2.6: Shapes of the interface $\eta(x)$ for $L = \pi$ and $\Gamma = 0.1$ over one period of $-L/2$ to $L/2$. Values of $U$ have been obtained from truncating (2.58) at $n = 4$ and solving the resulting $5^{\text{th}}$ order polynomial. The solid line corresponds to $U = 0.017$, the dashed line $U = 0.083$, the dot-dash line $U = 0.125$ and the three-dot-dash line $U = 0.249$. (Note that the interface for $U = 0.017$ is 'not quite' flat and only appears so here due to the scale of the $y$-axis). The $+$ represents the point vortex location.

To help ascertain the values of $\Gamma$ for which physically permissible solutions may exist it is useful to consider the quadratic

$$U = \left[ \frac{L}{8\pi} + \frac{\Gamma}{4L} \right] \pm \frac{1}{2} \left[ \left( \frac{L}{4\pi} + \frac{\Gamma}{2L} \right)^2 - \frac{\Gamma}{\pi} \left( e^{-\frac{4\pi}{L}} + \frac{1}{2} \right) \right]^{\frac{1}{2}}, \qquad (2.59)$$

obtained from truncating (2.58) at $n = 1$, rearranging and then solving for $U$. Demanding $U \in \Re$ the constraint on $L$ and $\Gamma$ is therefore given by

$$\left( \frac{L}{4\pi} + \frac{\Gamma}{2L} \right)^2 > \frac{\Gamma}{\pi} \left( e^{-\frac{4\pi}{L}} + \frac{1}{2} \right). \qquad (2.60)$$

This condition, depending on the value of $L$, can lead to situations where 'lower' and 'upper' critical values of $\Gamma$ exist, in which, physically permissible solutions for $U$ exist for positive $\Gamma$ less than this 'lower' critical value and for $\Gamma$ greater than this 'upper'

critical value. However, for $\Gamma$ between these two critical values, solutions of $U$ are complex and are therefore not physical. Define

$$R(\Gamma, L) = \frac{\left(\frac{L}{4\pi} + \frac{\Gamma}{2L}\right)^2}{\frac{\Gamma}{\pi}\left(e^{-\frac{4\pi}{L}} + \frac{1}{2}\right)}. \tag{2.61}$$

Physically permissible (non-complex) solutions of $U$ will therefore exist when $R(\Gamma, L) \geq 1$. Figures 2.7 and 2.8 show plots of $R(\Gamma, L)$ against $\Gamma$. Figure 2.7, in which $L = \pi$, shows the two regions in which real solutions of (2.59) exist. In the region where $1.07 < \Gamma < 2.30$ solutions of (2.59) will be complex and therefore not physically permissible. For $\Gamma > 0$ and not within this region solutions of (2.59) will be real and therefore physically permissible. Note however, that the larger the value of $\Gamma$, the larger the expected amplitude of the interfacial waves. For waves of $O(1)$ amplitude, the validity of linear theory is brought into question and can be considered, at best, a 'guide' as to what non-linear equilibria may possibly exist. Figure 2.8 shows the corresponding plot in which $L = 2\pi$. Here the region of 'small' $\Gamma$ where $R(\Gamma, L) > 1$ is seen, but after $R(\Gamma, L)$ initially falls below 1 it does not rise above 1 again until $\Gamma \gg 1$.

Figures 2.9-2.12 show examples of $\eta(x)$ for various situations when $L = \pi$. When evaluating $\eta(x)$ the sum in equation (2.39) is truncated at $k = 50$ ensuring that the accuracy of $\eta(x)$ is determined by the accuracy of $U$ and not by the truncation. Figure 2.9 shows four interface shapes for $\Gamma$ below the lower 'critical' value of 1.07 and the negative root of (2.59) taken for $U$. For $\Gamma = 0.1$ the interface has a small amplitude hump symmetrically placed above the point vortex. The primary mode is clearly the dominant mode in this circumstance. As $\Gamma$ is increased the amplitude of this hump also increases and the effect of higher order modes is clearly visible upon
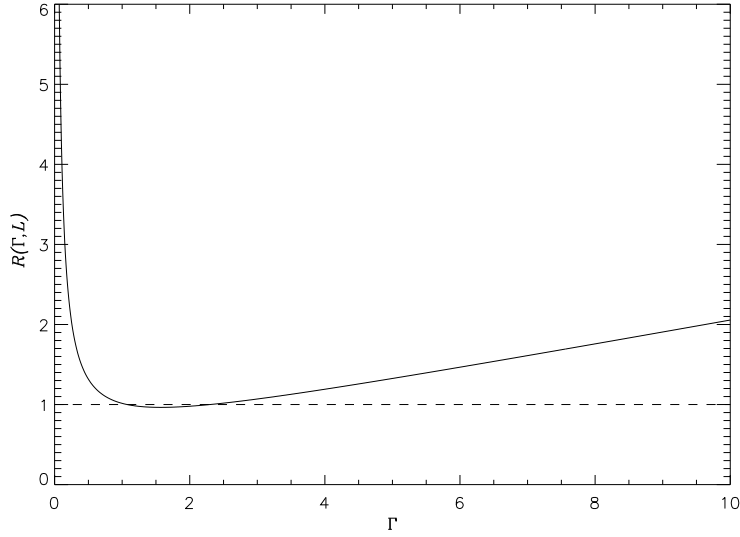
Figure 2.7: $R(\Gamma, L)$ (solid line) against $\Gamma$ for $L = \pi$. For values of $\Gamma$ where $R(\Gamma, L)$ is above the dashed line, solutions to the quadratic in $U$ are real and therefore physically permissible. In the region where $R(\Gamma, L) < 1$ no real solutions for $U$ exist. This region roughly corresponds to $1.07 < \Gamma < 2.30$.

the interface. Figure 2.10 shows the corresponding interface shapes to figure 2.9 with $U$ taken as the positive root of (2.59). Now, for $\Gamma = 0.1$ the freestream velocity $U = 0.249$ which is close to 2.5, the condition for an $n = 1$ resonance (see equation (2.50)). This results in large values of $a_1$ and therefore large amplitude interfacial waves dominated by the primary mode. As the value of $\Gamma$ increases the value of $U$ decreases, moving further away from the $n = 1$ resonance value of 2.5 resulting in the amplitude of the interfacial waves decreasing.

Figures 2.11 and 2.12 show the interface shapes for $\Gamma$ above the upper 'critical' value of 2.30 for $U$ taken as the negative and positive roots of (2.59) respectively. In figure 2.11 the hump is now placed 'out of phase' with the point vortex and the trough of the interface corresponds to the point vortices horizontal position. The amplitude
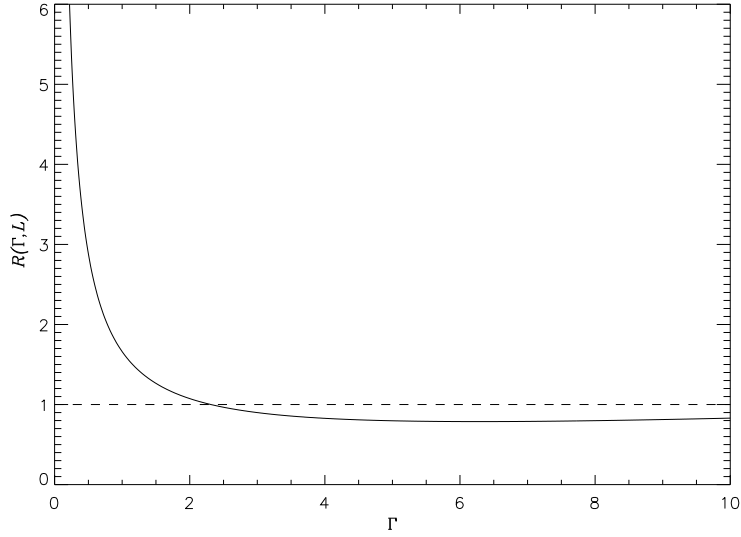
Figure 2.8: $R(\Gamma, L)$ (solid line) against $\Gamma$ for $L = 2\pi$. For values of $\Gamma$ where $R(\Gamma, L)$ is above the dashed line, solutions to the quadratic in $U$ are real and therefore physically permissible. In the region where $R(\Gamma, L) < 1$ no real solutions for $U$ exist. This region roughly corresponds to $\Gamma > 2.31$.

of waves upon the interface are however large and the trough actually 'engulfs' the point vortex. The amplitude of the interfacial waves increases as $\Gamma$ increases. In figure 2.12 the interfacial trough is again placed directly above the point vortex and the interfacial shapes lie entirely above $y = 0$. These configurations have similarities to the Karman vortex street (von Karman and Rubach 1913) in which the upper row of vortices is desingularised into patches.

Figures 2.13 and 2.14 show the interface shapes for $L = 2\pi$ with $U$ taken as the negative and positive root of (2.59) respectively. For low values of $\Gamma$, figure 2.13 shows that the interfacial shapes are similar to those seen in figure 2.9. As $\Gamma$ increases the amplitude of the interface increases and higher order modes again become more prevalent in the interface shape. The interfacial shapes seen in figure 2.14 mirror
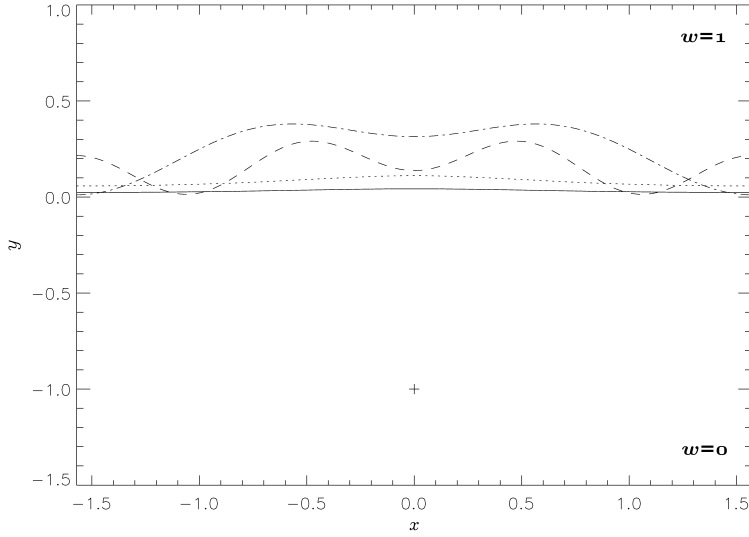
Figure 2.9: Shapes of the interface $\eta(x)$ for $L = \pi$ over one period of $-L/2$ to $L/2$ for values of $\Gamma < 1.07$. All $\eta(x)$ in this figure are evaluated using the 'lower' root of $U$ (see 2.59) and are truncated after the first 50 terms of the Fourier series. The solid line is for $\Gamma = 0.1$ and $U = 0.017$, the dotted line for $\Gamma = 0.25$ and $U = 0.042$, the dashed line for $\Gamma = 0.5$ and $U = 0.084$ and the dotted and dashed line for $\Gamma = 0.8$ and $U = 0.137$. The $+$ represents the point vortex location.

closely those of figure 2.10.

Figures 2.9-2.14 show a wide range of interfacial shapes given by linear theory. However, in many of the configurations shown, the amplitude of the interfacial wave is large. In such situations, linear theory is not expected to be a good guide as to what non-linear shapes may exist. In figure 2.9 when $\Gamma = 0.1$ and $\Gamma = 0.25$ small amplitude waves are present on the interface with the primary mode being the dominant one. It is therefore expected that in these circumstances linear theory is a 'good' guide as to what non-linear shapes can be seen. For $\Gamma = 0.5$ and $\Gamma = 0.8$ in figure 2.9, although the amplitude of the interfacial waves is not particularly large, higher order modes are now playing a significant role in the interfacial shape. Therefore, if corresponding
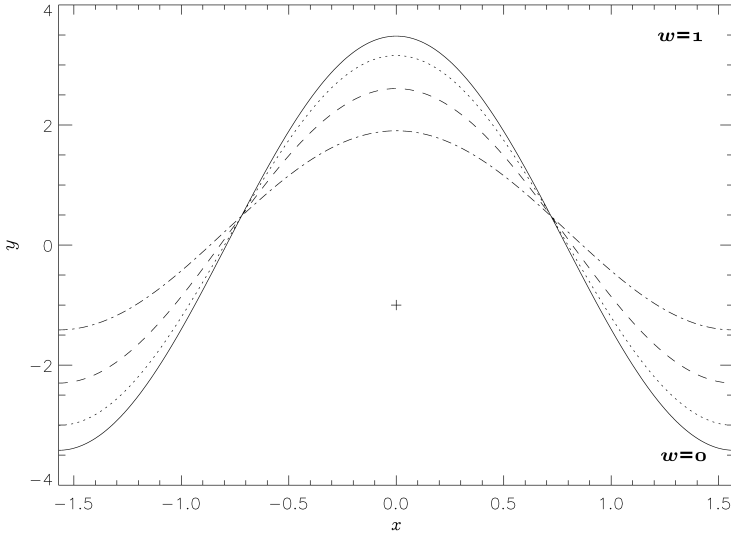
Figure 2.10: Shapes of the interface $\eta(x)$ for $L = \pi$ over one period of $-L/2$ to $L/2$ for values of $\Gamma < 1.07$. All $\eta(x)$ in this figure are evaluated using the 'higher' root of $U$ (see 2.59) and are truncated after the first 50 terms of the Fourier series. The solid line is for $\Gamma = 0.1$ and $U = 0.249$, the dotted line for $\Gamma = 0.25$ and $U = 0.248$, the dashed line for $\Gamma = 0.5$ and $U = 0.245$ and the dotted and dashed line for $\Gamma = 0.8$ and $U = 0.240$. The + represents the point vortex location.

non-linear shapes do exist, they are likely to be more unstable and therefore difficult to find numerically as many 'more' stable shapes will lie in their vicinity. Figure 2.11 shows a situation where interfacial waves are of very large amplitude and the interface actually crosses the point vortex. The vortex would now lie in the vortical region of the flow and this, along with the large amplitude of the waves, invalidate the linear theory.

The shapes in figure 2.12 represent the 'out of phase' versions of some interface shapes seen in figure 2.9 (i.e. the interface trough is now aligned with the vortex in place of the peak) and resemble a 'partially' desingularised Karman vortex street. The amplitude of these interfacial waves is however quite large bringing into question
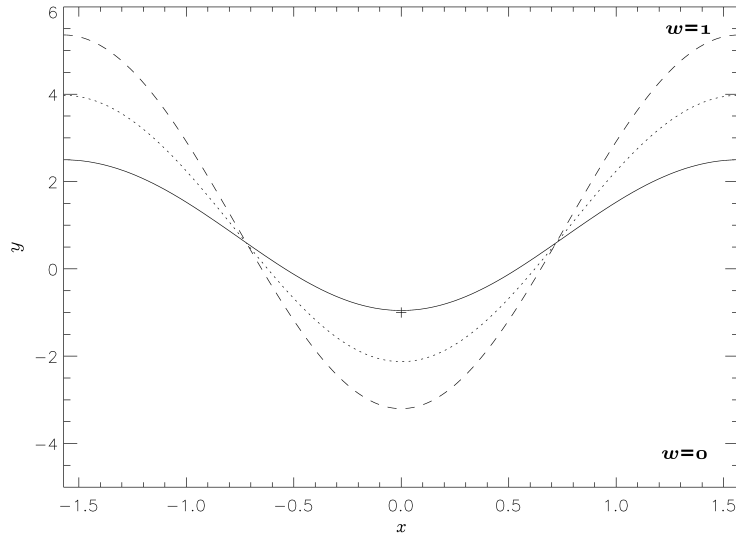
Figure 2.11: Shapes of the interface $\eta(x)$ for $L = \pi$ over one period of $-L/2$ to $L/2$ for values of $\Gamma > 2.30$. All $\eta(x)$ in this figure are evaluated using the 'lower' root of $U$ (see 2.59) and are truncated after the first 50 terms of the Fourier series. The solid line is for $\Gamma = 3.0$ and $U = 0.271$, the dotted line for $\Gamma = 3.5$ and $U = 0.268$ and the dashed line for $\Gamma = 4.0$ and $U = 0.266$. The + represents the point vortex location.

the validity of the linear theory (that requires $\eta \ll 1$). Nonetheless, the linear theory

still gives an indication that such shapes may exist. Corresponding non-linear shapes

to those discussed here are analysed numerically in the following chapter.
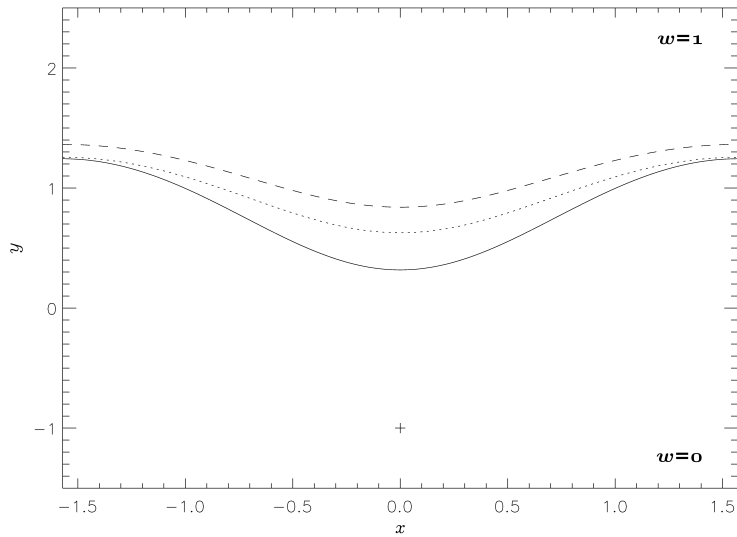
Figure 2.12: Shapes of the interface $\eta(x)$ for $L = \pi$ over one period of $-L/2$ to $L/2$ for values of $\Gamma > 2.30$. All $\eta(x)$ in this figure are evaluated using the 'higher' root of $U$ (see 2.59) and are truncated after the first 50 terms of the Fourier series. The solid line is for $\Gamma = 3.0$ and $U = 0.456$, the dotted line for $\Gamma = 3.5$ and $U = 0.539$ and the dashed line for $\Gamma = 4.0$ and $U = 0.621$. The + represents the point vortex location.
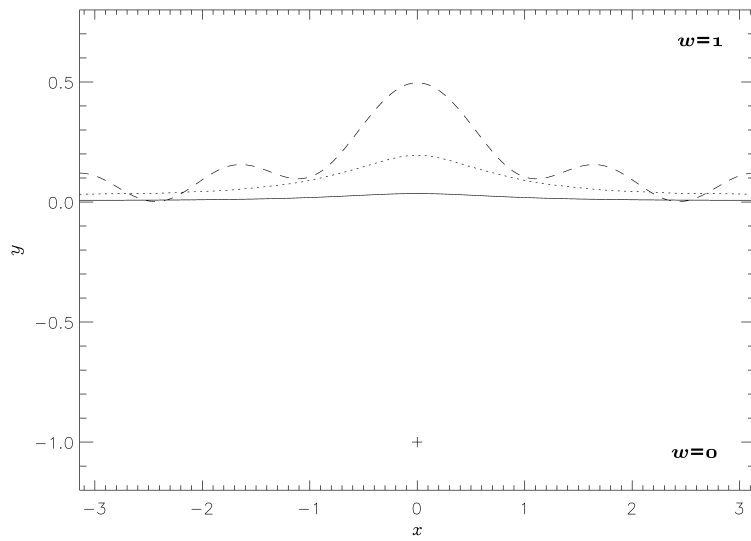
Figure 2.13: Shapes of the interface $\eta(x)$ for $L = 2\pi$ over one period of $-L/2$ to $L/2$ for $0 < \Gamma < 2.31$. All $\eta(x)$ in this figure are evaluated using the 'lower' root of $U$ (see 2.59) and are truncated after the first 50 terms of the Fourier series. The solid line is for $\Gamma = 0.1$ and $U = 0.010$, the dotted line for $\Gamma = 0.5$ and $U = 0.054$ and the dashed line for $\Gamma = 1.0$ and $U = 0.115$. The + represents the point vortex location.
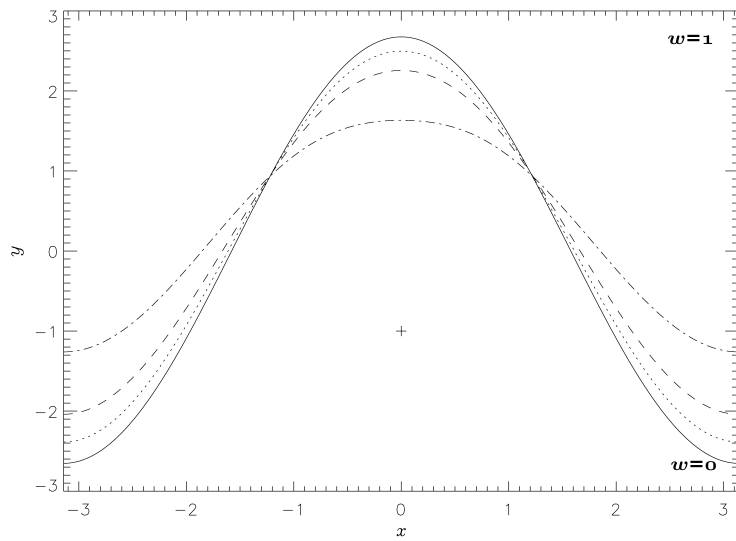
Figure 2.14: Shapes of the interface $\eta(x)$ for $L = 2\pi$ over one period of $-L/2$ to $L/2$ for $0 < \Gamma < 2.31$. All $\eta(x)$ in this figure are evaluated using the 'higher' root of $U$ (see 2.59) and are truncated after the first 50 terms of the Fourier series. The solid line is for $\Gamma = 0.1$ and $U = 0.498$, the dotted line for $\Gamma = 0.5$ and $U = 0.488$, the dashed line for $\Gamma = 1.0$ and $U = 0.473$ and the dotted and dashed line for $\Gamma = 2.0$ and $U = 0.420$. The $+$ represents the point vortex location.

## 2.2.2  Vortices in the rotational flow region

Consider a shear flow with vorticity jump $\tilde{\omega} = -1$ at $y = 0$ such that the velocity field in the absence of point vortices is given by

$$u - iv = \begin{cases} U, & y > 0, \\ U + y, & y < 0. \end{cases} \tag{2.62}$$

Compare this to (2.31): now the vortical region lies below $y = 0$. An infinite row of periodic point vortices with circulation $\Gamma$ are placed at $r_n = (nL, -1)$ ($n \in \mathbb{Z}$) and are now located in the rotational region of the flow. The analysis of this system is very similar to that of section 2.2.1. The condition on the vortical interface is unchanged and the condition to render $u_{loc} = 0$ is modified to

$$U - 1 - \frac{1}{2\pi} \int_{-\infty}^{\infty} \frac{\eta(x')}{x'^2 + 1} dx' = 0. \tag{2.63}$$

Following the method of section 2.2.1, with the interface condition unchanged and (2.35) modified to (2.63) leads to an equation for $U$ given by

$$2(U - 1) + \frac{\Gamma}{L} \left( \sum_{n=1}^{\infty} \frac{e^{-\frac{4n\pi}{L}}}{\frac{2n\pi U}{L} - \frac{1}{2}} - 1 \right) = 0. \tag{2.64}$$

Truncating (2.64) for various $n = N$ and solving the resultant $(N+1)^{th}$ order polynomial it is seen that once $L$ is fixed, all but one root (for a given value for $\Gamma$) leads to resonance. The root that does not lead to resonance is the only root with $U > 1$ and corresponds to the positive root of the quadratic obtained from truncating (2.63) at $n = 1$. Thus in the figures that follow, (2.64) was truncated at $n = 4$ to obtain a value of the root with $U > 1$ accurate to at least three decimal places. Again, to gauge for which values of $\Gamma$ 'useful' solutions of (2.64) may exist it is useful to consider the

function $R(\Gamma, L)$. Truncating (2.64) at $n = 1$ and rearranging gives

$$U = \left[\frac{L}{8\pi} + \frac{\Gamma}{4L} + \frac{1}{2}\right] \pm \frac{1}{2}\left[\left(\frac{L}{4\pi} + \frac{\Gamma}{2L} + 1\right)^2 - \left(\frac{\Gamma}{\pi}e^{-\frac{4\pi}{L}} + \frac{\Gamma}{2\pi} + \frac{L}{\pi}\right)\right]^{\frac{1}{2}}, \quad (2.65)$$

and thus

$$R(\Gamma, L) = \frac{\left(\frac{L}{4\pi} + \frac{\Gamma}{2L} + 1\right)^2}{\frac{\Gamma}{\pi}e^{-\frac{4\pi}{L}} + \frac{\Gamma}{2\pi} + \frac{L}{\pi}}. \quad (2.66)$$

$R(\Gamma, L)$ is plotted against $\Gamma$ in figures 2.15 and 2.16 for $L = \pi$ and $L = 2\pi$ respectively. For both $L = \pi$ and $L = 2\pi$ and $\Gamma > 0$ the function $R(\Gamma, L)$ is always greater than one and thus 'useful' linear solutions may exist for all positive values of $\Gamma$.
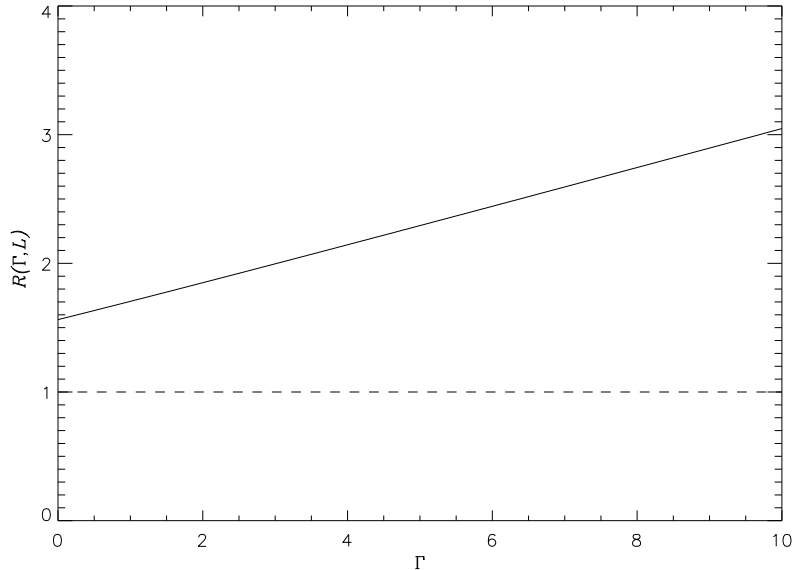


Figure 2.15: $R(\Gamma, L)$ (solid line) as a function of $\Gamma$ for $L = \pi$. In the region between $0 < R < 1$ represented by the horizontal axis and the dashed line, solutions of $U$ will be complex.

Using (2.39), with the sum truncated at $k = 50$, shapes of $\eta(x)$ are evaluated for $L = \pi$ and $L = 2\pi$: shown in figures 2.17 and 2.18 respectively. For $L = \pi$ the actual amplitude of the interfacial oscillation is small for all values of $\Gamma$. As $\Gamma$ is increased and
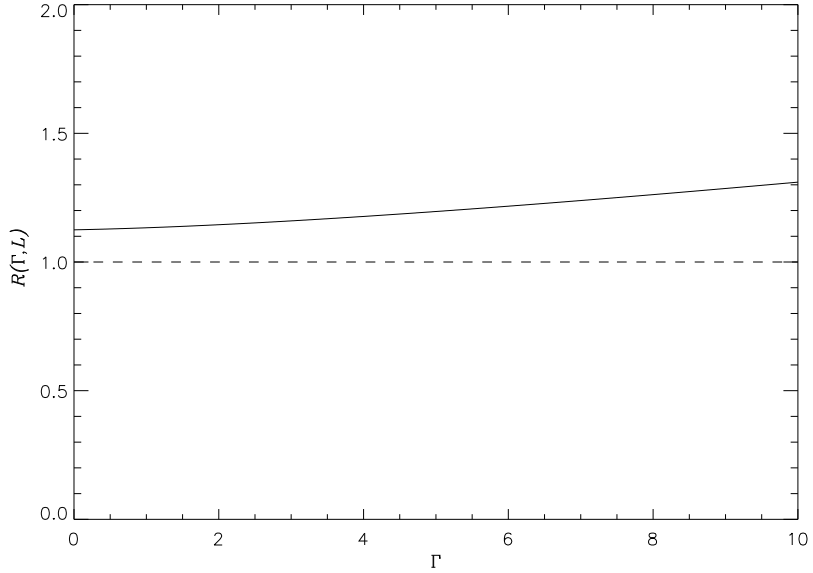
Figure 2.16: $R(\Gamma, L)$ (solid line) as a function of $\Gamma$ for $L = 2\pi$. In the region between $0 < R < 1$ represented by the horizontal axis and the dashed line, solutions of $U$ will be complex.

the uniform background velocity $U$ increases the interface essentially moves further away from the point vortices. As this shift occurs there is only a small increase in the amplitude of the wave present on the interface. However, for $L = 2\pi$ this is not the case. As $\Gamma$ is increased, although the minimum $y$-height of the interface increases, the amplitude of the interfacial wave increases to a much greater extent than in the $L = \pi$ case. These interface shapes again resemble a Karman vortex street with the upper row of vortices desingularised. As the amplitude of the interfacial oscillations remain relatively small in the situations considered here, $L = \pi$ and $L = 2\pi$, it is expected that linear theory will be a good guide as to what non-linear shapes can be expected across a range of $\Gamma$.
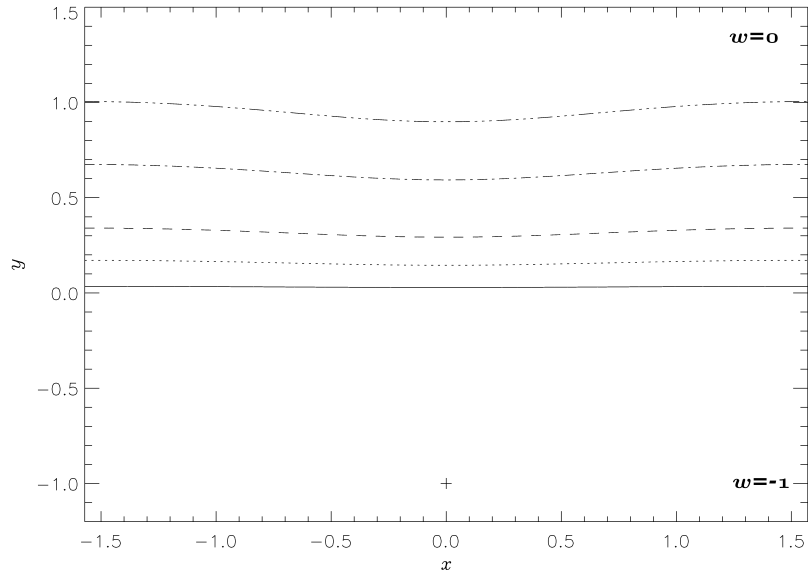
Figure 2.17: Shapes of the interface $\eta(x)$ for $L = \pi$ over one period of $-L/2$ to $L/2$. All $\eta(x)$ in this figure are evaluated using the positive root of $U$ (see 2.64) and are truncated after the first 50 terms of the Fourier series. The solid line represents $\Gamma = 0.1$ and $U = 1.016$, the dotted line for $\Gamma = 0.5$ and $U = 1.079$, the dashed line $\Gamma = 1.0$ and $U = 1.158$, the dot-dash line $\Gamma = 2.0$ and $U = 1.316$ and finally the three-dot-dash line $\Gamma = 3.0$ and $U = 1.474$. The $+$ represents the point vortex location.
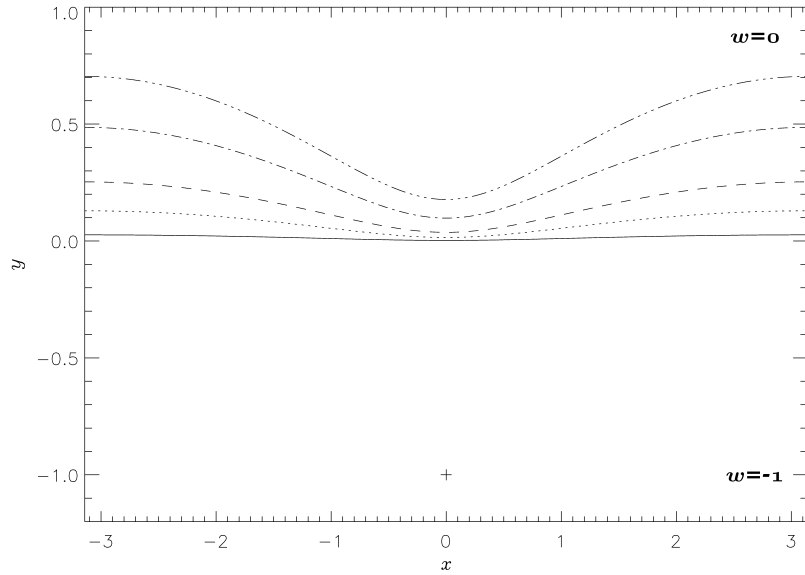
Figure 2.18: Shapes of the interface $\eta(x)$ for $L = 2\pi$ over one period of $-L/2$ to $L/2$. All $\eta(x)$ in this figure are evaluated using the positive root of $U$ (see 2.64) and are truncated after the first 50 terms of the Fourier series. The solid line represents $\Gamma = 0.1$ and $U = 1.006$, the dotted line for $\Gamma = 0.5$ and $U = 1.029$, the dashed line $\Gamma = 1.0$ and $U = 1.059$, the dot-dash line $\Gamma = 2.0$ and $U = 1.123$ and finally the three-dot-dash line $\Gamma = 3.0$ and $U = 1.189$. The + represents the point vortex location.

## 2.3   Vortex street in a shear flow

Similar to section 2.2, linear equilibria can also be constructed for the situation where a vortex street (i.e. staggered rows of opposite-signed vortices) lies in a shear flow. Here, the form of the shear flow is given by equations (2.5) and (2.6) i.e. in the absence of point vortices

$$
u = \begin{cases} U - y/2 & y > 0, \\ U + y/2 & y < 0. \end{cases} \tag{2.67}
$$

Point vortices of equal but opposite circulations are periodically placed at $(-L/4 \pm nL, -1)$ and $(L/4 \pm nL, 1)$, where $n \in \mathbb{Z}^+$. A schematic of the system is shown in figure 2.19. Here, the circulation of the vortices, $\Gamma$, is not restricted to being positive but instead can be of arbitrary sign. Due to the anti-symmetric nature of the configuration, the interfacial contour, $\eta(x)$, will also be anti-symmetric on $[-L/2, L/2]$. This ensures that the $y$-direction velocity at the point vortices is zero.

The streamfunction for the interfacial disturbance is again given by equation (2.32). The streamfunction $\psi_{\mathrm{pv}}$ owing to the periodic array of point vortices is

$$
\psi_{\mathrm{pv}} = \frac{\gamma}{4\pi} \log \left[ \sin^2 \left( \frac{\pi}{L}(x - x_{loc}) \right) + \sinh^2 \left( \frac{\pi}{L}(y - y_{loc}) \right) \right], \tag{2.68}
$$

where $\gamma$ is the circulation of the vortices, $L$ is the period of the configuration and $(x_{loc}, y_{loc})$ position of one of the vortices. Here the region between $L/2$ and $L/2$ is being considered and thus $x_{loc} \in [-L/2, L/2)$. The condition to render the vortices
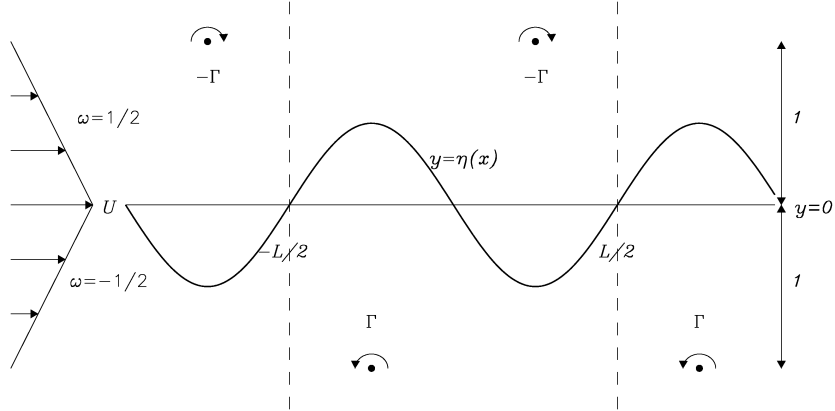
Figure 2.19: Schematic of the problem under consideration. A shear flow is present with vorticity jump $\tilde{\omega} = -1$ such that $\omega = 1/2$ in $y > 0$ and $\omega = -1/2$ in $y < 0$ and the velocity is $U$ at $y = 0$. Point vortices of circulation $\Gamma$ and $-\Gamma$ are placed periodically at $(-L/4 \pm nL, -1)$ and $(L/4 \pm nL, 1)$ respectively, where $n \in \mathbb{Z}^+$. The fluid disturbance along the vorticity interface is labelled as $y = \eta(x)$.

in $y < 0$ stationary is given by

$$U - \frac{1}{2} + \frac{1}{2\pi}\frac{\partial}{\partial y}\int_{-\infty}^{\infty}\int_{0}^{\eta(x')}\left[\left((x-x')^2 + (y-y')^2\right)^{1/2}\right]dy'dx'\Bigg|_{(-L/4,-1)} + $$

(2.69)

$$\frac{\Gamma}{4\pi}\frac{\partial}{\partial y}\log\left[\sin^2\left(\frac{\pi}{L}(x-L/4)\right) + \sinh^2\left(\frac{\pi}{L}(y-1)\right)\right]\Bigg|_{(-L/4,-1)} = 0.$$

Using the linear approximation $|\eta| \ll 1$ gives

$$U - \frac{1}{2} - \frac{1}{2\pi}\int_{-\infty}^{\infty}\frac{\eta(x')}{(L/4+x')^2+1}dx' - \frac{\Gamma}{2L}\tanh\left(\frac{2\pi}{L}\right) = 0. \qquad (2.70)$$

Due to the anti-symmetry of the problem, (2.70) also ensures that the vortices in

$y > 0$ are also rendered stationary. Now consider the condition on the vortical

interface (again given by (2.9)) which yields

$$U\frac{\partial \eta}{\partial x} = \frac{1}{2\pi}\frac{\partial}{\partial x}\left[-\int_{-\infty}^{\infty}\int_{0}^{\eta(x')}\log\left[\left((x-x')^2+(-y')^2\right)^{1/2}\right]dy'dx'\right.$$

$$\left. +\frac{\Gamma}{2}\left(\log\left[\sin^2\left(\frac{\pi}{L}(x+L/4)\right)+\sinh^2\left(\frac{\pi}{L}y\right)\right]\right.\right. \tag{2.71}$$

$$\left.\left. -\log\left[\sin^2\left(\frac{\pi}{L}(x-L/4)\right)+\sinh^2\left(\frac{\pi}{L}(-1)\right)\right]\right)\right].$$

After some algebra, (2.71) simplifies to give

$$U\frac{\partial \eta}{\partial x} = \frac{-1}{2\pi}\int_{-\infty}^{\infty}\frac{\eta(x')}{x-x'}dx' + \frac{\Gamma\beta}{L}\frac{\cos(2\pi x/L)}{\beta^2-\sin^2(2\pi x/L)}, \tag{2.72}$$

where $\beta = \cosh(2\pi/L)$. The interface shape, $\eta(x)$, which is anti-symmetric on $[-L/2, L/2]$ can be written as a Fourier series given by

$$\eta(x) = \sum_{n=1}^{\infty} b_n \sin\frac{2\pi n x}{L}, \tag{2.73}$$

where

$$b_n = \frac{4}{L}\int_{0}^{L/2}\eta(x)\sin\frac{2\pi n x}{L}dx. \tag{2.74}$$

Note owing to the imposed antisymmetry the net circulation is zero. There was no need to impose this condition as was done in section 2.2. Following the method of section 2.2, the forcing term at the interface owing to the point vortices is also written as a Fourier series, here given by

$$g(x) = \frac{\Gamma\beta}{L}\frac{\cos(2\pi x/L)}{\beta^2-\sin^2(2\pi x/L)} = \sum_{k=1}^{\infty} a_k \cos\frac{2\pi k x}{L}, \tag{2.75}$$

where

$$a_k = \frac{2\pi\Gamma\beta}{L^2}\int_{-L/2}^{L/2}\frac{\cos(2\pi x/L)\cos(2\pi k x/L)}{\beta^2-\sin^2(2\pi x/L)}dx = \frac{2\Gamma\beta}{\pi L}\int_{0}^{\pi}\frac{\cos z\cos kz}{\beta^2-\sin^2 z}dz. \tag{2.76}$$

Substituting (2.73) and (2.75) into (2.72) gives

$$\sum_{n=1}^{\infty} \frac{2\pi n U}{L} b_n \cos \frac{2\pi n x}{L} = -\frac{1}{2\pi} \sum_{n=1}^{\infty} \int_{-\infty}^{\infty} b_n \frac{\sin(2\pi n x'/L)}{x - x'} dx' + \sum_{n=1}^{\infty} a_n \cos \frac{2\pi n x}{L}. \quad (2.77)$$

From the result of (2.49), evaluating the integral on the right hand side of (2.77) gives

$$\int_{-\infty}^{\infty} \frac{\sin(2\pi n x'/L)}{x - x'} dx = -\pi \cos \frac{2\pi n x}{L}. \quad (2.78)$$

A relationship between the constants $a_n$ and $b_n$ is therefore given by

$$b_n = \frac{a_n}{\frac{2\pi n U}{L} - \frac{1}{2}}. \quad (2.79)$$

Again, as in (2.50), when $2\pi n U/L \simeq 1/2$ resonance will occur. Finally, in order to resolve $U$ and thus the interfacial shapes $\eta(x)$, (2.73) is substituted into (2.70) giving

$$U - \frac{1}{2} - \frac{1}{2\pi} \int_{-\infty}^{\infty} \sum_{n=1}^{\infty} b_n \frac{\sin(2\pi n x')}{(L/4 + x')^2 + 1} dx' - \frac{\alpha \Gamma}{2L} = 0, \quad (2.80)$$

where $\alpha = \tanh(2\pi/L)$. To evaluate the integral on the left hand side of (2.80) let $\zeta = L/4 + x'$ giving

$$\int_{-\infty}^{\infty} \frac{\sin(2\pi n x')}{(L/4 + x')^2 + 1} dx' = \Im \left[ e^{-in\pi/2} \int_{-\infty}^{\infty} \frac{e^{i2\pi n \zeta/L}}{\zeta^2 + 1} d\zeta \right] \quad (2.81)$$

$$= -\pi e^{-2\pi n/L} \sin \frac{n\pi}{2}.$$

Using the result of (2.81) in (2.80), the equation for $U$ is given by

$$U - \frac{1}{2} - \frac{\alpha \Gamma}{2L} + \frac{1}{2} \sum_{n=1}^{\infty} b_n e^{-2\pi n/L} \sin \frac{n\pi}{2} = 0. \quad (2.82)$$

Note that due to the $\sin(n\pi/2)$ term in the summation, only $b_n$ for odd $n$ will contribute to (2.82). Following the method and reasoning of section 2.2, that is, the

relevant roots of $U$ can again be obtained from truncating (2.82) at $n = 1$ and solving the resultant quadratic, and using equation (2.79) in (2.82), gives

$$U - \frac{1}{2} - \frac{\alpha\Gamma}{2L} + \frac{1}{2}\frac{a_1}{\frac{2\pi U}{L} - \frac{1}{2}}e^{-2\pi/L} = 0. \tag{2.83}$$

Rearranging (2.83) gives

$$U = \left(\frac{L}{8\pi} + \frac{1}{4} + \frac{\alpha\Gamma}{4L}\right) \pm \frac{1}{2}\left[\left(\frac{L}{4\pi} + \frac{1}{2} + \frac{\alpha\Gamma}{2L}\right)^2 - \left(\frac{\alpha\Gamma + L}{2\pi} + \frac{2\beta\Gamma}{\pi^2}\hat{a}_1 e^{-2\pi/L}\right)\right]^{\frac{1}{2}}, \tag{2.84}$$

where

$$\hat{a}_1 = \int_0^\pi \frac{\cos^2 z}{\beta^2 - \sin^2 z}dz. \tag{2.85}$$

Here, due to the $\sin(n\pi/2)$ term in (2.82), values of $U$ accurate to three significant figures can be obtained from truncating the sum at $n = 1$ and solving the resultant quadratic, i.e. there is no need to solve a higher order polynomial to achieve this accuracy as was done in section 2.2. Again, to gauge for which values of $\Gamma$ physically permissible solutions of $U$ may exist consider the function

$$R(\Gamma, L) = \frac{\left(\frac{L}{4\pi} + \frac{1}{2} + \frac{\alpha\Gamma}{2L}\right)^2}{\frac{\alpha\Gamma + L}{2\pi} + \frac{2\beta\Gamma}{\pi^2}\hat{a}_1 e^{-2\pi/L}}. \tag{2.86}$$

Solutions for $U$ will be non-complex, and therefore physically permissible, for $R(\Gamma, L) \leq 0$ or $R(\Gamma, L) \geq 1$. Plots of the function $R(\Gamma, L)$ against $\Gamma$ are shown in figures 2.20 and 2.21 for $L = \pi$ and $L = 2\pi$ respectively. Figure 2.20 shows that for the case when $L = \pi$, solutions of (2.84) will be real for all $\Gamma \in \Re$. When $L = 2\pi$, shown in figure 2.21, it is seen that solutions of (2.84) are real except in the region $0 < \Gamma < 23.57$. However, for $\Gamma = O(10)$, large amplitude waves will be excited on the vortical interface invalidating the use of linear theory which requires $|\eta| \ll 1$. Therefore, somewhat

surprisingly, in this case ($L = 2\pi$) in the linear limit of small amplitude interfacial waves, $\Gamma$ is required to be negative.
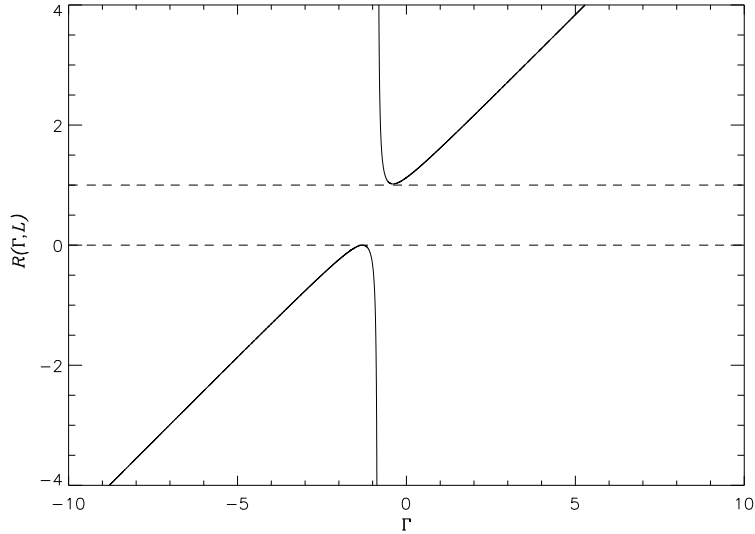


Figure 2.20: $R(\Gamma, L)$ (solid line) as a function of $\Gamma$ for $L = \pi$. In the region between the dashed lines, $0 < R(\Gamma, L) < 1$, no real solutions of $U$ exist. Here, solutions of $U$ are real for all $\Gamma \in \Re$.

Using (2.76), (2.79) and (2.84) the interface shapes $\eta(x)$ are determined. When evaluating $\eta(x)$, the sum in (2.73) was truncated at $n = 50$. Plots of $\eta(x)$ for $L = \pi$ are shown in figures 2.22 and 2.23 for $U$ evaluated taking the negative and positive roots of (2.84) respectively. In figure 2.22, curves of $\eta(x)$ are plotted for $\Gamma = -4$, (for which $U = -0.144$) and $\Gamma = -2$, (for which $U = 0.140$). This leads to a situation where the interface 'sinks' towards each point vortex. For both values of $\Gamma$, the velocity due to $U$ and the effect of the shear flow will be negative at each point vortex (since $U < 1/2$ in both cases). Thus, for a stationary configuration the velocity fields owing to the interfacial disturbance and the other point vortex need to cancel exactly with this velocity field. Having the interface deform towards the
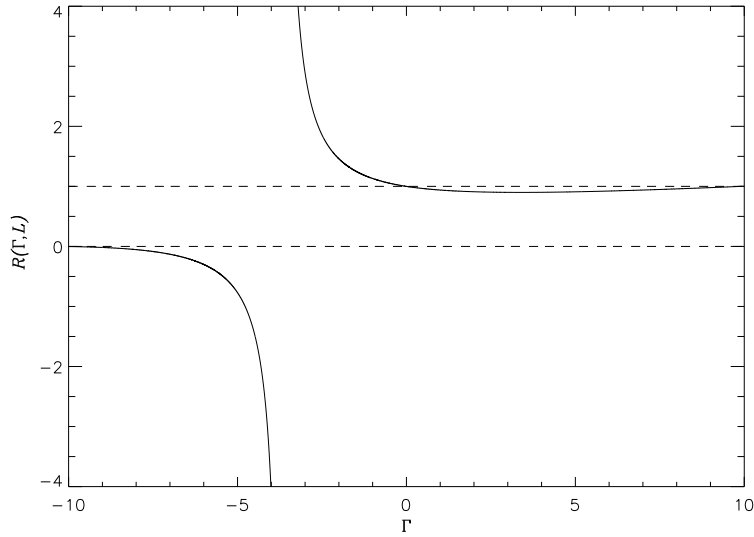
Figure 2.21: $R(\Gamma, L)$ (solid line) as a function of $\Gamma$ for $L = 2\pi$. In the region between the dashed lines, $0 < R(\Gamma, L) < 1$, no real solutions of $U$ exist. Here, solutions for $U$ will be real for $\Gamma$ not in the region $0 < \Gamma < 23.57$.

point vortices results in the contributions to the velocity field from the interfacial disturbance and the other vortex both being in the positive $y$-direction. For the case when $\Gamma = -1$, the contribution from the other point vortex is comparatively large and only a small amplitude disturbance at the interface is necessary to render the configuration stationary. When $\Gamma = -2$ the other vortex contribution is smaller and a larger amplitude interfacial disturbance is now required for a stationary configuration. For $L = \pi$, when $\Gamma$ is close to zero and when $\Gamma > 0$, evaluating equation (2.84) gives $U \simeq 0.25$, the condition for an $n = 1$ resonance. Thus for $\Gamma$ in this region the amplitude of interfacial waves is large and linear theory is not applicable.

When evaluating $U$ for $L = \pi$ taking the positive root of (2.84), negative $\Gamma$ leads to an interfacial disturbance in the opposite direction to the case previously considered, i.e. the interface moves 'away' from each point vortex. However, for

positive values of $\Gamma$ there is a small disturbance at the interface towards the point vortices (as previously seen for negative values of $\Gamma$). Figure 2.23 shows the shapes of $\eta(x)$ for $\Gamma = -1/2$, $\Gamma = -1/4$ and $\Gamma = 1/2$ in this case. As $\Gamma$ is increased the amplitude of the interfacial disturbance also increases. As a quick check of the validity of linear theory, consider the interface given by the dotted line in figure 2.23. In this case, the interface is nearly flat and therefore at the point vortices the velocity owing to the interfacial disturbance will be small. In the absence of the vorticity interface and any ambient flows, the vortex street of figure 2.23 with $\Gamma = 1/2$ will steadily translate with $u = -0.077$. Therefore, to render the configuration stationary a contribution to the velocity field at the point vortices of $u = 0.005$ is required from the interfacial disturbance. Considering the shape of the interface in question this is a sensible value. Note that, as in section 2.2, high order resonances can again be seen in this system for certain values of $\Gamma$ and $U$. However, as linear theory is not valid in such situations no such corresponding interface shapes are shown here (or in the following figures of this section).

Interfacial shapes with a period of $L = 2\pi$ are shown for $U$ evaluated using the negative and positive roots of (2.84) in figures 2.24 and 2.25 respectively. Here, only negative values of $\Gamma$ are considered as solutions of (2.84) for $0 < \Gamma < 23.57$ are complex and thus not physically permissible. Figure 2.24 shows the 'corresponding' interface shapes to those of figure 2.22. The interface shapes seen in figure 2.24 are similar in shape to those of figure 2.22, however in contrast, as $\Gamma$ increases the amplitude of the interfacial wave also increases. When $L = 2\pi$ and $U$ is evaluated using the positive root of equation (2.84) the system exhibits similar behaviour to the corresponding
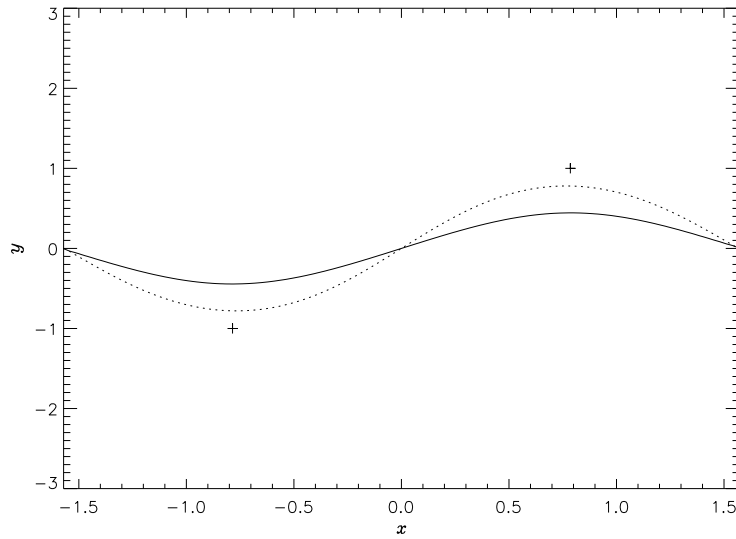
Figure 2.22: Plots of $\eta(x)$ for $L = \pi$ and $U$ evaluated using the negative root of (2.84). The solid line represents $\Gamma = -4$ (for which $U = -0.144$) and the dashed line $\Gamma = -2$ (for which $U = 0.140$).

$L = \pi$ system.

## 2.4  Summary

Point vortex equilibria near a vortical interface have been derived in the linear limit of small amplitude oscillations at the interface. The jump in vorticity across the interface was provided by a shear flow. The first configuration considered was the anti-symmetric analogue of that considered in McDonald (2004), that is, two vortices of equal but opposite circulations located either side of a vorticity interface. For this configuration, no equilibrium states could be found in the linear limit. The conditions necessary to render both point vortices stationary resulted in large amplitude oscillations at the interface that engulfed the point vortices rendering linear theory
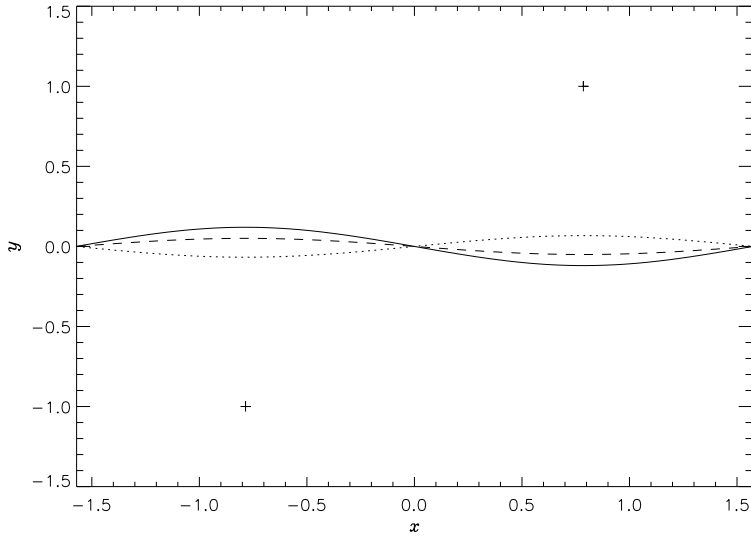
Figure 2.23: Plots of $\eta(x)$ for $L = \pi$ and $U$ evaluated using the positive root of (2.84). The solid line represents $\Gamma = -1/2$ (for which $U = 0.431$), the dashed line $\Gamma = -1/4$ (for which $U = 0.465$) and the dotted line $\Gamma = 1/2$ (for which $U = 0.572$).

invalid. Although linear theory can serve as a guide in searching for corresponding non-linear equilbria this non-result cannot rule out their existence.

Three configurations with periodic arrays of vortices near an interface were then considered. The first was an array of symmetric vortices located in the irrotational region of the flow. The problem depends on the parameters $\Gamma$, $U$ and $L$ which are the point vortex circulation, free-stream velocity and periodicity of the domain respectively. One method of obtaining solutions is to represent the interface as a Fourier series. This results in $U$ being given by a transcendental function dependent on $\Gamma$ and $L$. Solutions of $U$ are obtained by approximating the function as an $N$th order polynomial and solving for $U$. Many of the solutions of $U$ were complex or led the resonance and thus a condition was derived that served as a guide as to where physically permissible values of $U$ may be obtained. A vast array of interfacial shapes
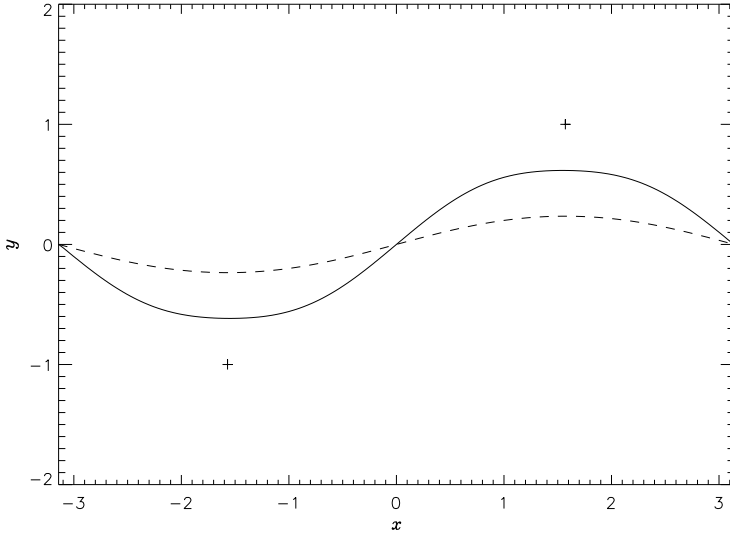
Figure 2.24: Plots of $\eta(x)$ for $L = 2\pi$ and $U$ evaluated using the negative root of (2.84). The solid line represents $\Gamma = -1$ (for which $U = 0.320$) and the dashed line $\Gamma = -0.1$ (for which $U = 0.450$).

exist for the possible values of $\Gamma$, $U$ and $L$. Many solutions lead to resonance and large amplitude oscillations at the interface bringing into question the validity of linear theory. However, for small $\Gamma$, some solutions are seen in which there exists a small amplitude hump at the interface, placed symmetrically above the point vortex. Also, some solutions were seen in which the interface amplitude remained relatively small and higher order modes were playing a significant role in the interface shape.

Next, the above configuration with the vortices now placed in the rotational region of the flow was considered. The method of solution closely parallels that of the previous configuration. Solutions in which linear theory is expected to be a good guide now have a hump at the interface placed out of phase with the point vortex, resembling a Von-Karman vortex street one row of vortices desingularised. For small $L$, interface shapes tended to be higher and flatter i.e. the interface would have a
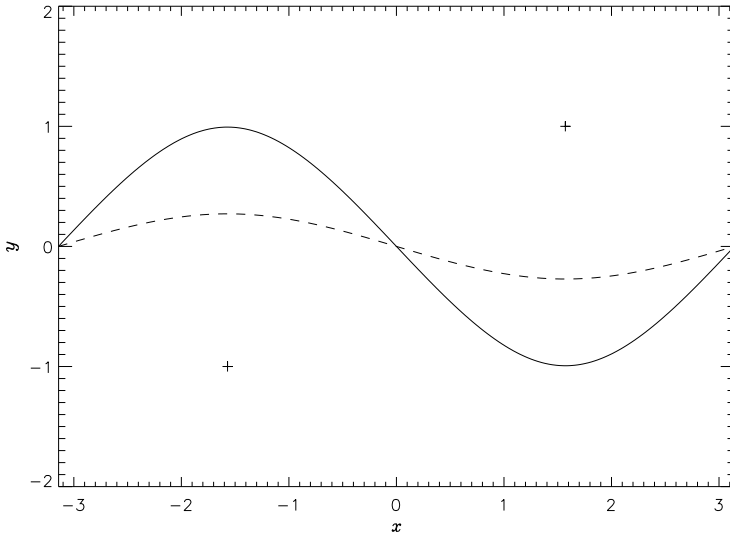
Figure 2.25: Plots of $\eta(x)$ for $L = 2\pi$ and $U$ evaluated using the positive root of (2.84). The solid line represents $\Gamma = -1$ (for which $U = 0.620$) and the dashed line $\Gamma = -0.1$ (for which $U = 0.544$).

small amplitude oscillation and be at a greater vertical distance from the point vortex.

The final configuration considered was that of a vortex street in a shear flow. The method of solution is again very similar to that of the previous two configurations but now with an extra point vortex per period. Also, for this problem, both positive and negative values of $\Gamma$ were considered. In general, interface shapes resembled sine waves over one period. Solutions exist in which the interface curves towards and away from the vortices, i.e. the interface can resemble a positive or negative sine wave. Either situation could occur for both positive and negative values of $\Gamma$. However, for larger values of $L$, for example $L = 2\pi$, no linear equilibria could be found for which $\Gamma > 0$.

The linear equilibria derived in this chapter will motivate and help the search for non-linear equilibria in chapter 3. It has been shown that a range of linear equilibria are possible for the configurations considered and it is expected that some of the

possible non-linear equilibria will be similar in shape. Thus, initially, in chapter 3, the linear equilibria derived here will be used to initialise the non-linear computations.

# Chapter 3

# Computation of non-linear equilibria on a vortical interface

In this chapter the corresponding non-linear equilibria to those found in the linear limit of small amplitude interfacial oscillations in chapter 2 are computed numerically. To examine these non-linear equilibria a numerical procedure based on that of McDonald (2004) is used. In general, the procedure entails using Newton's method to iterate the vortical interface to a shape such that is has a constant value of the streamfunction along it (i.e. the interface becomes a streamline) and the velocity at all point vortices vanishes. In iterating the interface towards a streamline, the parameters $\Gamma$ and $U$ and, depending on the system under consideration, possibly an extra parameter measuring the vortex separation will also be calculated. When calculating symmetric equilibria (c.f. chapter 2.2) the vortex position will remain fixed and when calculating anti-symmetric equilibria (c.f. chapter 2.3) the distance of the vortices from the interface will remain fixed. The vorticity distributions under consideration

are piecewise constant, enabling the use of a contour dynamics algorithm (Dritschel (1989)) to calculate the velocity field owing to the vorticity interface. For the planar anti-symmetric system considered in chapter 2.1, a planar contour dynamics algorithm is used while for the systems considered in chapters 2.2 and 2.3, a cylindrical (or singly periodic) contour dynamics algorithm is used to account for the periodicity of the vortical interface. First, computations of equilibria for the periodic configuration of chapter 2.2 are presented. Equilibria are first computed for the case when the point vortices are situated in the non-rotational region of the flow and also for when they are situated in the rotational region. Next, equilibria are computed for the anti-symmetric periodic configuration of chapter 2.3. Finally, as noted in chapter 2, no non-linear equilibria for the planar anti-symmetric configuration of chapter 2.1 could be found and this is briefly discussed.

## 3.1 Periodic symmetric equilibria

In computing periodic equilibria a modified version of the cylindrical contour dynamics algorithm outlined in Dritschel (1989) is used. The vorticity dynamics are formulated on the surface of an infinitely long, unit radius cylinder (which corresponds to the case when $L = 2\pi$ in chapters 2.2 and 2.3). In the algorithm, velocity fields owing to piecewise constant vorticity jumps are determined using three dimensional Cartesian coordinates restricted to the surface of the cylinder. From these Cartesian coordinates the corresponding surface cylindrical coordinates $\hat{\phi}$ and $\hat{z}$, where $\hat{\phi} \in [0, 2\pi)$ is the azimuthal angle and $\hat{z} \in (-\infty, \infty)$ is the along cylinder axis coordinate, are determined. Note that here, the radial coordinate, $\hat{r}$, is always given by $\hat{r} = 1$.

Further details of the cylindrical contour dynamics algorithm are given in appendix A and Dritschel (1989). The cylindrical coordinates $\hat{\phi}$ and $\hat{z}$ correspond to the planar Cartesian coordinates $x$ and $y$ respectively and these latter coordinates are used in the discussion that follows.

The vortical interface is discretized into $2N - 2$ nodes which are uniformly distributed in the $x$-direction such that $x_1 = 0$ and $x_N = \pi$. The interface must be symmetric over one period (where one period is taken to be the interval $x \in [0, 2\pi)$). To ensure this property the computational domain is restricted to the interval between 0 and $\pi$, i.e. only the $y$-location of the nodes $i = 1, .., N$ are adjusted during the iterative process. The $y$ coordinates of nodes with $i > N$ (i.e. the nodes within the interval $0 < x < 2\pi$) are thus given by $y_{N+j} = y_{N-j}$. A schematic of the setup is shown in figure 3.1. For a given interfacial shape, the velocity at the interface is computed by summing its self induced velocity, calculated using the contour dynamics algorithm, and the velocity at the interface owing to the point vortex located at $(\pi, y_{loc})$ (where $y_{loc}$ will be set to $-1$ or $-2$). The $x$-direction velocity at $u_{vort}$ the point vortex, which is entirely due to the interfacial disturbance, is also computed using the contour dynamics algorithm. Also, note that due to the symmetry of the interface the requirement that the $y$-direction velocity at the point vortex is zero is automatically satisfied. Here, the contour dynamics algorithm is not being used in its normal time dependent form (Dritschel 1989), but rather is used only to find the velocity at each node upon the interface and at the point vortex.

Two values of the streamfunction, $\psi_i^F$ and $\psi_i^B$, are calculated at each node in the computational domain by marching to the right and to the left respectively. When
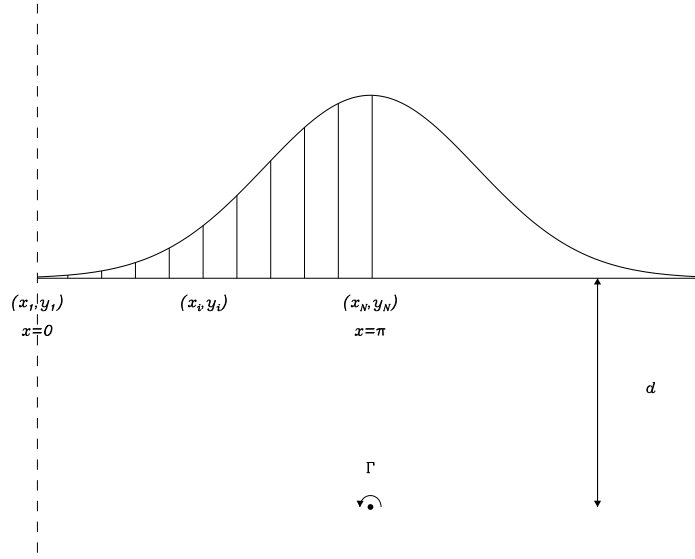
Figure 3.1: Schematic of the computational domain setup for periodic symmetric equilibria.

marching to the right the streamfunction at the $i = 1$ node is set so that $\psi_1^F = 0$. When marching to the left the streamfunction at $i = N$ is set to zero, that is $\psi_N^B = 0$. Values of the streamfunction at each node are calculated according to

$$\psi_{i+1}^F = \psi_i^F + \bar{v}_i dx_i - \bar{u}_i dy_i, \qquad i = 1, .., N-1, \tag{3.1}$$

and

$$\psi_i^B = \psi_{i+1}^B - \bar{v}_i dx_i + \bar{u}_i dy_i, \qquad i = 1, .., N-1, \tag{3.2}$$

where

$$\bar{u}_i = \frac{u_i + u_{i+1}}{2}, \qquad \bar{v}_i = \frac{v_i + v_{i+1}}{2}, \qquad i = 1, .., N-1, \tag{3.3}$$

and

$$dx_i = x_{i+1} - x_i, \qquad dy_i = y_{i+1} - y_i, \qquad i = 1, .., N-1. \tag{3.4}$$

The streamfunction at each node is then the average of $\psi^F$ and $\psi^B$, i.e.

$$\psi_i = \frac{\psi_i^F + \psi_i^B}{2}. \tag{3.5}$$

To find an equilibrium the values of $y_i$ and $U$ are simultaneously adjusted so that, to within some numerical tolerance, $\psi_i = 0$, $i = 1, .., N$, and the $x$-direction velocity at the vortex, $u_{vort} = 0$. By fixing the point vortex circulation, $\Gamma$, and the distance of the vortex from the interface, the $N + 1$ unknowns $y_1, .., y_N$ and $U$ are given by the $N + 1$ equations

$$\psi_i(y_1, y_2, .., y_N, U) = 0, \qquad i = 1, .., N,$$

$$\tag{3.6}$$

$$u_{vort}(y_1, y_2, .., y_N, U) = 0.$$

Equations (3.6) are solved using Newton's method. For a given iteration, the $n$th iteration say, the variables $y_j$ and $U$ at the $(n+1)$th iteration are computed according to

$$y_j^{(n+1)} = y_j^{(n)} + \Delta_j, \qquad j = 1, .., N$$

$$\tag{3.7}$$

$$U^{(n+1)} = U^{(n)} + \Delta_{N+1},$$

where $\Delta_j$ is the $j$th element of the vector solution of the $(N + 1) \times (N + 1)$ matrix equation

$$\sum_{j=1}^{N} \frac{\partial \psi_i^{(n)}}{\partial y_j} \Delta_j + \frac{\partial \psi_i^{(n)}}{\partial U} \Delta_{N+1} = -\psi_i^{(n)}, \qquad i = 1, .., N,$$

$$\tag{3.8}$$

$$\sum_{j=1}^{N} \frac{\partial u_{vort}^{(n)}}{\partial y_j} \Delta_j + \frac{\partial u_{vort}^{(n)}}{\partial U} \Delta_{N+1} = -u_{vort}^{(n)}.$$

The derivatives in (3.8) are computed numerically according to

$$\frac{\partial f}{\partial l} \approx \frac{f(l+\delta) - f(l)}{\delta}, \tag{3.9}$$

using $\delta = 10^{-6}$. Therefore, in order to calculate the columns of the matrix, for a configuration $y_j$, $U$ $(j = 1, .., N)$, the contour dynamics algorithm is called to evaluate the velocity at each node along with $u_{vort}$. Knowing the velocity at each node enables the streamfunction to be calculated using (3.5). The values $y_j$ at each node (or the value of $U$ when evaluating elements of the $(N+1)$th row) are then varied by $\delta$ and the contour dynamics algorithm is called to evaluate the new velocities, enabling the evaluation of the new streamfunctions $\psi_i(y_j + \delta)$ $(i = 1, .., N)$ and $u_{vort}(y_j + \delta)$ (or $\psi_i(U + \delta)$ and $u_{vort}(U + \delta)$ when $j = N + 1$). Using the estimate of the derivative given in (3.9) the columns of the matrix are hence evaluated. Finally, the matrix equation (3.8) is solved by Gaussian elimination. Therefore, each iteration of the above algorithm requires $N + 2$ calculations of the velocity field at all points, giving a contour dynamics cost of $(N+2) \times (N+1)$. In addition, an $(N+1) \times (N+1)$ matrix is inverted once per iteration.

In the following computations, the number of nodes in the computational domain is set to $N = 100$, giving a resolution in the $x$-direction of $\delta x = 0.0314$. Increasing the number of nodes within the computational domain (i.e. decreasing $\delta x$) results in the algorithm converging to a slightly different steady state which, although different, is nevertheless, a genuine equilibria. This is due to the fact that all nodes within the computational domain are free to move in the $y$-direction and is not due to a lack of resolution in the $x$-direction to obtain convergence. As all nodes are free to move in the $y$-direction, it is possible for the entire interface to shift 'upwards' or 'downwards'

through the course of a simulation. This is equivalent to, say, altering the periodicity of the domain in chapter 2.2 which, in the linear regime, can introduce a number of possible new equilibrium shapes. Thus for a point vortex of fixed circulation at some fixed distance below the $y$-axis it is expected that the algorithm will converge to many distinct equilibria depending on the initial conditions used, i.e. depending on the initial choice of interface shape and free stream velocity $U$. This is typical of Newtonian iteration.

In order to monitor the convergence of the computed equilibria, values of both $U$ and the area of the interfacial disturbance are recorded and it is ensured that these values have converged to at least six decimal places in all results that follow. This level of convergence was generally realised within 50 iterations.

The lack of exact solutions for the non-linear equilibria inhibits an analytical investigation of their stability. Thus, to examine the stability, or robustness of computed equilibria, they are then used as initial conditions in a fully non-linear time dependent cylindrical contour dynamics code. A robust equilibrium is expected to remain largely unchanged for a reasonable period of time. Conversely, if an equilibrium is unstable, due to numerical perturbations it is expected to quickly lose coherence and behave in a complicated manner. Some of the equilibria are tested in this way.

### 3.1.1   Point vortex in the irrotational flow region

Consider the configuration where the vortex is in the irrotational region of the flow (chapter 2.2.1, figure 2.5). The linear equilibria computed in chapter 2.2.1 are used to initialise the non-linear algorithm described above. For the case in chapter

2.2.1 when $L = \pi$, this equates to multiplying all length scales by a factor of two and consequently the point vortex circulation by a factor of four and $U$ by a factor of two. Figure 3.2 shows the non-linear equilibria computed with $(\Gamma = 0.4, U_0 = 0.034)$, $(\Gamma = 1.0, U_0 = 0.084)$ and $(\Gamma = 2.0, U_0 = 0.168)$ as initial conditions (where the brackets have been introduced for ease of notation and indicate the pair of initial values used in each case and $U_0$ represents the value of $U$ used to initialise the simulation. Note that here, $\Gamma$ remains fixed). These initial conditions correspond to three of the linear equilibria shown in figure 2.9 'stretched' into a domain with $2\pi$ periodicity. When $\Gamma = 0.4$ and $\Gamma = 1$, through visual comparison, it is seen that the shapes of $\eta(x)$ correspond very closely to their linear counterparts of figure 2.9 (i.e. the equilibria with $(\Gamma = 0.1, U = 0.017)$ and $(\Gamma = 0.25, U = 0.042)$ respectively). However, when $\Gamma = 2$, the higher order modes present in the linear equilibria are clearly absent in the 'corresponding' non-linear case; the shape of the interface is very similar to when $\Gamma = 0.4$ or $\Gamma = 1$ but with a higher amplitude. This is not unexpected as, as mentioned above, all interfacial nodes are free to move in the $y$-direction making the algorithm more likely to converge to a more stable equilibrium without higher order modes. Therefore, if non-linear equilibria in which higher order modes play a significant role do exist, it is likely that a different algorithm is needed to find them. Consequently, the constraints seen on the values of $\Gamma$ that give physically permissible $U$ (i.e. 2.60 and 2.61) in the linear analysis are not observed here. Also, the equilibria of chapter 2.2.1 with large amplitude interface oscillations, such as in figures 2.10 and 2.12, could not be realised numerically. In fact, the equilibria of figure 2.12 resemble closely some of the non-linear equilibria computed when the point vortex is in the

rotational region of the flow as will be seen in the following section.

When initialising the algorithm with the linear equilibria of chapter 2.2.1 with $L = 2\pi$ no corresponding non-linear equilibria could be found. In all cases the algorithm would either diverge or converge to a result in which a great deal of noise was present at the edges of the vortical interface. Equilibria could however be found when the algorithm was initialised with the point vortex unit distance from a flat interface. However, in such cases the interface would essentially move away from the vortex to an equilibrium position in which the vertical separation of vortex and interface was far greater than the initial unit distance. This resulted in equilibria similar to those shown of figure 3.3 (whose computation is detailed below).

Figure 3.3 shows equilibria resulting from initialising the simulation with the vortex at $(\pi, -2)$ and a flat interface along $y = 0$ with $(\Gamma = 4, U_0 = 0.3)$, $(\Gamma = 12, U_0 = 0.5)$ and $(\Gamma = 20, U_0 = 0.6)$. In the three equilibria of figure 3.3 it is seen that the node at $x = 0$ is at a location with $y < 0$. This was a common feature of equilibria resulting from initialising the simulation with the vortex at $(\pi, -2)$ for various initial interface shapes. Another example of an initial interface shape used was a Gaussian profile. Also, as noted previously, in simulations initiated with the vortex located at $(\pi, -1)$ and a flat interface along $y = 0$, the whole interface would often 'lift up' resulting in a vortex-interface separation similar to the separations seen in figure 3.3. This seemingly preferential vortex-interface separation possibly gives some indication of an optimum vortex-interface separation for stability. It should also be noted that initialising simulations with a vortex of the same circulation but with different values of $U_0$ could lead to the algorithm converging to different equilibria. These equilibria

would be similar in shape but with different $y$ values at the nodes; that is, the initial

value of $U_0$ would effect the resulting vortex-interface separation.
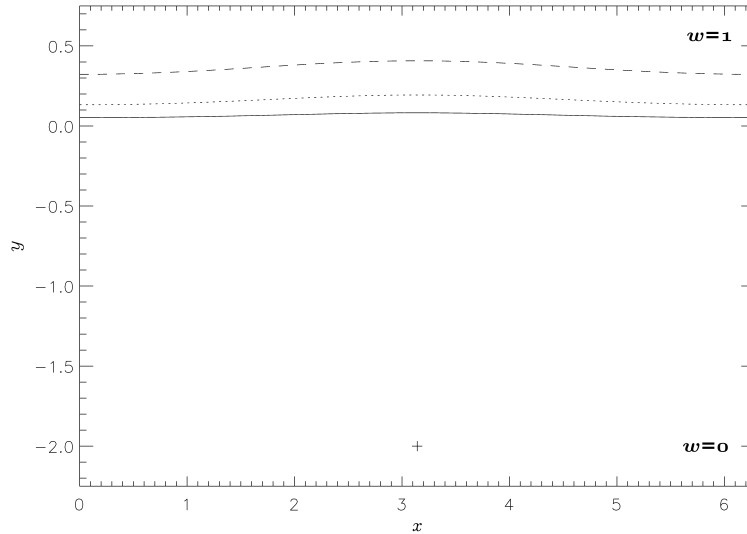


Figure 3.2: Non-linear profiles of $\eta(x)$ computed with $\Gamma = 0.4$ (solid line), $\Gamma = 1$ (dotted line) and $\Gamma = 2$ (dashed line). The final computed free stream velocities are, respectively, $U = 0.02545$, $U = 0.06137$ and $U = 0.13412$. The $+$ indicates the point vortex position.

To examine the robustness of the computed equilibria they are set as initial conditions in a time dependent cylindrical contour dynamics code. In the contour dynamics algorithm velocity fields are calculated at nodes along the interface as well as at the point vortex. Time integration is carried out using a fourth order Runge-Kutta method and typically 200-400 nodes are used to represent the vortical interface depending on the size of the equilibrium. The time step is set to $dt = 0.01$. Figures 3.4 and 3.5 show the time evolution of the equilibrium previously shown in figure 3.2 with ($\Gamma = 0.4, U = 0.02545$) and the equilibrium shown in figure 3.3 with ($\Gamma = 12, U = 0.040912$) respectively. Even after the 150 time units, the equilibrium
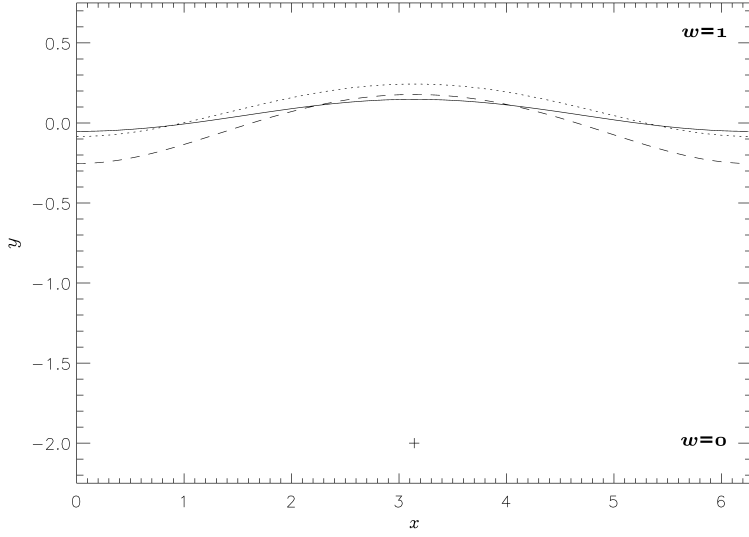
Figure 3.3: Non-linear profiles of $\eta(x)$ computed with $\Gamma = 4$ (solid line), $\Gamma = 12$ (dotted line) and $\Gamma = 20$ (dashed line). The final computed free stream velocities are, respectively, $U = 0.02357$, $U = 0.04091$ and $U = 0.00310$. The $+$ indicates the point vortex position.

with $(\Gamma = 0.4, U = 0.02545)$ has moved very little and the little movement which has occurred is effectively discernible to the naked eye. To give an indication of how little the numerical equilibrium has moved in this time, at $t = 150$ the deviation of the point vortex in the $x$-direction is of $O(10^{-4})$, showing that the equilibrium is very robust. At $t = 150$, the vortex with $(\Gamma = 12, U = 0.040912)$ has clearly deviated from its initial position at $t = 0$. A faster deviation away from the equilibrium position is expected in this case due to the larger vortex circulation and interface amplitude involved. Nevertheless, the equilibria still takes a significant time to deviate from its initial position and even after large time periods there is only a relatively small deviation. Similar results to those shown in figures 3.2 and 3.3 were seen for many of the other numerical equilibria computed giving a good indication that many of the

equilibria computed when the point vortex is in the irrotational region of the flow are of a stable nature.
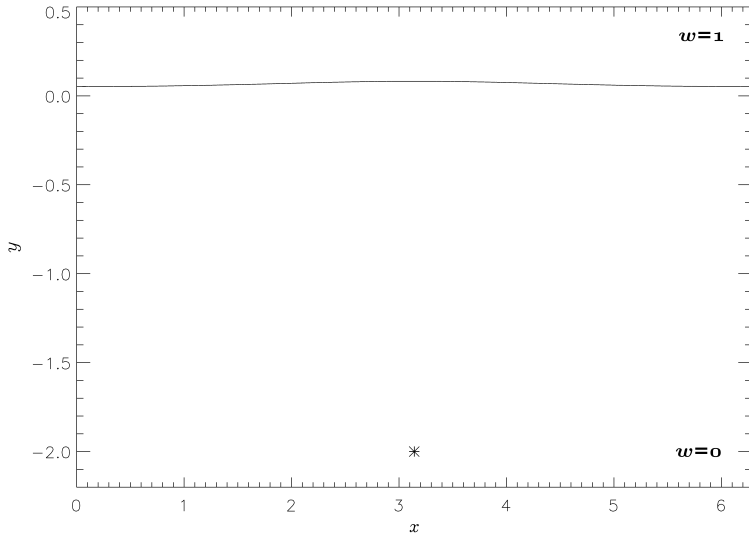


Figure 3.4: Numerical equilibrium with ($\Gamma = 0.4, U = 0.02545$) at $t = 0$ (dashed line and asterisk) and at $t = 150$ (solid line and cross). (Over this time period both the interface and point vortex have moved very little making any differences very difficult to resolve by eye).

It is also of interest to consider how the magnitude of the vortex circulation effects the size of the disturbance at the interface. One method of examining this is to consider how the amplitude of the disturbance varies with vortex circulation, where amplitude is taken here to mean the difference in $y$ between the highest and lowest nodes of the computational domain. Figure 3.6 shows the amplitude of the disturbance at the interface for point vortices of various circulations. In obtaining the results of figure 3.6, all simulations were initiated with the point vortex at a vertical distance of two from a flat interface, and $U$ was varied between 0.1 to 0.2, with larger values of $U$ being used for larger vortex circulations. After the algorithm
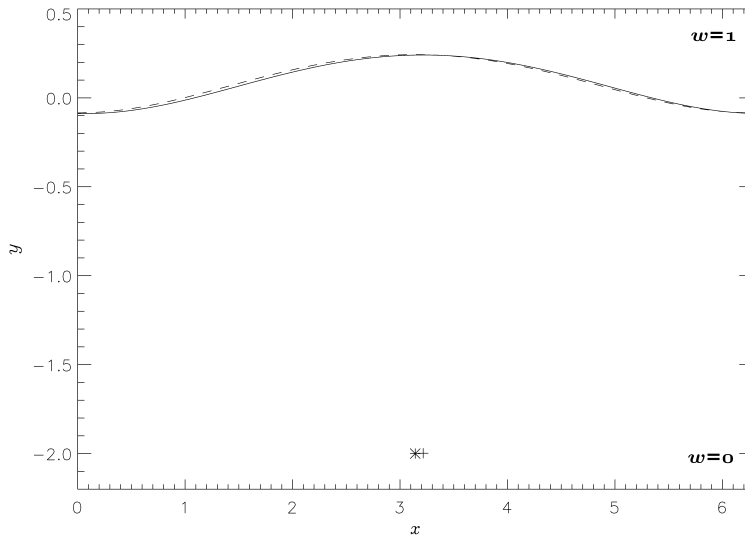
Figure 3.5: Numerical equilibrium with ($\Gamma = 12, U = 0.040912$) at $t = 0$ (dashed line and asterisk) and at $t = 150$ (solid line and cross).

has converged, the final vortex-interface separation will play an important role in the amplitude of the disturbance on the interface, and as the algorithm was chosen such that all interfacial nodes are free to move in the vertical direction, this separation is very difficult to control. Through trial and error, the above initial conditions were found to keep the separation of the vortex from the lowest node in the computational domain relatively constant. Therefore, although this is a rather crude analysis, it does give some indication of how the vortex circulation effects the disturbance on the interface.

Figure 3.6 indicates that for weak point vortices, increasing the circulation results in the amplitude of the disturbance increasing quite rapidly in an approximately linear manner. As the vortex circulation gets larger the amplitude of the disturbance continues to increase, however this increase in amplitude becomes 'sub-linear' as in-

dicated by the decreasing gradient in figure 3.6. That is, increasing the point vortex
circulation results in the interface amplitude increasing with 'diminishing returns'.
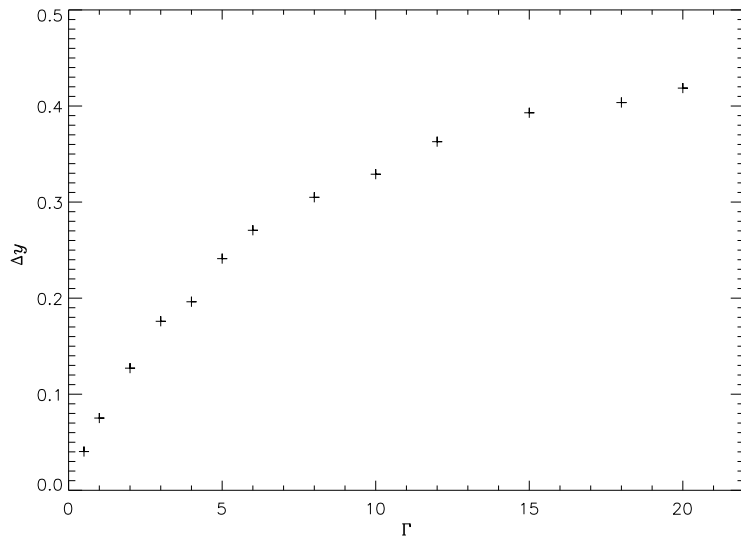


Figure 3.6: The difference in height between the highest and lowest interface nodes
of the equilibria ($\Delta y$) for point vortices of various circulations. All simulations were
initiated with point vortices at a $y$-distance of two from a flat interface and $U$ varying
from 0.1 to 0.2.

To summarise, in this section, various non-linear equilibria have been computed
for the configuration where a point vortex in a singly-periodic domain is located in
the irrotational region of a shear flow. Non-linear equilibria were initially computed
by initialising simulations with the linear equilibria calculated in chapter 2.2.1. For
small vortex circulations, when the vortex-interface vertical separation was two units,
the non-linear equilibria show good agreement with the linear equilibria. However, as
the vortex circulation is increased, the non-linear equilibria resembled scaled versions
of those equilibria with point vortices of smaller circulation. When linear equilibria
with a vortex-interface separation of one unit were used to initialise the algorithm, no

corresponding non-linear equilibria could be found i.e. convergence was not obtained.

A range of non-linear equilibria were found through initialising the algorithm with point vortices of various circulations at a vertical distance of two units from a flat interface. The robustness of these equilibria, along with those found through initialising the algorithm with corresponding linear equilibria, was tested. It was seen that the computed equilibria remained largely unchanged for large time periods giving a good indication that they are of a stable nature.

### 3.1.2 Point vortex in the rotational flow region

The configuration where the vortex is in the rotational region of the flow is now considered (see chapter 2.2.2, equation 2.62). The linear equilibria of figures 2.17 and 2.18 are used as initial conditions in the computation of non-linear equilibria. As mentioned at the beginning of section 3.1.1, for the configuration of chapter 2.2.2 with a periodicity of $\pi$, it is required to multiply all length scales by a factor of two and consequently the vortex circulation by a factor of four and $U_0$ by a factor of two to 'stretch' these equilibria onto the surface of the unit cylinder, which is a $2\pi$-periodic domain.

Figure 3.7 shows the non-linear equilibria resulting from using the appropriately adapted equilibria of figure 2.17 as initial conditions, that is, computation of non-linear equilibria is initiated with $(\Gamma = 0.4, U_0 = 2.032)$, $(\Gamma = 2, U_0 = 2.158)$, $(\Gamma = 4, U_0 = 2.316)$, $(\Gamma = 8, U_0 = 2.632)$ and $(\Gamma = 12, U_0 = 2.948)$ respectively. These initial conditions lead to equilibria in which the interface is nearly flat. Through a visual comparison with the linear equilibria of figure 2.17, it is seen that the cor-

responding non-linear equilibria have a 'slightly' flatter interface and an increased vortex-interface separation. Slightly surprisingly, in all cases, the resulting value of $U$ changes very little, if at all.

In figure 3.8, the equilibria resulting from using the linear equilibria of figure 2.18 as initial conditions are shown. Through a visual comparison with figure 2.18, the non-linear equilibria computed are very similar in shape to their corresponding linear equilibria and their values of $U$ match up to five significant figures. When $\Gamma = 0.1$, $\Gamma = 0.5$ or $\Gamma = 1$, it is difficult to distinguish the non-linear from linear equilibria with the naked eye. When $\Gamma = 2.0$ or $\Gamma = 3.0$, the amplitude of the disturbance at the interface is smaller for the non-linear equilibria, that is, the vertical distance between the highest and lowest interfacial nodes has decreased. For $\Gamma = 2.0$, the amplitude decreases from 0.38790 (linear equilibrium) to 0.30305 (non-linear equilibrium) and for $\Gamma = 3.0$, the decrease in amplitude is from 0.52668 to 0.35594.

As in the previous section, to examine the robustness of computed non-linear equilibria they are used as initial conditions in a time dependent cylindrical contour dynamics code. Figures 3.9 and 3.10 show the time evolution of the equilibria of figure 3.8 with ($\Gamma = 0.1, U = 1.00600$) and ($\Gamma = 3.0, U = 1.18900$) respectively. As expected, equilibria with only small disturbances upon the interface remain largely unchanged over very long time periods. For larger amplitude equilibria, there is a drift in the interface from its initial configuration. However, this drift only occurs after a reasonable time, about 50 time units in the case of figure 3.10, giving a good indication that the computed equilibria are stable configurations.

For an initial vortex-interface separation of two units, more 'interesting' equilibria
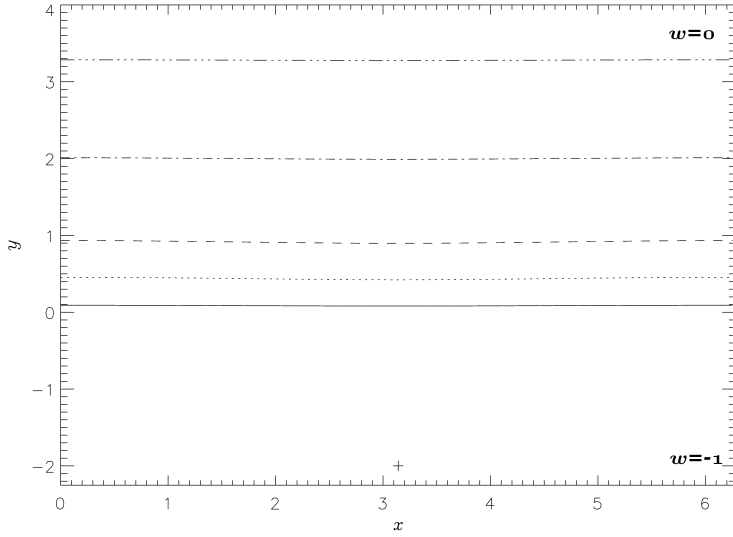
Figure 3.7: Non-linear profiles of $\eta(x)$ computed with $\Gamma = 0.4$ (solid line), $\Gamma = 2$ (dotted line), $\Gamma = 4$ (dashed line), $\Gamma = 8$ (dot-dash line) and $\Gamma = 12$ (three dot-dash line) for a point vortex at $z = -2$. The final computed free stream velocities are, respectively, $U = 2.03200$, $U = 2.15800$, $U = 2.31600$, $U = 2.63200$ and $U = 2.94798$. The + indicates the point vortex position.

than those of figure 3.7 can be computed by initialising the algorithm with differ-ent initial conditions, for example, a flat interface or a cosine profile. Figure 3.11 shows some of the interface shapes resulting from initialising the algorithm with a flat interface for point vortices with circulations ranging from 0.5 to 12 and $U$ ranging from 2.032 to 2.12. These conditions were chosen through trial and error in order to obtain equilibria whose minimums had roughly the same $y$ value. It was seen that for this configuration, the minimum interface height of computed equilibria could be 'controlled' by the initial choice of $U$. The larger the value of $U$, the higher and flatter the resulting equilibria. In figure 3.12 a plot of the interface amplitude against point vortex circulation is shown for the equilibria of figure 3.11 along with some extra
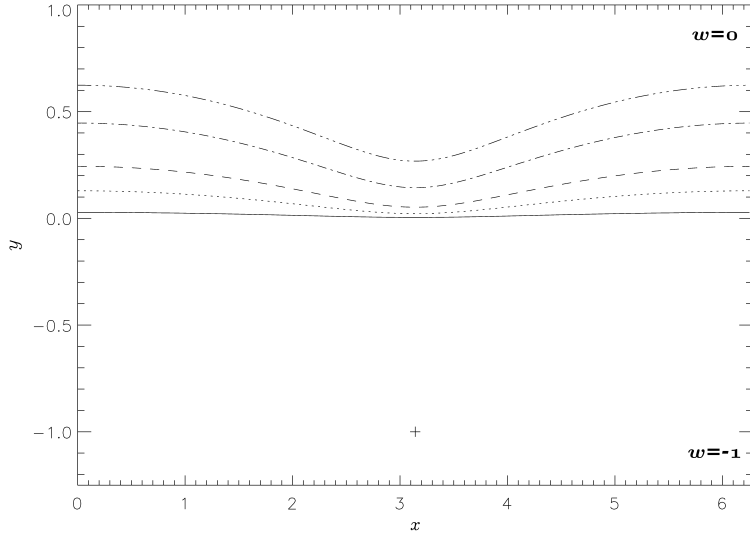
Figure 3.8: Non-linear profiles of $\eta(x)$ computed when $\Gamma = 0.1$ (solid line), $\Gamma = 0.5$ (dotted line), $\Gamma = 1$ (dashed line), $\Gamma = 2$ (dot-dash line) and $\Gamma = 3$ (three dot-dash line) for a point vortex at $z = -1$. The final computed free stream velocities are, respectively, $U = 1.00600$, $U = 1.02900$, $U = 1.05900$, $U = 1.12300$ and $U = 1.18900$. The $+$ indicates the point vortex position.

equilibria computed using point vortices of different circulations. It was ensured that the interface minimum in these added equilibria was at a very similar level to those of figure 3.11. Here, in contrast to the previous section, as the point vortex circulation increases the amplitude of the interface increases at a faster rate.

## 3.2   Periodic anti-symmetric equilibria

Non-linear equilibria are now calculated for the case of a vortex street in a shear flow (see chapter 2.3 for details of the configuration). The algorithm used to compute these equilibria is similar to that detailed in 3.1, the required modifications are detailed below.
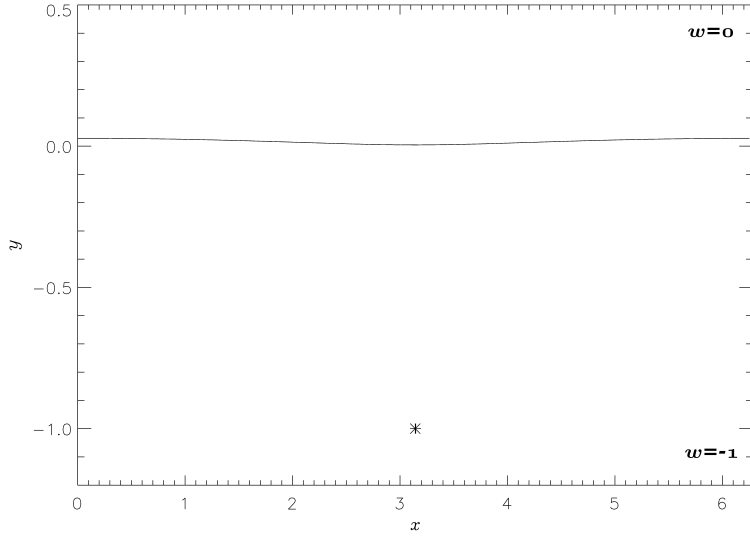
Figure 3.9: Numerical equilibrium of figure 3.8 with $(\Gamma = 0.1, U = 1.00600)$ at $t = 0$ (solid line and asterisk) and at $t = 150$ (dashed line and $+$). (Over this time period both the interface and point vortex have moved very little making any differences very difficult to resolve by eye).

Again, the domain is discretized into $2N - 2$ nodes uniformly spaced in the $x$-direction. The equilibria under consideration must now be anti-symmetric over one period. To ensure this property, the computational domain is again restricted to the interval between $0$ and $\pi$ and only the nodes $i = 1, .., N$ are considered. Then for $i > N$ the $y$ node locations are calculated according to $y_{N+j} = -y_{N-j}$. For a given interfacial shape, the velocity at each node is computed by summing its self induced velocity, calculated using the contour dynamics algorithm, with the velocity at the interface owing to the point vortices located at $(\pi - S/2, y_{loc})$ and $(\pi + S/2, -y_{loc})$ where $S$ is the horizontal separation of the vortices and $y_{loc}$ will again to set to $-1$ or $-2$. Ensuring the vortex at $(\pi - S/2, -1)$ is stationary is sufficient to ensure its anti-symmetrically placed partner is also stationary. Thus only the velocity at
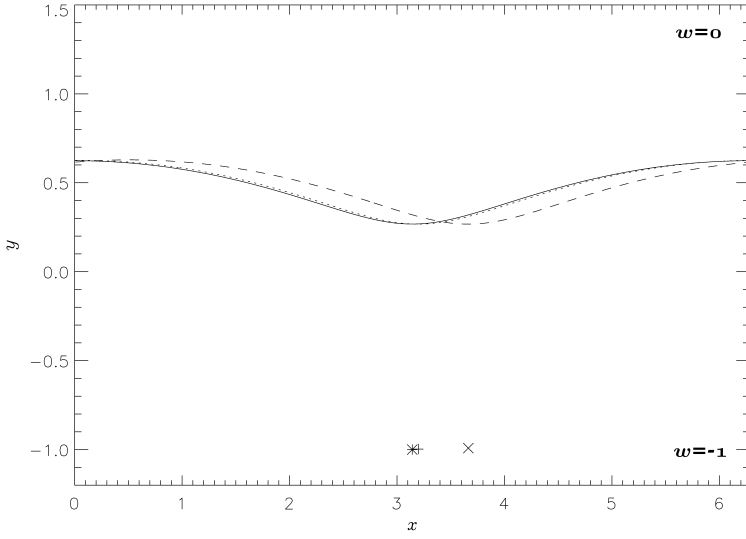
Figure 3.10: Time evolution of the equilibrium of figure 3.8 with ($\Gamma = 3.0, U = 1.18900$). The solid line and asterisk mark $t = 0$, the dotted line and + mark $t = 50$ and the dashed line and X mark $t = 150$.

$(\pi - S/2, -1)$ is considered and is evaluated in both the $x$ and $y$ directions by summing the velocity field owing to the interface with that due to the other point vortex.

In contrast to the configurations considered in 3.1, in which it was not natural to fix any nodes in the computational domain, with the anti-symmetric configuration under consideration it is natural to fix $y_1 = y_N = 0$. The streamfunction, $\psi_i$, is now evaluated by setting $\psi_1 = 0$ and then marching to the right such that

$$\psi_{i+1} = \psi_i + \bar{v}_i dx_i - \bar{u}_i dy_i, \qquad i = 1, .., N - 1, \tag{3.10}$$

where $\bar{u}_i$ and $\bar{v}_i$ and $dx_i$ and $dy_i$ are given by equations (3.3) and (3.4) respectively. To find an equilibrium, the $N + 1$ unknowns $y_i$ ($i = 2, .., N - 1$), $U$, $\Gamma$ and $S$ are simultaneously adjusted such that the interface is iterated towards a streamline and the velocity at the point vortices vanishes, that is, $(u_{vort}, v_{vort}) = (0, 0)$. The vertical
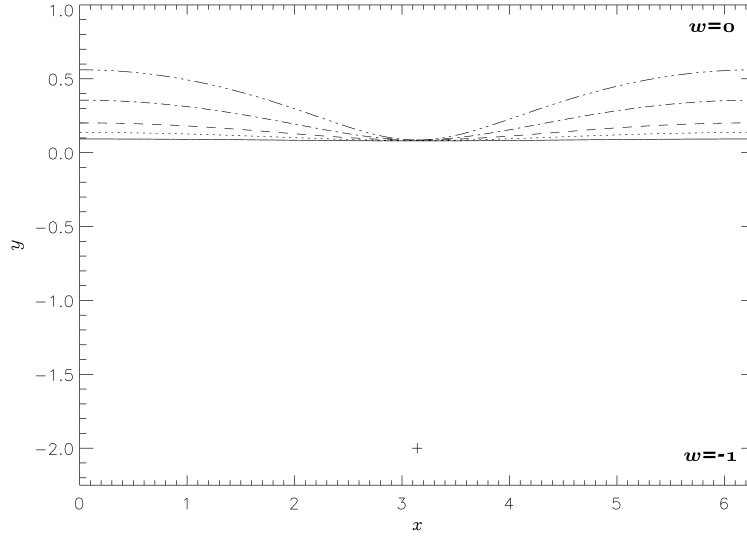
Figure 3.11: Non-linear profiles of $\eta(x)$ with $(\Gamma = 0.1, U = 2.03200)$ (solid line), $(\Gamma = 2, U = 2.04000)$ (dotted line), $(\Gamma = 4, U = 2.05200)$ (dashed line), $(\Gamma = 8, U = 2.08000)$ (dot-dash line) and $(\Gamma = 12, U = 2.12000)$ (three dot-dash line) for a point vortex at $(\pi, -2)$. In all cases the final value of $U$ is unchanged to five decimal places.

separation of the vortices from the interface is fixed giving $N + 1$ equations,

$$\psi_i(y_2, y_3, .., y_{N-1}, U, \Gamma, S) = 0, \qquad i = 2, .., N,$$

$$u_{vort}(y_2, y_3, .., y_{N-1}, U, \Gamma, S) = 0, \tag{3.11}$$

$$v_{vort}(y_2, y_3, .., y_{N-1}, U, \Gamma, S) = 0.$$

Note that here, the vortices have not been fixed such that their horizontal separation is $\pi$ (as was the case in the linear analysis of chapter 2.3) in order to form a system of $(N+1)$ unknowns and $(N+1)$ variables. But as will be seen in the results that follow, the horizontal vortex separation naturally converges (to a good level of agreement) to $S = \pi$. Equations 3.11 are again solved using Newton's method such that the
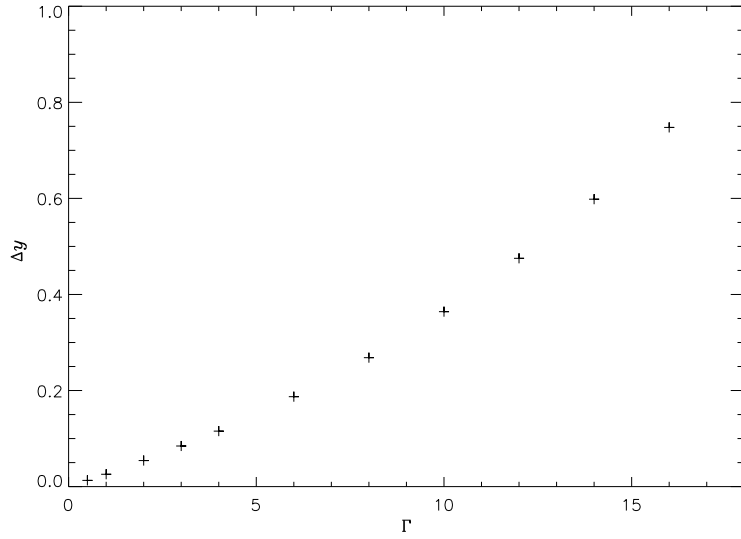
Figure 3.12: The difference in height between the highest and lowest interface nodes of the equilibria ($\Delta y$) for point vortices of various circulations. All simulations were initiated with point vortices at a $y$-distance of two from a flat interface and $U$ varying from 2.032 to 2.18.

$(n+1)$th iteration is evaluated according to

$$y_{j+1}^{(n+1)} = y_{j+1}^{(n)} + \Delta_j, \qquad j = 1, .., N-2$$

$$U^{(n+1)} = U^{(n)} + \Delta_{N-1},$$

$$(3.12)$$

$$\Gamma^{(n+1)} = \Gamma^{(n)} + \Delta_N,$$

$$S^{(n+1)} = S^{(n)} + \Delta_{N+1},$$

where $\Delta_j$ is the $j$th element of the vector solution of the $(N+1) \times (N+1)$ matrix

equation

$$\sum_{j=1}^{N-2} \frac{\partial \psi_{i+1}^{(n)}}{\partial y_{j+1}} \Delta_j + \frac{\partial \psi_{i+1}^{(n)}}{\partial U} \Delta_{N-1} + \frac{\partial \psi_{i+1}^{(n)}}{\partial \Gamma} \Delta_N + \frac{\partial \psi_{i+1}^{(n)}}{\partial \Gamma} \Delta_S = -\psi_{i+1}^{(n)}, \qquad i = 1, .., N-1,$$

$$\sum_{j=1}^{N-2} \frac{\partial u_{vort}^{(n)}}{\partial y_{j+1}} \Delta_j + \frac{\partial u_{vort}^{(n)}}{\partial U} \Delta_{N-1} \frac{\partial u_{vort}^{(n)}}{\partial \Gamma} \Delta_N \frac{\partial u_{vort}^{(n)}}{\partial S} \Delta_{N+1} = -u_{vort}^{(n)},$$

$$\sum_{j=1}^{N-2} \frac{\partial v_{vort}^{(n)}}{\partial y_{j+1}} \Delta_j + \frac{\partial v_{vort}^{(n)}}{\partial U} \Delta_{N-1} \frac{\partial v_{vort}^{(n)}}{\partial \Gamma} \Delta_N \frac{\partial v_{vort}^{(n)}}{\partial S} \Delta_{N+1} = -u_{vort}^{(n)}.$$

$$(3.13)$$

The derivatives in (3.13) are again computed numerically according to (3.9). The number of nodes in the computational domain is now set to $N = 150$, giving a resolution in the $x$-direction of $\delta x = 0.02094$. Increasing the number of nodes within the computation does not alter the results to the quoted level of accuracy. Typically, convergence was realised within 50 iterations.

In figure 3.13 the non-linear equilibria resulting from initialising the algorithm with the linear equilibria of chapter 2.3, figures 2.20 and 2.21 are shown. These linear equilibria were derived in a $\pi$-periodic domain and have thus once again been 'stretched' onto the unit cylinder. The initial conditions used in computing these equilibria were given by ($\Gamma_0 = -16, U_0 = -0.288, S_0 = \pi$), ($\Gamma_0 = -8, U_0 = 0.280, S_0 = \pi$), ($\Gamma_0 = -2, U_0 = 0.862, S_0 = \pi$), ($\Gamma_0 = -1, U_0 = 0.930, S_0 = \pi$) and ($\Gamma_0 = 2, U_0 = 1.144, S_0 = \pi$), where the circulation given is that of the vortex in the region $x \in [0, 2\pi)$ and the 0 subscript indicates the initial value of the parameter in question. In all computations the vortex circulation remained unchanged to 5 decimal places, as

did the horizontal vortex separation parameter $S$. (It should be noted that increasing the $x$-direction resolution resulted in $\Gamma$ and $S$ remaining unchanged to five decimal places. In the following text, for the sake of brevity, the given value of $\Gamma$ will be accurate to five decimal places, i.e. $\Gamma = 1$ means $\Gamma = 1.00000$).

For the vortices with $\Gamma = -16$ and $\Gamma = -8$ the interface was initially curved towards them (see figure 2.22). However, in the non-linear equilibria resulting from these initial configurations, the interface has 'reversed' and is now curved away from the point vortices (figure 3.13). The non-linear equilibria with $\Gamma = -2$ and $\Gamma = -1$ are similar in shape but have a lower amplitude in comparison to their linear counterparts of figure 2.21. The non-linear equilibria for $\Gamma = -16$ and $\Gamma = -8$ are thus similar in shape to the equilibria with $\Gamma = -2$ and $\Gamma = -1$ but have larger amplitudes owing to the larger circulations of the point vortices involved. Conversely, when $\Gamma = 2$, the resulting non-linear equilibria is of a similar shape but has a greater amplitude than its linear counterpart, compare figures 2.21 (linear equilibria) and 3.13 (non-linear equilibria).

Figure 3.14 shows the non-linear equilibria resulting from initialising the algorithm with the linear equilibria of figure 2.25, thus, the initial conditions are given by $(\Gamma_0 = -1, U_0 = 0.620, S_0 = \pi)$ and $(\Gamma_0 = -0.1, U_0 = 0.544, S_0 = \pi)$. In both cases, the vortex circulation and separation parameter $S$ again remain unchanged to 5 decimal places and the final free stream velocities are slightly lower than their initialisation values. Through a visual comparison with the initial interface shapes shown in figure 2.25 it is seen that the non-linear shapes are very similar. It is worth noting that when the algorithm was initialised with the linear equilibria of figure 2.24,
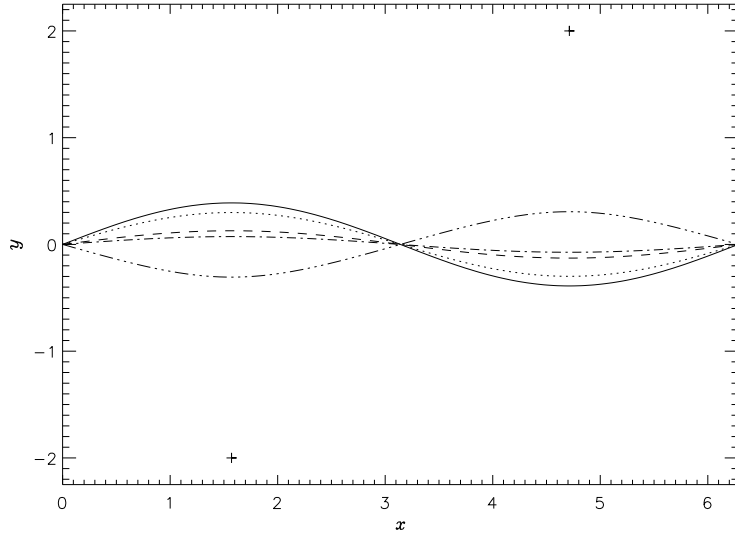
Figure 3.13: Non-linear profiles of $\eta(x)$ with ($\Gamma = -16.00000, U = -0.20640$) (solid line), ($\Gamma = -8.00000, U = 0.40290$) (dotted line), ($\Gamma = -2.00000, U = 0.85410$) (dashed line), ($\Gamma = -1.00000, U = 0.92770$) (dot-dash line) and ($\Gamma = 2.00000, U = 1.13250$) (three dot-dash line). $S = 3.14159$ in all cases and the + symbols mark the locations of the point vortices.

which had the same vortex circulations as the above equilibria but different free stream velocities and an interface that initially curved towards the point vortices, provided it was run for a sufficient period of time it would converge to exactly the equilibria of figure 3.14. The algorithm was also initiated with positive circulation point vortices and for various initial interface shapes. However, for the initial conditions tried with vortices of a positive circulation, as indicated by linear theory (see equation (2.86) and figure 2.21), no convergence could be found.

For the case when the point vortices are located at $(\pi - S/2, -1)$ and $(\pi + S/2, 1)$ the amplitude of the interfacial disturbance in comparison to the vortex circulations was examined. Figure 3.15 shows that away from $\Gamma \approx 0$ the increase in amplitude is
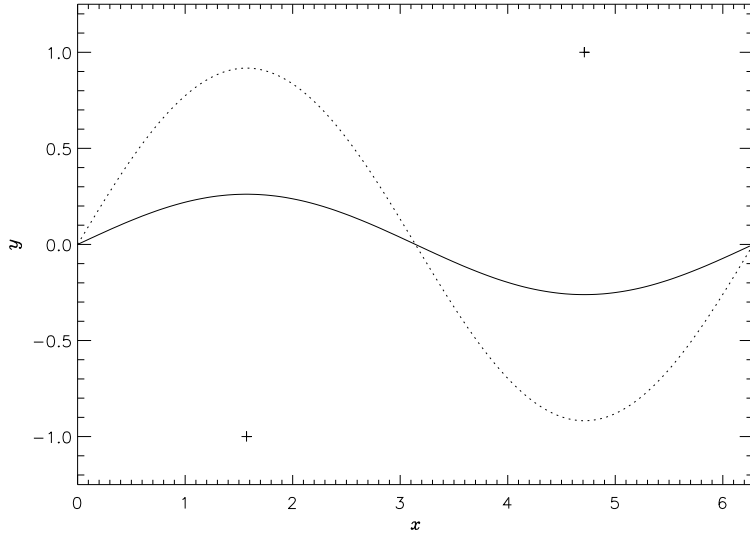
Figure 3.14: Non-linear profiles of $\eta(x)$ with $(\Gamma = -0.100000, U = 0.53628)$ (solid line) and $(\Gamma = -1.00000, U = 0.57582)$ (dotted line). $S = 3.14159$ in both cases and the $+$ symbols mark the locations of the point vortices.

approximately linear with the increase in vortex circulation. Also, for vortex circulations much greater than $\Gamma \approx 1.2$ the algorithm would not converge.

The robustness of the equilibria was again examined by using the non-linear profiles as initial conditions in a time dependent cylindrical contour dynamics algorithm. Time integration was carried out using a fourth order Runge-Kutta method and the time step and resolution parameter between vortex nodes were each set to 0.01 resulting in roughly $400 - 700$ nodes in the computational domain depending on the curvature of the interface. Figures 3.16 and 3.17 show the time evolution of the systems with the point vortices located at $(\pi - S/2, -1)$ and $(\pi + S/2, 1)$ and $(\Gamma = -0.1, U = 0.53628)$ and $(\Gamma = -1, U = 0.57582)$ respectively. Again, the value of $\Gamma$ refers to the circulation of the vortex initially in the region $x \in [0, 2\pi)$. $S_0$ was 3.14159 in both cases. When $\Gamma = -0.1$ the configuration changed very little over large
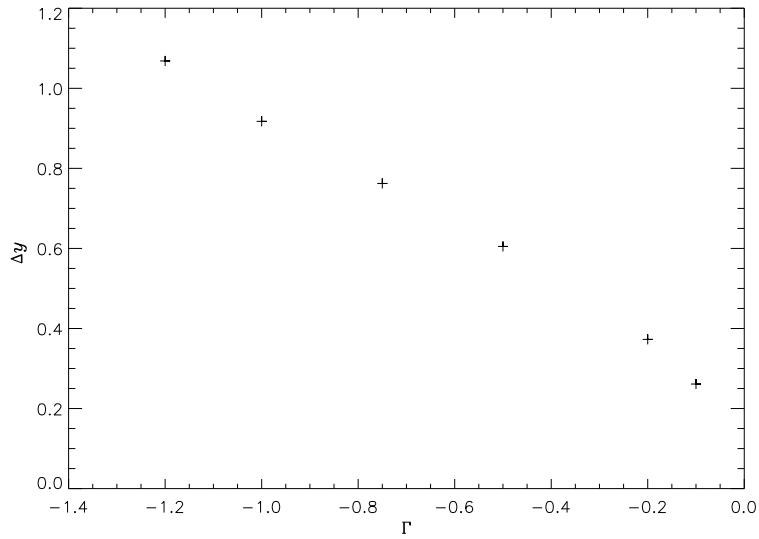
Figure 3.15: The difference in height between the highest and lowest interface nodes of the equilibria ($\Delta y$) for point vortices with $0.1 < \Gamma < 1.2$.

time periods. As shown in figure 3.16, even after 150 time units the configuration is very similar. As expected, the configuration with $\Gamma = -1$ undergoes a greater drift over the same time period, but, as was the case with the symmetric equilibria of the previous sections, the equilibria remains visibly unchanged for a reasonable amount of time ($t = 50$) and then the drift away from its equilibrium position is slow. Thus, these results indicate that the anti-symmetric equilibria computed in this section are also of a stable nature.

## 3.3  Planar anti-symmetric equilibrium

The planar anti-symmetric configuration of chapter 2.1 (see figure 2.1 for a sketch of the configuration) is now considered. Planar equilibria are computed using very
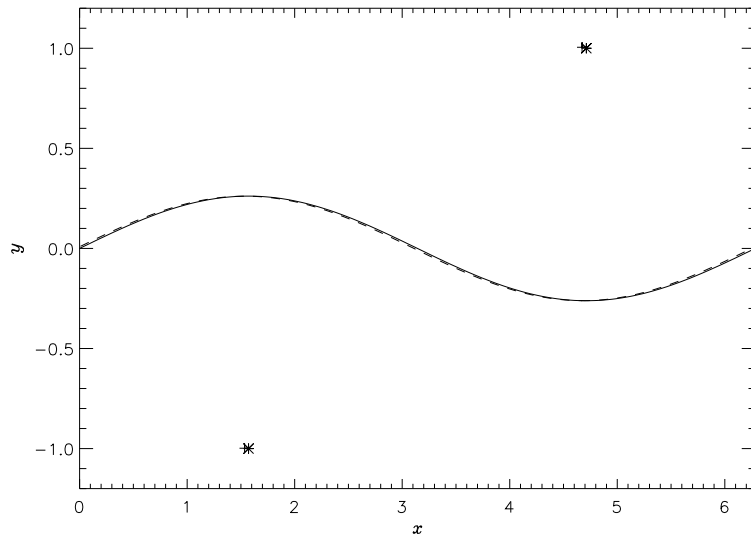
Figure 3.16: Numerical equilibrium of figure 3.14 with ($\Gamma = -0.1, U = 0.53628$) at $t = 0$ (solid line and asterisk) and at $t = 150$ (dashed line and +).
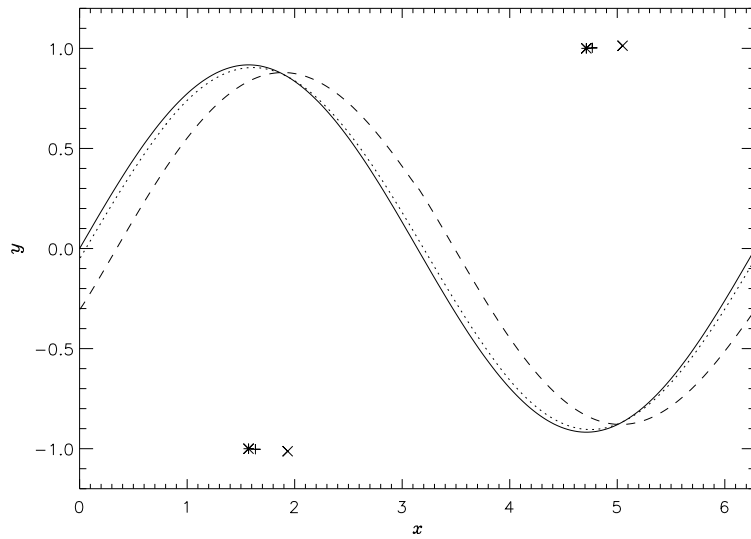


Figure 3.17: Numerical equilibrium of figure 3.14 with ($\Gamma = -1.0, U = 0.57582$) at $t = 0$ (solid line and asterisk), $t = 50$ (dotted line and +) and at $t = 150$ (dashed line and X).

similar methods to those presented in the previous sections of this chapter, the main difference being that velocity fields are now computed using a planar contour dynamics algorithm as opposed the cylindrical algorithm. In fact, owing to the similarity of the problems, the algorithm presented in section 3.2 to iterate towards an equilibrium can be used with only two minor modifications: The domain now has $2N - 1$ nodes where $y_{2N-1} = y_1$ (this change only effects the computation of velocity fields owing to the interface and not the algorithm that iterates towards an equilibrium) and a wider computational domain must be used and the $x$-direction node resolution increased accordingly. This is due to the fact that the interface height, $\eta$, only tends to zero as $x \to \pm\infty$. It must therefore be insured that the computational domain is sufficiently wide such that $\eta$ is very small at its outer boundary. This was the first algorithm used in attempting to compute a planar anti-symmetric equilibrium. Here, the computational domain is chosen to be the region $x \in [-20, 20]$ and $N = 400$ giving an $x$-direction resolution of $\delta x = 0.05$.

The algorithm was initialised with various initial conditions including the linear equilibrium of chapter 2.1 with the interface height scaled down, a flat interface and various profiles of the form $\eta(x) = ax \exp(-x^2/b)$. A range of initial $U$ and $\Gamma$ were used in each case. However, convergence was not realised for any of these combinations. Various adjustments were made to the algorithm including fixing $\Gamma$ and the node $y_2 = 0$ along with $y_1 = 0$, extending the algorithm to include all $2N - 1$ nodes, using an averaged streamfunction (similar to that of section 3.1) and marching backwards through the domain instead of forwards. However, none of these methods led to convergence. This inability to obtain convergence from the numerical algorithm

along with the null result from linear theory (chapter 2.1) gives a good indication that no such equilibrium exists.

## 3.4  Summary

Corresponding non-linear equilibria have been computed for the periodic configurations considered in chapter 2, namely, a row of symmetrically placed vortices near a vorticity interface and a vortex street in a shear flow. For the symmetric configuration, the problem was considered for both when the vortices lie in the rotational and irrotational region of the flow. Periodicity was accounted for by considering the problem on the surface of the unit cylinder, where the cylinder represents one period of the configuration. For the planar anti-symmetric configuration (chapter 2.1), as with linear theory, no equilibrium state could be found.

Symmetric equilibria in which the vortex lies in the irrotational region of flow have similar characteristics to some of the small amplitude linear equilibria in that, the hump on the interface lies symmetrically above the vortex. As the vortex circulation increases, equilibria have larger amplitude disturbances on the interface or alternatively, there is a larger vortex-interface separation. Which of these states is achieved is dependent on the choice of initial conditions. Equilibria in which the interface lies within unit distance of the point vortex, or in which higher order modes are present, could not be found. Computed equilibria were proven to be robust by using them as initial conditions in a time dependent code with, only small drifts from equilibrium positions were observed over long time periods.

When the vortex lies in the rotational region of the flow, linear theory again proves

to be a good guide as to what shapes can be computed. In these equilibria, the hump on the interface was now placed anti-symmetrically above the vortex. Again, for a specific value of $\Gamma$, many equilibria could be computed. Equilibria with larger amplitude oscillations at the interface tend to have a lower vortex-interface separation along with a lower free stream velocity. Faster free stream velocities lead to a flatter interface shapes with a greater vortex-interface separation. The equilibria were again shown to be robust giving a good indication of their stability.

For the vortex street configuration, interface shapes were found in which the interface curved towards the vortices when $\Gamma > 0$ and away from them when $\Gamma < 0$ (here $\Gamma$ refers to the circulation of the vortex in the region $x \in [0, \pi]$). However, when the vortices were placed at unit distance from the interface, only equilibria with $\Gamma < 0$ could be found. Equilibria were again used as initial conditions in a time dependent code and again only underwent small deviations over long periods of time giving a good indication that they are stable. It is hoped that the equilibria computed here may be of help in explaining the longevity of some vortical configurations observed in planetary atmospheres and oceans.

# Chapter 4

# Vortex-wave interaction on the surface of a sphere

Strong zonal shear flows are frequently observed in the Earth's atmosphere and ocean and also on the giant planets. Such shear flows are able to support wave motion and it is of interest to understand how small, intense vortices interact with these flows. One area of such interactions in the Earth's atmosphere is the Gulf stream. Meanders of the Gulf stream can sometimes detach and form cyclonic or anti-cyclonic structures. The resulting interaction between these detached eddies and the Gulf stream play an important role in water vapour mixing across the Atlantic region and hence in the weather patterns seen across much of Western Europe. With this region in mind, Stern and Flierl (1987) consider the interaction between a point vortex and shear flows on the $f$-plane in which two regions of constant vorticity owing to the shear flow are separated by a single interface. Results showed that an anticyclonic vortex located in the region of high vorticity generated a perturbation

upon the interface resulting in a "westward" propagation. Results also demonstrated that when the vortex was located sufficiently close to the interface, the vortex would cause the interface to wrap around it. Bell (1990) considers time-dependent vortex-wave interaction in flows with piecewise constant vorticity of the type considered in chapter 2 and 3. He shows that for a vortex-wave interaction in a planar shear flow, a positive (cyclonic) vortex drifts in the direction of increasing potential vorticity by radiating interfacial waves, while a negative (anti-cyclonic) vortex will drift towards regions of lower vorticity. Then, with applications to transport and mixing between rotational and irrotational flows, Atassi (1998) considers the problem of point vortex interaction with a wall-bounded shear layer. The study showed that the interaction between the point vortex and shear layer is strongest when the vortex and layer are of opposite signed vorticity. Strong interactions resulted in the ejection of fluid from the shear layer and such ejections were associated with a significant rise in the magnitude of wall pressure.

Much research has been conducted into the interaction of point vortices with topography that give rise to a background potential vorticity distribution (see appendix B). Near continental margins where sharp variations in depth occur, such as the Gulf of Mexico, to leading order local variations in potential vorticity are dominated by sharp topographic gradients and it is of interest to examine how such variations in depth effect the motion of eddies. McDonald (1998) considers the motion of an intense point vortex near an infinite escarpment in the plane. Intense in this context means that the vortex circulation time is much shorter than the time scale associated with wave propagation. Owing to the conservation of potential vorticity, at small times,

an intense cyclone's motion is towards regions of lower potential vorticity whilst an anticyclones motion is in the opposite direction. Following this initial motion, a steady motion parallel to the escarpment ensues before the vortex resonates with the topographic wave field resulting in cyclones drifting slowly towards regions of higher ambient potential vorticity and anticyclones drifting slowly away from such regions. The remaining cases of moderate and weak point vortices are considered in Dunn et al. (2001). White and McDonald (2004) then consider the analogous two-layer fluid problem. The two-layer stratification is chosen such that the height of topography in the upper layer is a small fraction of the overall depth enabling the use of quasi-geostrophic theory which implies that in the upper layer the vorticity is, again, piecewise constant. Weak vortices in the lower-fluid layer propagate mainly due to their image in the topography whilst upper-layer vortices propagate much slower and produce comparatively small amplitude topographic waves. In Newton and Sakajo (2007) the interaction of a ring of point vortices with a background vorticity initially in solid body rotation is considered.

The present chapter considers the time dependent problem of a point vortex on the surface of the non-rotating unit sphere with a background distribution of vorticity consisting of two opposite signed caps. Unlike previous work conducted in the plane, on the sphere there is periodicity in the zonal direction. Also, as mentioned in the beginning to chapter 2, the curvature of the sphere introduces a shielding effect. The point vortex forcing induces waves upon the vorticity interface which, in turn, perturb the zonally symmetric flow. The resultant coupled motion of the point vortex and waves is investigated. Analytic results valid for linear interfacial waves are first

presented. A non-linear stability analysis of the coupled motion is then followed by numerical computations of the problem using a spherical contour dynamics algorithm based on Dritschel (1989) and applications of the model to planetary vortices are considered.

## 4.1 Problem formulation and linear solution

The system consists of a single point vortex of circulation $\Gamma$ on the unit sphere in the presence of a background piecewise constant vorticity distribution. In spherical polar co-ordinates, $\phi$ is the azimuthal angle between $0$ and $2\pi$ and $\theta$ is the latitudinal angle between $-\pi/2$ and $\pi/2$. The system consists of two caps of vorticity given by $\omega_S$ in the southern cap and $\omega_N$ in the northern cap. The two caps are separated by an initially flat interface located at $\theta = \theta_0$. At time $t = 0$ a point vortex is 'switched on' at a position $(\phi_{pv}(0), \theta_{pv}(0))$. The net vorticity is zero as required by the Gauss constant,

$$\int\int_S (\omega_N + \omega_S + \Gamma\delta(\phi - \phi_{pv}, \theta - \theta_{pv}))dA = 0. \tag{4.1}$$

A sketch of the configuration is shown in figure 4.1. The linearised problem is initially considered enabling an analytical derivation of the equations of motion. These linear equations are valid for (i) short times, or (ii) for weak vortices or (iii) for vortices far from the interface. Crucially, all these conditions imply the interface displacement is small.

In seeking a linear solution it is simplest to consider the problem in Cartesian coordinates, $(x, y, z)$, where $x = \cos\theta\cos\phi$, $y = \cos\theta\sin\phi$ and $z = \sin\theta$. Let the
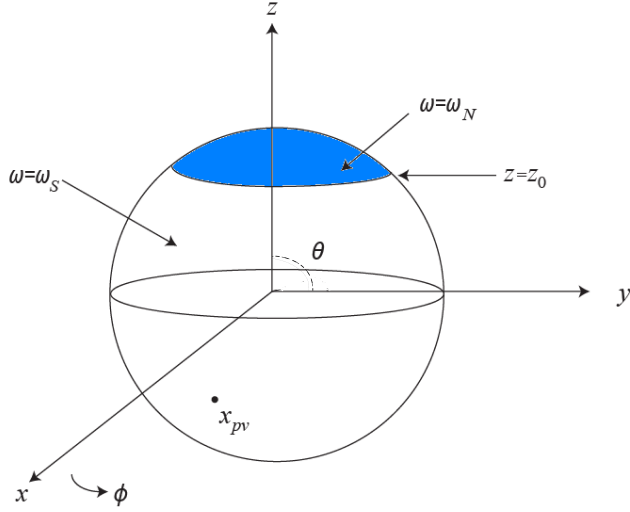
Figure 4.1: Sketch of the problem under consideration. $0 \leq \phi < 2\pi$ is the azimuthal angle and $-\pi/2 \leq \theta \leq \pi/2$ is the latitudinal angle. The point vortex is located at $\mathbf{x}_{pv}$ and the vorticity jump is initially along a flat interface at the height $z_0$, separating regions of constant vorticity $\omega_N$ and $\omega_S$.

interface position be given by

$$z(\phi, t) = z_0 + \hat{z}(\phi, t), \tag{4.2}$$

where $z_0 = \sin \theta_0$. The point vortex is located at $\mathbf{x}_{pv}(t) = (x_{pv}(t), y_{pv}(t), z_{pv}(t))$ and without loss of generality let $\mathbf{x}_{pv}(0) = ((1 - z_{pv}^2(0))^{1/2}, 0, z_{pv}(0))$. From Dritschel and Polvani (1992), the equations of motion owing to a piecewise constant vorticity jump $c_k$ in an inviscid, incompressible fluid on the surface of a sphere can be written in the form

$$\frac{d\mathbf{x}}{dt} = \mathbf{u}(\mathbf{x}) = -\frac{1}{4\pi}\tilde{\omega} \oint_{c_k} \log |\mathbf{x} - \mathbf{X}_k|^2 d\mathbf{X}_k, \tag{4.3}$$

where $\tilde{\omega} = \omega_N - \omega_S$ is the vorticity jump across the interface $c_k$. The streamfunction owing to a point vortex of strength $\Gamma$ on the unit sphere can be written as (Polvani

and Dritschel 1993)

$$\psi = \frac{\Gamma}{4\pi} \log(1 - \mathbf{x} \cdot \mathbf{x}_{pv}). \tag{4.4}$$

Note that the global circulation owing to (4.4) is zero, since it includes a uniform background vorticity of $-\Gamma/4\pi$. The azimuthal and vertical velocities owing to the point vortex are then retrieved via

$$\frac{d\phi}{dt} = -\frac{\partial \psi}{\partial z} \qquad \text{and} \qquad \frac{dz}{dt} = \frac{\partial \psi}{\partial \phi}. \tag{4.5}$$

To solve the linear vortex-wave interaction problem, the perturbation at the interface, $\hat{z}(\phi, t)$, is written as a time dependent Fourier series

$$z(\phi, t) = z_0 + \sum_{n=1}^{\infty} \left( a_n(t) \cos(n\phi) + b_n(t) \sin(n\phi) \right). \tag{4.6}$$

First, $z$-direction perturbations at the interface are considered. Substituting (4.6) into (4.3) gives the self induced vertical velocity of the vorticity jump on the contour. The total vertical velocity at the contour is given by summing this with the vertical velocity field due to the point vortex:

$$\frac{dz}{dt} = \frac{\partial z}{\partial t} + \Omega_0 \frac{\partial z}{\partial \phi} = -\frac{\tilde{\omega}}{4\pi} \int_0^{2\pi} \log |\mathbf{x}(\phi, t) - \mathbf{X}(\alpha, t)|^2 \left. \frac{\partial z}{\partial \phi} \right|_\alpha d\alpha$$

$$\tag{4.7}$$

$$+ \frac{\partial}{\partial \phi} \frac{\Gamma}{4\pi} \log(1 - \mathbf{x}_0 \cdot \mathbf{x}_{pv}),$$

where, consistent with linear theory, $\Omega_0 = \tilde{\omega}/2$ is the angular velocity at an unperturbed interface (Dritschel and Polvani 1992). Evaluating and linearising the terms in (4.7) gives

$$|\mathbf{x}(\phi, t) - \mathbf{X}(\alpha, t)|^2 = 2 \cos^2 \theta_0(t)(1 - \cos(\alpha - \phi)),$$

$$\tag{4.8}$$

$$\mathbf{x}_0 \cdot \mathbf{x}_{pv} = (1 - z_{pv}^2)^{\frac{1}{2}} (1 - z_0^2)^{\frac{1}{2}} \cos(\phi - \phi_{pv}) + z_{pv} z_0.$$

Substitution of (4.6) and (4.8) into (4.7) gives

$$\sum_{n=1}^{\infty} \left( \dot{a}_n \cos n\phi + \dot{b}_n \sin n\phi + n\frac{\tilde{\omega}}{2}(-a_n \sin n\phi + b_n \cos n\phi) \right) =$$

$$- \frac{\tilde{\omega}}{4\pi} \int_0^{2\pi} \log|1 - \cos(\alpha - \phi)| \left( \sum_{n=1}^{\infty} n \left( -a_n \sin n\alpha + b_n \cos n\alpha \right) \right) d\alpha \qquad (4.9)$$

$$+ \frac{\Gamma}{4\pi} \left[ \frac{(1 - z_{pv}^2)^{\frac{1}{2}}(1 - z_0^2)^{\frac{1}{2}} \sin(\phi - \phi_{pv})}{1 - (1 - z_{pv}^2)^{\frac{1}{2}}(1 - z_0^2)^{\frac{1}{2}} \cos(\phi - \phi_{pv}) - z_{pv}z_0} \right].$$

Evaluation of the integrals in (4.9) yield the following results:

$$\int_0^{2\pi} \log|1 - \cos(\alpha - \phi)| \left( \sum_{n=1}^{\infty} (-na_n) \sin n\alpha \right) d\alpha = 2\pi \sum_{n=0}^{\infty} a_n \sin n\phi,$$

$$(4.10)$$

$$\int_0^{2\pi} \log|1 - \cos(\alpha - \phi)| \left( \sum_{n=1}^{\infty} nb_n \sin n\alpha \right) d\alpha = -2\pi \sum_{n=0}^{\infty} b_n \cos n\phi.$$

Substituting the integrals (4.10) back into (4.9) gives

$$\sum_{n=1}^{\infty} \left[ \left( \dot{a}_n + \frac{\tilde{\omega}}{2}(n - 1)b_n \right) \cos n\phi + \left( \dot{b}_n - \frac{\tilde{\omega}}{2}(n - 1)a_n \right) \sin n\phi \right]$$

$$(4.11)$$

$$= \frac{\Gamma}{4\pi} \left[ \frac{(1 - z_{pv}^2)^{\frac{1}{2}}(1 - z_0^2)^{\frac{1}{2}} \sin(\phi - \phi_{pv})}{1 - (1 - z_{pv}^2)^{\frac{1}{2}}(1 - z_0^2)^{\frac{1}{2}} \cos(\phi - \phi_{pv}) - z_{pv}z_0} \right] = \frac{\Gamma}{4\pi} F(\phi, t).$$

The RHS forcing term of (4.11) is now written as a Fourier series such that

$$F(\phi, t) = \sum_{n=1}^{\infty} \left( c_n(t) \cos n\phi + d_n(t) \sin n\phi \right), \qquad (4.12)$$

where

$$c_n(t) = \frac{1}{\pi} \int_0^{2\pi} F(\phi, t) \cos n\phi \, d\phi$$

(4.13)

$$= \frac{1}{\pi} \int_0^{2\pi} \frac{(1 - z_{pv}^2)^{\frac{1}{2}}(1 - z_0^2)^{\frac{1}{2}} \sin(\phi - \phi_{pv})}{1 - (1 - z_{pv}^2)^{\frac{1}{2}}(1 - z_0^2)^{\frac{1}{2}} \cos(\phi - \phi_{pv}) - z_{pv} z_0} \cos n\phi \, d\phi,$$

and

$$d_n(t) = \frac{1}{\pi} \int_0^{2\pi} F(\phi, t) \sin n\phi \, d\phi$$

(4.14)

$$= \frac{1}{\pi} \int_0^{2\pi} \frac{(1 - z_{pv}^2)^{\frac{1}{2}}(1 - z_0^2)^{\frac{1}{2}} \sin(\phi - \phi_{pv})}{1 - (1 - z_{pv}^2)^{\frac{1}{2}}(1 - z_0^2)^{\frac{1}{2}} \cos(\phi - \phi_{pv}) - z_{pv} z_0} \sin n\phi \, d\phi.$$

Gradshteyn and Ryzhik (1965) give an identity to evaluate integrals of the form seen

in (4.13) and (4.14) which can be written as (Dritschel and Polvani 1992)

$$-\frac{m}{2\pi} \int_0^{2\pi} \log(1 - z_a z_b - (1 - z_a^2)^{\frac{1}{2}}(1 - z_b^2)^{\frac{1}{2}} \cos\beta) e^{im\beta} d\beta = \left( \frac{1 - z_>}{1 + z_>} \frac{1 + z_<}{1 - z_<} \right)^{m/2}, \quad (4.15)$$

where $z_>$ stands for the maximum of $z_a$ and $z_b$ and $z_<$ for the minimum. For the case

when $z_0 > z_{pv}$, i.e. when the point vortex is located in the southern cap of vorticity,

the integrals of (4.13) and (4.14) give

$$c_n(t) = -2\sin(n\phi_{pv}) \left( \frac{1 - z_0}{1 + z_0} \frac{1 + z_{pv}}{1 - z_{pv}} \right)^{n/2},$$

(4.16)

$$d_n(t) = 2\cos(n\phi_{pv}) \left( \frac{1 - z_0}{1 + z_0} \frac{1 + z_{pv}}{1 - z_{pv}} \right)^{n/2},$$

where $\phi_{pv}$ is a function of time determined by integrating the angular velocity of the

point vortex in the azimuthal direction owing to the background vorticity distribution.

This angular velocity is derived below. When $z_0 > z_{pv}$, from (4.15) it is seen that $c_n(t)$

and $d_n(t)$ will be given by swapping $z_0$s with the $z_{pv}$s in equations (4.16). To obtain a coupled set of equations relating the time dependent Fourier coefficients $a_n(t)$ and $b_n(t)$, (4.16) are substituted into (4.11) giving

$$\dot{a}_n(t) + \frac{\tilde{\omega}}{2}(n-1)b_n(t) = \frac{\Gamma}{4\pi}c_n(t),$$

(4.17)

$$\dot{b}_n(t) - \frac{\tilde{\omega}}{2}(n-1)a_n(t) = \frac{\Gamma}{4\pi}d_n(t),$$

where $n \in \mathbb{Z}^+$. An immediate consequence of (4.17) is the impossibility of a steady solution provided $z_0 \neq \pm 1$ i.e. the vortex is not at a pole. In particular, putting $n = 1$ in (4.17) implies that $\dot{a}_1$ and $\dot{b}_1$ cannot both be simultaneously zero implying unsteady behaviour for all time. This of course does not preclude the existence of non-linear steady solutions.

An infinite set of coupled ordinary differential equations for coefficients $a_n(t)$ and $b_n(t)$, $n = 1, 2, 3, \ldots$ has now been derived. In order to close the linear system, the equations motion for the point vortex, $\dot{z}_{pv}$ and $\dot{\phi}_{pv}$ are now derived. An approximate solution can then be obtained by truncating at $n = N$ and solving an $2N+2$ coupled system of ODEs to give the resulting dynamics of the interface and point vortex.

First, an equation for the azimuthal velocity, $u_{pv}$, at the point vortex is sought. The angular velocity is then given by

$$\dot{\phi} = u_{pv}/(1 - z_{pv}^2)^{1/2}.$$

(4.18)

Using (4.3), the azimuthal velocity at the point vortex is given by

$$u_{pv} = -\frac{\tilde{\omega}}{4\pi} \oint \log |\mathbf{x}_{pv} - \mathbf{X}(\alpha)|^2 \frac{\partial}{\partial \alpha}\left[(1 - z^2(\alpha))^{\frac{1}{2}}\sin\alpha\right] d\alpha.$$

(4.19)

Expanding and linearising the log term of (4.19) gives

$$|\mathbf{x}_{pv} - \mathbf{X}(\alpha)|^2 = 2(1 - z_0 z_{pv} - (1 - z_0^2)^{\frac{1}{2}}(1 - z_{pv}^2)^{\frac{1}{2}}\cos(\alpha - \phi_{pv})), \tag{4.20}$$

and therefore

$$u_{pv} = -\frac{\tilde{\omega}}{4\pi}\int_0^{2\pi}\log|1 - z_0 z_{pv} - (1 - z_0^2)^{\frac{1}{2}}(1 - z_{pv}^2)^{\frac{1}{2}}\cos(\alpha - \phi_{pv})|$$

$$\times \frac{\partial}{\partial\alpha}\left[(1 - z^2(\alpha))^{\frac{1}{2}}\sin\alpha\right]d\alpha$$

$$\tag{4.21}$$

$$= -\frac{\tilde{\omega}}{4\pi}\int_0^{2\pi}\log|1 - z_0 z_{pv} - (1 - z_0^2)^{\frac{1}{2}}(1 - z_{pv}^2)^{\frac{1}{2}}\cos(\alpha - \phi_{pv})|$$

$$\times \left((1 - z_0^2)^{\frac{1}{2}}\cos\alpha - \frac{z_0 \hat{z}_\alpha \sin\alpha}{(1 - z_0^2)^{\frac{1}{2}}}\right)d\alpha,$$

where $\hat{z} = \sum_{n=1}^{\infty}(a_n(t)\cos n\alpha + b_n(t)\sin n\alpha)$ (see (4.6)). Equation (4.21) represents the flow due to an unperturbed interface plus a small modification due to perturbations at the interface induced by the point vortex, that is

$$u_{pv} = u_0 + u'_{pv}, \tag{4.22}$$

where (Polvani and Dritschel 1993)

$$u_0 = -\frac{\tilde{\omega}}{4\pi}\int_0^{2\pi}\log|1 - z_0 z_{pv} - (1 - z_0^2)^{\frac{1}{2}}(1 - z_{pv}^2)^{\frac{1}{2}}\cos(\alpha - \phi_{pv})|(1 - z_0^2)^{\frac{1}{2}}\cos\alpha\, d\alpha$$

$$= \frac{\tilde{\omega}}{2}(1 - z_0)\left(\frac{1 + z_{pv}}{1 - z_{pv}}\right)^{\frac{1}{2}},$$

$$\tag{4.23}$$

and

$$u'_{pv} = -\frac{\tilde{\omega}}{4\pi}\int_0^{2\pi}\log|1 - z_0 z_{pv} - (1 - z_0^2)^{\frac{1}{2}}(1 - z_{pv}^2)^{\frac{1}{2}}\cos(\alpha - \phi_{pv})|$$

$$\times \frac{-z_0\sin\alpha}{(1 - z_0^2)^{\frac{1}{2}}}(-na_n\sin n\alpha + nb_n\cos n\alpha)d\alpha$$

(4.24)

$$= \frac{\tilde{\omega}z_0}{4\pi(1 - z_0^2)^{\frac{1}{2}}}\int_0^{2\pi}\log|1 - z_0 z_{pv} - (1 - z_0^2)^{\frac{1}{2}}(1 - z_{pv}^2)^{\frac{1}{2}}\cos(\alpha - \phi_{pv})|$$

$$\times \sin\alpha(-na_n\sin n\alpha + nb_n\cos n\alpha)d\alpha.$$

To evaluate the integral in (4.24) the substitution $\beta = \alpha - \phi_{pv}$ in made and use is made of the following trigonometric identities

$$\sin\alpha\sin\beta = \frac{1}{2}(\cos(\alpha - \beta) - \cos(\alpha + \beta)),$$

(4.25)

and

$$\sin\alpha\cos\beta = \frac{1}{2}(\sin(\alpha - \beta) + \sin(\alpha + \beta)).$$

(4.26)

This yields

$$u'_{pv} = \sum_{n=1}^{\infty}\frac{n\tilde{\omega}z_0}{4(1 - z_0^2)^{\frac{1}{2}}}\left[\frac{1}{n-1}\left(\frac{1 - z_0}{1 + z_0}\frac{1 + z_{pv}}{1 - z_{pv}}\right)^{\frac{n-1}{2}}(a_n\cos(n-1)\phi_{pv} - b_n\sin(n-1)\phi_{pv})-\right.$$

$$\left.\left(\frac{1 - z_0}{1 + z_0}\frac{1 + z_{pv}}{1 - z_{pv}}\right)^{\frac{n+1}{2}}(a_n + b_n n + 1)\cos(n+1)\phi_{pv}\right].$$

(4.27)

An equation for $u'_{pv}$ has now been derived. However, (4.27) is not valid for $n = 1$ and therefore, this is considered as a special case. Substituting $n = 1$ into (4.24) and

again using the substitution $\beta = \alpha - \phi_{pv}$ gives

$$u'_{pv} = \frac{\tilde{\omega} z_0}{8\pi(1-z_0^2)^{\frac{1}{2}}} \int_0^{2\pi} \log |1 - z_0 z_{pv} - (1-z_0^2)^{\frac{1}{2}}(1-z_{pv}^2)^{\frac{1}{2}} \cos \beta|$$

$$\times (a_1(\cos 2\phi_{pv} \cos 2\beta - 1) + b_1 \sin 2\phi_{pv} \cos 2\beta) d\beta$$

$$\tag{4.28}$$

$$= -\frac{\tilde{\omega} z_0}{8(1-z_0^2)^{\frac{1}{2}}} \left[ (a_1 \cos 2\phi_{pv} + b_1 \sin 2\phi_{pv}) \left( \frac{1-z_0}{1+z_0} \frac{1+z_{pv}}{1-z_{pv}} \right) \right.$$

$$\left. + a_1 \left( \log[1 - z_0 z_{pv}] + \log \left[ \frac{1 + (1-R^2)^{\frac{1}{2}}}{2} \right] \right) \right]$$

where $R = (1-z_0^2)^{1/2}(1-z_{pv}^2)^{1/2}/(1-z_0 z_{pv})$. Equations (4.18), (4.23), (4.27) and (4.28) give finally

$$\dot{\phi}_{pv} = -\frac{\omega_s}{(1-z_{pv}^2)^{\frac{1}{2}}} \left( \frac{1+z_{pv}}{1-z_{pv}} \right)^{\frac{1}{2}} - \frac{\tilde{\omega} z_0}{8(1-z_0^2)^{\frac{1}{2}}(1-z_{pv}^2)^{\frac{1}{2}}}$$

$$\times \left[ (a_1 \cos 2\phi_{pv} + b_1 \sin 2\phi_{pv})A + a_1 \log \left[ (1-z_0 z_{pv}) \frac{1 + (1-R^2)^{\frac{1}{2}}}{2} \right] \right]$$

$$+ \sum_{n=2}^{\infty} \frac{n\tilde{\omega} z_0}{4(1-z_0^2)^{\frac{1}{2}}(1-z_{pv}^2)^{\frac{1}{2}}} \left[ \frac{1}{n-1} A^{\frac{n-1}{2}}(a_n \cos(n-1)\phi_{pv} - b_n \sin(n-1)\phi_{pv}) \right.$$

$$\left. - A^{\frac{n+1}{2}} \left( \frac{a_n + b_n}{n+1} \right) \cos(n+1)\phi_{pv} \right].$$

$$\tag{4.29}$$

where, consistent with linear theory, $A = \left( \frac{1-z_0}{1+z_0} \frac{1+z_{pv}(0)}{1-z_{pv}(0)} \right)$ is a constant. Now, from

(4.3) the point vortex velocity in the $z$-direction is given by

$$\dot{z}_{pv} = -\frac{\tilde{\omega}}{4\pi} \int_0^{2\pi} \log |\mathbf{x}_{pv} - \mathbf{X}(\alpha)|^2 \frac{\partial z}{\partial \alpha} d\alpha. \tag{4.30}$$

Substituting in the expression for $z$ given in (4.6) gives

$$\dot{z}_{pv} = -\frac{\tilde{\omega}}{4\pi} \int_0^{2\pi} \log |\mathbf{x}_{pv} - \mathbf{X}(\alpha)|^2 \sum_{n=1}^{\infty} (-na_n \sin n\alpha + nb_n \cos n\alpha) d\alpha. \tag{4.31}$$

Expanding and linearising $|\mathbf{x}_{pv} - \mathbf{X}(\alpha)|^2$, and then integrating gives

$$\dot{z}_{pv} = -\sum_{n=1}^{\infty} \frac{\tilde{\omega}}{2} A^{\frac{n}{2}} (a_n \sin n\phi_{pv} - b_n \cos n\phi_{pv}). \tag{4.32}$$

Truncating the sums in (4.29) and (4.32) at $n = N$ gives a system of $2N + 2$ ODEs for the $2N + 2$ unknowns $a_1, .., a_N, b_1, .., b_N, \phi_{pv}$ and $z_{pv}$ governing the motion of a point vortex located below a vorticity interface on the surface of the sphere in the limit of small amplitude waves upon the interface. In the following sections, the short time behaviour of the system and the effect of truncating the system at $n = 1$ will be examined. Following this, the linear system will be truncated at higher $n$ and the resulting motion examined.

## 4.2 Short time behaviour and the $n = 1$ system

Initially, only the primary mode will be considered. Truncating (4.16), (4.17), (4.29) and (4.32) at $n = 1$ gives the following system of ODEs

$$\dot{a}_1(t) = -\frac{\Gamma}{2\pi} A^{\frac{1}{2}} \sin \phi_{pv},$$

$$\dot{b}_1(t) = \frac{\Gamma}{2\pi} A^{\frac{1}{2}} \cos \phi_{pv},$$

$$\dot{\phi}_{pv}(t) = -\frac{\omega_s}{(1 - z_{pv}^2)^{\frac{1}{2}}} \left(\frac{1 + z_{pv}}{1 - z_{pv}}\right)^{\frac{1}{2}} - \frac{\tilde{\omega} z_0}{8(1 - z_0^2)^{\frac{1}{2}}(1 - z_{pv}^2)^{\frac{1}{2}}} \left[(a_1 \cos 2\phi_{pv} + b_1 \sin 2\phi_{pv})A\right.$$

$$\left. + a_1 \log\left[(1 - z_0 z_{pv})\frac{1 + (1 - R^2)^{\frac{1}{2}}}{2}\right]\right],$$

$$\dot{z}_{pv}(t) = -\frac{\tilde{\omega}}{2} A^{\frac{1}{2}}(a_1 \sin \phi_{pv} - b_1 \cos \phi_{pv}),$$

$$(4.33)$$

with initial conditions $a_1(0) = b_1(0) = 0$, $\phi_{pv}(0) = 0$ and $0 \leq z_{pv}(0) \leq 1$.

Before considering the full $n = 1$ system, it is insightful to make further relevant approximations to examine the initial movements of the system. When $t$ is close to zero it is reasonable to assume that the azimuthal velocity of the point vortex is constant (i.e. its velocity is that due to an unperturbed interface). This is the velocity given in (4.23). Taking the southern cap to be of negative vorticity and northern cap to be of positive vorticity, an eastward azimuthal velocity will be induced at the vortex. (A westward zonal velocity is induced in the case where the vorticity of the

caps is reversed). Therefore, for small times, the azimuthal position of the vortex is approximately

$$\phi_{pv} = \Omega_0 t, \tag{4.34}$$

where $\Omega_0$ is given by (4.23) and (4.18). The Fourier coefficients $a_1$ and $b_1$ can now be integrated to give

$$a_1(t) = \frac{\Gamma A^{1/2}}{\Omega_0} \cos \Omega_0 t - \frac{\Gamma A^{1/2}}{\Omega_0},$$

$$\tag{4.35}$$

$$b_1(t) = \frac{\Gamma A^{1/2}}{\Omega_0} \sin \Omega_0 t,$$

and therefore from (4.33)

$$\dot{z}_{pv} = \frac{\tilde{\omega} A \Gamma}{2\Omega_0} \sin \Omega_0 t. \tag{4.36}$$

For $t << \Omega_0^{-1}$ (4.36) gives

$$\dot{z}_{pv} \approx \frac{\tilde{\omega} A \Gamma t}{2}. \tag{4.37}$$

Equation (4.37) shows that $\text{sgn}(\dot{z}_{pv}) = \text{sgn}(\tilde{\omega}\Gamma)$ (where $\tilde{\omega} = \omega_N - \omega_S$ is the vorticity jump across the interface) and thus a point vortex in a region of same-signed vorticity will initially move away from the interface, whilst a point vortex in a region of opposite-signed vorticity will initially move towards it. While this analysis has been carried out assuming $z_{pv} < z_0$, the same conclusion holds for $z_{pv} > z_0$. The required modifications for this case are the substitution of $\bar{A} = \left( \frac{1+z_0}{1-z_0} \frac{1-z_{pv}}{1+z_{pv}} \right)$ for $A$ and $\bar{\Omega}_0 = \frac{\tilde{\omega}}{2} \frac{1+z_0}{1+z_{pv}}$ for $\Omega_0$ throughout the preceding analysis. Additionally, integrating (4.36) with respect to time gives

$$z_{pv}(t) = \frac{\tilde{\omega} A \Gamma}{2\Omega^2} (1 - \cos \Omega t) + z_{pv}(0). \tag{4.38}$$

Thus, equation (4.38) predicts that point vortices undergo periodic oscillation with $z_{pv}(0)$ being one extremum of the motion.

The full $n = 1$ system valid for all time is now considered. The coupled system of equations (4.33) is solved using numerical integration. Here, a fourth order Runge-Kutta scheme is used and the timestep is set to $\delta t = 0.01$. Results confirm that a point vortex in a region of same-sign vorticity initially moves away from the interface, while a point vortex in a region of opposite signed vorticity initially moves towards it. Point vortices with sufficiently weak circulation then undergo periodic meridional oscillation while orbiting the sphere. The magnitude of 'sufficiently weak' is determined by the initial latitudinal position of the interface, the vorticity jump across it and the point vortex proximity to it. Figure 4.2 demonstrates this behaviour, showing the initial movement towards the interface and the periodic meridional oscillation as the vortex travels around the sphere. In figure 4.3 a snapshot of this system is shown at $t = 1$. The forcing at the interface due to the point vortex has caused a peak to form ahead of the point vortex and a trough to its rear. If the sign of point vortex circulation is reversed the form of the interfacial wave is also reversed: a peak forms to the rear of the point vortex while a trough leads it.

Initially $(t = 0^+)$ interfacial disturbances induce purely meridional motion. Following this, the interfacial wave always forms to initially oppose the zonal motion of the vortex. However, as the expression for the interface is only valid for small amplitude waves, the correction to the zonal velocity is always small. This is a clear difference to planar topography cases, such as that of McDonald (2004), where the free stream velocity is independent of the magnitude of the vorticity jump. For a vor-
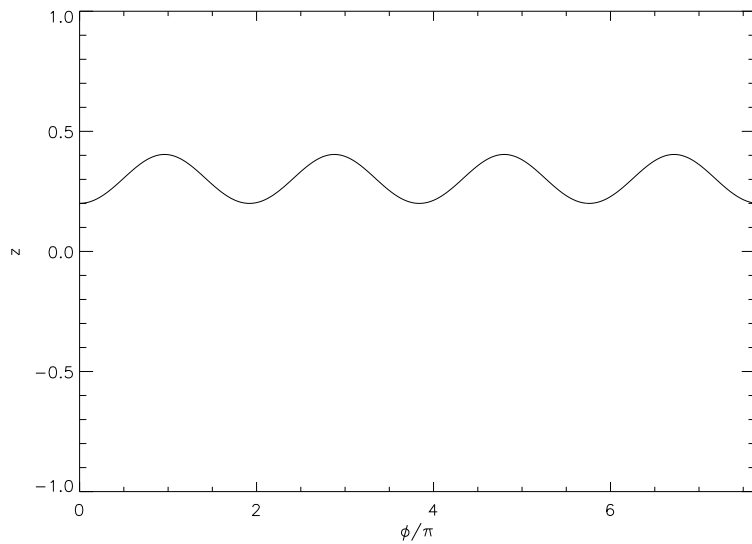
Figure 4.2: Vortex trajectory $0 \leq t \leq 20$ according to $n = 1$ linear theory. The vortex has $\Gamma = 1.0$, is initially at $z_{pv}(0) = 0.2$ and the interface has $z_0 = 0.5$. The vorticity is $-1$ in the southern cap.
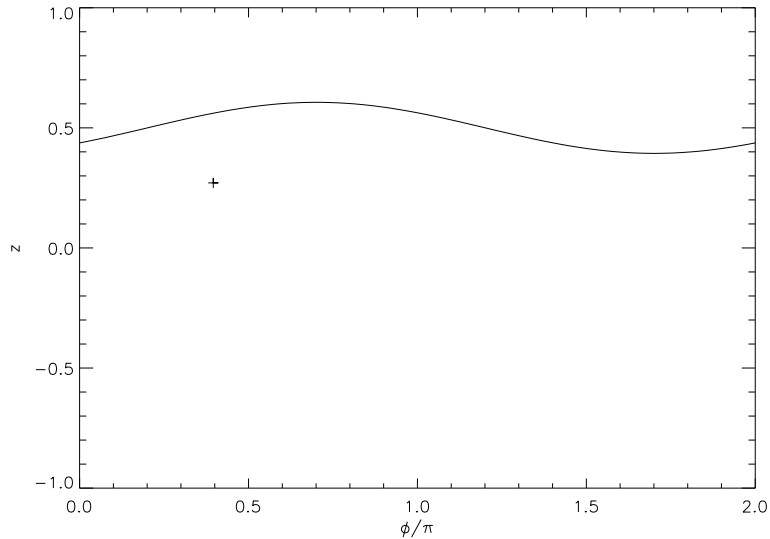


Figure 4.3: A snapshot of the system considered in figure 4.2 at $t = 1$. The vortex location is shown by $+$, and the solid line is the vortical interface.

tical interface on the sphere, the unperturbed angular velocity, $\Omega_0$, and that due to interfacial perturbations are proportional to the vorticity jump $\tilde{\omega}$ across the interface. This means that a low $\Omega_0$ can only result in a weak correction to the zonal flow.

The long time behaviour of the system shown in figure 4.2 was examined up to times of $t \approx 1000$. The motion seen in figure 4.2 persists for these very large times demonstrating the stability of the system. This is a characteristic of all systems within this regime i.e. if a configuration is such that the vortex undergoes meridional oscillation, this oscillation will persist for long periods of time.

When a strong point vortex is in a region of the same signed vorticity, the vortex will rapidly move away from the interface towards the pole. It is simple to show from (4.17) that these polar locations are equilibria e.g. if $z_{pv} < z_0$ then when $z_{pv} = -1$ (the South Pole) $\dot{a}_1 = \dot{b}_1 = \dot{z}_{pv} = 0$ and when $z_{pv} > z_0$ then $z_{pv} = 1$ (the North Pole) again gives $\dot{a}_1 = \dot{b}_1 = \dot{z}_{pv} = 0$. Further, (4.38) indicates that a point vortex located at a pole in a region of same sign vorticity will be a stable equilibrium. Slight meridional perturbations to the vortex will result in a velocity at the vortex pushing it back towards the pole. On the other hand, polar vortices in regions of opposite signed vorticity are unstable equilibria, since perturbations away from the pole will induce a meridional velocity pulling the vortex away from the pole.

Linear theory also predicts that if a point vortex in a region of same signed vorticity is sufficiently strong, it will always reach the pole regardless of its initial proximity to the vorticity interface. Clearly, for a strong vortex within close proximity to the interface, large amplitude waves will quickly develop on the interface invalidating linear theory. This result is therefore not expected to hold true in fully non-linear

computations. Figure 4.4 shows the trajectory of a point vortex in this regime and figure 4.5 the corresponding contour at $t = 1$. In the linear $n = 1$ calculation, the vortex passes below $z = -1$ and then proceeds to oscillate, never returning above $z = -1$. Clearly the trajectory is non-physical once the vortex has passed below $z = -1$. Nevertheless, the result still gives insight into the stability of vortices in polar regions and the initial movements of strong point vortices in these regions. The interface of figure 4.5 is 'opposite' in shape to that of 4.3 owing to the different sign circulation of the vortex i.e. a trough now precedes the vortex. Also, owing to the large circulation of the vortex, large amplitude waves have developed upon the interface. For strong point vortices in regions of opposite signed vorticity, linear theory breaks down as the point vortex rapidly approaches the interface exciting large amplitude disturbances, and then 'crossing' the interface.

## 4.3   Truncating at $n > 1$

In this section, the effect of truncating (4.16), (4.17), (4.29) and (4.32) at $n > 1$ on the resulting dynamics is examined. As in section 4.2, the system of $2N + 2$ ODEs resulting from truncating at $n = N$ is solved numerically using a fourth order Runge-Kutta scheme with timestep $\delta t = 0.01$.

Truncating at $n > 1$ alters the dynamics to varying degrees according to the vortex strength, vorticity jump across the interface and the vortices proximity to the interface. Figure 4.6 compares vortex trajectories for solutions truncated at $n = 1, n = 3$ and $n = 50$ for a weak vortex initially at a reasonable distance from the interface. This is a highly linear case and, as expected, the three trajectories are very
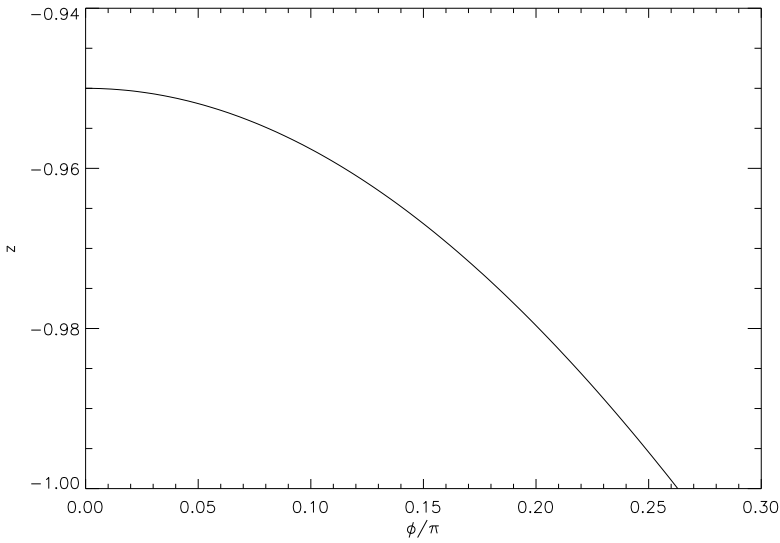
Figure 4.4: Vortex trajectory predicted by $n = 1$ linear theory for a vortex with circulation $\Gamma = -10.0$, initially located at $z_{pv} = -0.95$ with interface height $z_0 = 0.0$ and a vorticity of $-1$ in the southern cap. The motion shown is from $t = 0$ up to $t = 5$.

similar with the $n = 3$ and $n = 50$ trajectories being almost identical.

Figure 4.7 compares the trajectories for a vortex initially within closer proximity to the interface. The $n = 3$ and $n = 50$ results rapidly diverge from the $n = 1$ results. As expected, when higher frequency modes are excited on the interface, $a_2$ and $b_2$ (and possibly higher order modes), are non-negligible. The vortex trajectories are then no longer meridional oscillations and demonstrate more complex behaviour. Again, the $n = 3$ and $n = 50$ results are almost identical. Figure 4.8 shows a snapshot of the wave-vortex system at $t = 5$ using $n = 50$. Higher order modes are now clearly present on the interface and although oscillations upon the interface are still relatively small, the $n = 1$ equations fail to capture the behaviour of the system except at very small times. Also $z_{pv}$ in figure 4.7 eventually exceeds the value of $z_0$ and continues
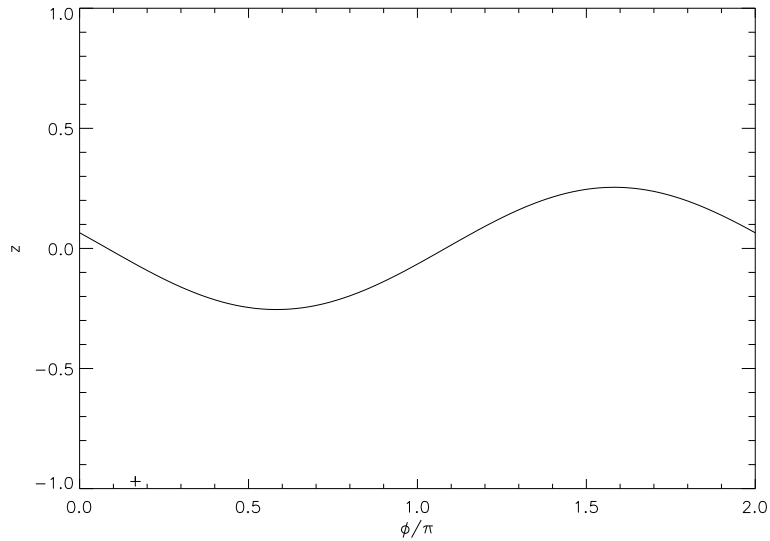
Figure 4.5: A snapshot of the system considered in figure 4.4 at $t = 1$. The vortex location is indicated by the + and the solid line represents the vortical interface.

to rise. As expected, the linear results, except in highly linear cases are valid only over a short period of time. These results also show that terms with $n$ greater than three are very small and, in the vast majority of cases, have a negligible effect on the system's dynamics.

## 4.4   A non-linear stability calculation

In section 4.2 only the linear stability of the system was considered. A non-linear stability argument and account of initial vortex drift based on angular momentum conservation is now presented. In the system's initial state, the angular momentum is given by

$$L = \int \int \omega z \, dA, \tag{4.39}$$
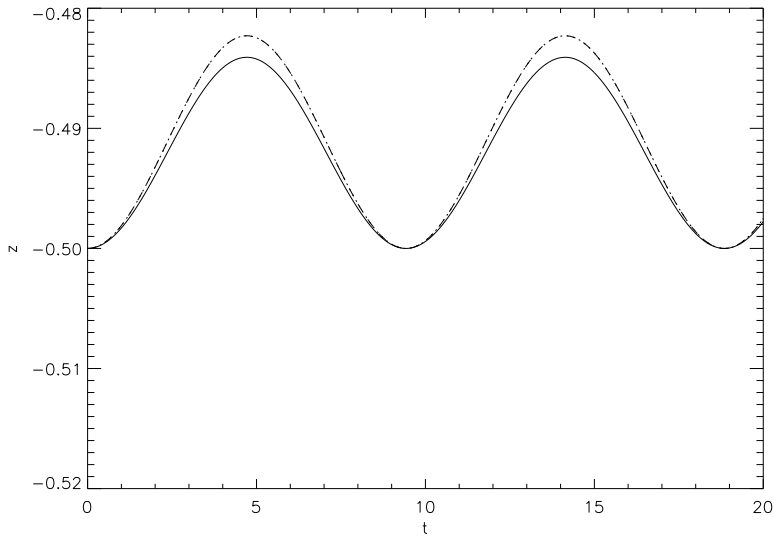
Figure 4.6: Vortex meridional oscillation in time for the linear solution truncated at $n = 1$ (solid line), $n = 3$ (dotted line) and $n = 50$ (dashed line). The vortex has $\Gamma = 0.1$, is initially at $z_{pv}(0) = -0.5$ and the interface has at $z_0 = 0.5$. The vorticity is $-1$ in the southern cap.

where $\omega$ is the vorticity and $A$ is the sphere's surface. The vorticity associated with the point vortex is given by

$$\omega_{pv} = \Gamma\delta(\phi - \phi_{pv}, z - z_{pv}) - C, \tag{4.40}$$

where $C$ is a constant. The angular momentum associated with the point vortex is therefore given by

$$L_{pv} = \Gamma z_{pv}. \tag{4.41}$$
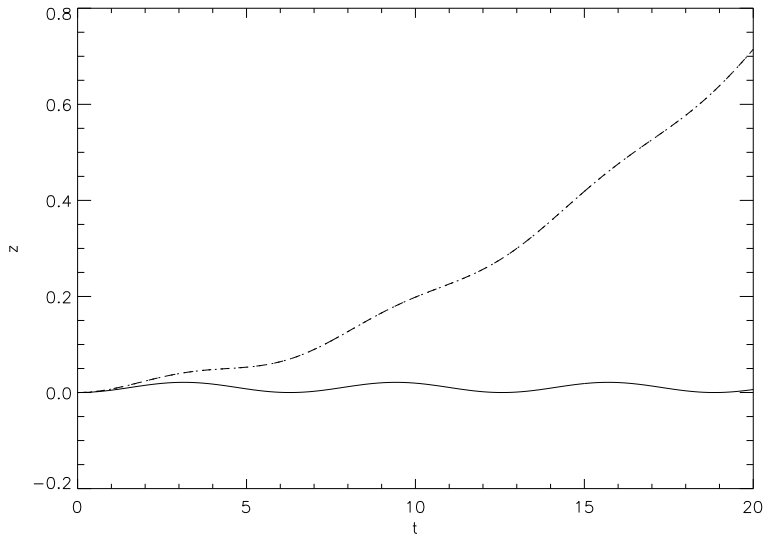
Figure 4.7: Vortex meridional oscillation in time for the linear solution truncated at $n = 1$ (solid line), $n = 3$ (dotted line) and $n = 50$ (dashed line). The vortex has $\Gamma = 0.1$, is initially at $z_{pv}(0) = 0.0$ and the interface has at $z_0 = 0.5$. The vorticity is $-1$ in the southern cap.

For the unperturbed (i.e. at $t = 0$) vorticity caps, the angular momentum is

$$L_{cap} = \int_0^{2\pi} \left( \int_{-1}^{z_0} \omega_S + \int_{z_0}^{1} \omega_N \right) dz d\phi$$

$$= \pi \left[ (\omega_N - \omega_S)(1 - z_0^2) \right] \qquad (4.42)$$

$$= 2\pi \omega_N (1 - z_0).$$
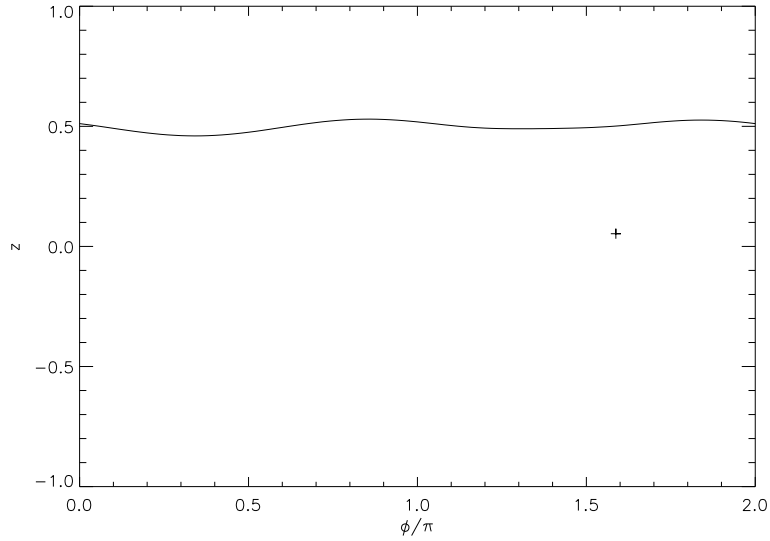
Figure 4.8: Snapshot of the vortex (+) and interface for the same system as the $n = 50$ vortex trajectory shown in figure 4.7 at $t = 5$.

The angular momentum due to the perturbed interface is now calculated. In this calculation it is assumed that the perturbation can be written as $z = z_0 + \hat{z}(\phi)$, then

$$L_{pert} = \int \int \omega z dA - L_{cap},$$

$$= \int_0^{2\pi} \int_{-1}^{z_0+\hat{z}} \omega_S z dz d\phi + \int_0^{2\pi} \int_{z_0+\hat{z}}^1 \omega_N z dz d\phi - L_{cap},$$

$$= \frac{\omega_S}{2} \int_0^{2\pi} \left( (z_0 + \hat{z})^2 - 1 \right) d\phi + \frac{\omega_N}{2} \int_0^{2\pi} \left( 1 - (z_0 + \hat{z})^2 \right) d\phi - L_{cap}, \qquad (4.43)$$

$$= \frac{\omega_S}{2} \int_0^{2\pi} \hat{z}^2 d\phi - \frac{\omega_N}{2} \int_0^{2\pi} \hat{z}^2 d\phi,$$

$$= -\frac{\omega_N}{1 + z_0} \int_0^{2\pi} \hat{z}^2 d\phi.$$

In order to examine the stability of the system it is first shown that $L$ is constant. From (4.39)

$$L = \int_0^{2\pi} \int_{-\frac{\pi}{2}}^{\frac{\pi}{2}} \omega \cos\theta \sin\theta d\theta d\phi$$

$$= \int_0^{2\pi} \int_{-\frac{\pi}{2}}^{\frac{\pi}{2}} \left( \sin\theta \frac{\partial}{\partial\theta} \left( \cos\theta \frac{\partial\psi}{\partial\theta} \right) + \tan\theta \frac{\partial^2\psi}{\partial\phi^2} \right) d\theta d\phi \qquad (4.44)$$

$$= -\int_0^{2\pi} \int_{-\frac{\pi}{2}}^{\frac{\pi}{2}} \cos^2\theta \frac{\partial\psi}{\partial\theta} d\theta d\phi,$$

from the periodicity in the system. But $u = -\partial\psi/\partial\theta$ and thus

$$L = \int_0^{2\pi} \int_{-\frac{\pi}{2}}^{\frac{\pi}{2}} u \cos^2\theta d\theta d\phi$$

$$(4.45)$$

$$= \int\int u \cos\theta dA \equiv L_{total},$$

where $L_{total}$ is the total angular momentum which is a conserved quantity in the system. $L_{total} = L_{pv} + L_{cap} + L_{pert}$ (where $L_{cap} = constant$) and thus from equations (4.42) and (4.43) there are two cases to consider: (i) $\Gamma > 0$, $\omega_N > 0$ and (ii) $\Gamma < 0$, $\omega_N > 0$. For (i), if the disturbance amplitude at the interface increases then according to (4.43) $L_{pert}$ decreases and thus $L_{pv}$ must increase, meaning $z_{pv}$ increases. Therefore a positive vortex at the North Pole is stable and a positive vortex at the South Pole unstable. For case (ii), again, if the amplitude of the interface increases, $L_{pert}$ will decrease and thus $L_{pv}$ must again increase meaning $z_{pv}$ must decrease. There is therefore stability for a negative vortex at the South Pole and instability for a negative vortex at the North Pole.

These calculations reinforce the results obtained from linear theory and demonstrate that even in non-linear regimes, provided the interface can be written as $z = z_0 + \hat{z}(\phi)$ (i.e. the interface does not become a multi-valued function of $\phi$), the poles are stable equilibrium locations for vortices in regions of the same sign vorticity and unstable for vortices in regions of opposite sign vorticity.

In the following section the results of linear theory are used to verify time-dependent non-linear contour dynamics results. Vortex trajectories obtained from contour dynamics will be tested against those predicted by linear theory. Following this, more 'exotic' non-linear behaviour will be considered.

## 4.5 Non-linear computations

The results of the linear theory presented in sections 4.2 and 4.3 are now used to validate computations using the contour dynamics algorithm (Dritschel 1988). The algorithm is described in appendix A. In the following computations, the resolution parameter between nodes was set to 0.01 and time integration is carried out using a fourth-order Runge-Kutta scheme with timestep $\delta t = 0.01$. Following each timestep, the interfacial nodes are redistributed according to the local curvature meaning that, even for highly non-linear cases, accurate vortex trajectories and interface shapes can be computed.

Figure 4.9 displays the vortex trajectories computed using contour dynamics and those given by $n = 100$ linear theory for the highly linear case previously considered in section 4.6, that is, $\Gamma = 0.1$, $z_{pv}(0) = -0.5$, $z_0 = 0.5$ and $\omega_S = -1$ for time up to $t \approx 20$. There is excellent agreement between linear theory and contour dynamics

in this case. When a large number of terms are included in the linear analysis, the trajectories are almost identical over long time scales. Figure 4.10 then shows a comparison of the vortex trajectories given by $n = 100$ linear theory and contour dynamics for a more non-linear system: the system considered in figure 4.7 with $\Gamma = 0.1$, $z_{pv}(0) = 0.0$, $z_0 = 0.5$ and $\omega_S = -1$. Linear theory and contour dynamics are in very good agreement up to $t \approx 5$. However, for time greater than $t = 5$ the trajectories begin to diverge. From $t \approx 11$ onwards the trajectories diverge rapidly and linear theory completely fails to capture the non-linear motion. Linear theory predicts that the vortex continues to rise towards the interface, whereas contour dynamics predicts that after the initial movement of the vortex towards the interface, it then begins to move away from it.

For systems with moderate strength point vortices, where the waves on the interface can no longer be considered linear, but remain single-valued with respect to the azimuthal coordinate $\phi$, a point vortex in a region of same/opposite sign vorticity will undergo periodic oscillation with a mean drift away/towards the contour depending on the sign of their vorticity relative to the surrounding fluid (see for example the vortex trajectory in figure 4.11 for a case when the drift is away from the interface). Vortices in regions of opposite sign vorticity that drift towards the contour eventually come within close proximity of the contour and induce highly nonlinear wrapping of the contour. Vortices in regions of same signed vorticity drift away from the contour and towards the pole with the rate of drift decreasing as the vortex moves further away from the contour. The system, in effect, becomes more linear as relative distance between vortex and contour increases. In moderate strength vortex systems,

complex non-linear waves develop on the contour but the basic structure predicted by linear theory is still present i.e. a peak or trough on the interface leads the vortex. Figure 4.11 shows an example of such a vortex trajectory along with the trajectory predicted by linear theory. Initially, linear theory and contour dynamics are in good agreement. However, similar to the example considered in figure 4.7, after $t \approx 4$, linear theory fails to capture the motion of the vortex.

Figure 4.12 shows an example of a system in which interfacial wrapping eventually occurs. The system consists of a vortex with $\Gamma = 3$ and $z_{pv}(0) = -0.5$, the interface is initially at $z_0 = 0.5$ and $\omega_S = -1$. The vortex initially precesses about the sphere whilst drifting towards the interface. Eventually the vortex comes within close proximity to the interface, inducing the interface to wrap around it, and as a result, the vortices azimuthal precession is slowed.
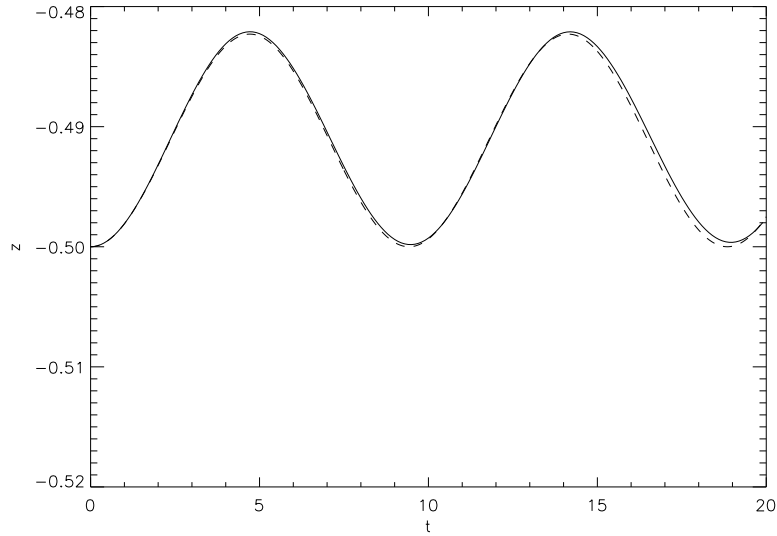


Figure 4.9: Comparison of vortex latitude as a function of time computed using contour dynamics (solid line) and $n = 100$ linear theory (dashed line) for the same system shown in figure 4.2.
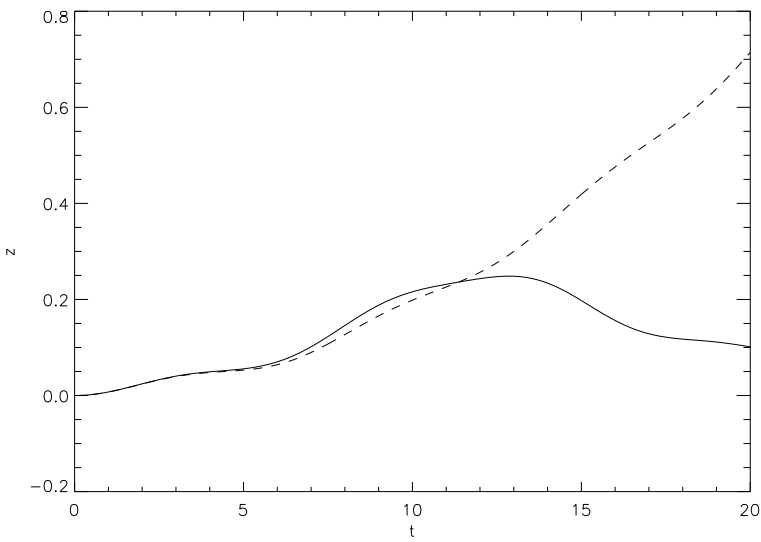
Figure 4.10: Comparison of vortex latitude as a function of time computed using contour dynamics (solid line) and $n = 100$ linear theory (dashed line) for the same system shown in figure 4.7.

The stability of polar vortices is examined by placing a vortex at a small distance from a pole and observing the resulting meridional oscillations given by contour dynamics. Oscillations of vortices with negative and positive circulations, initially located close to the south pole, in a sea of negative vorticity are shown in figures 4.13 and 4.14 respectively. Figure 4.13 does indeed show that the pole is a stable attractor for vortices in a sea of same signed vorticity. The vortex initially moves towards the pole and then undergoes a meridional oscillation that is damped in time. In such systems, high amplitude waves are excited at the interface, but owing to the distance of the vortex from the interface, no interfacial wrapping (multivaluedness ) occurs. However, if such a vortex is initially positioned further from the pole and sufficiently close to the interface, it first drifts towards the pole but the interface is
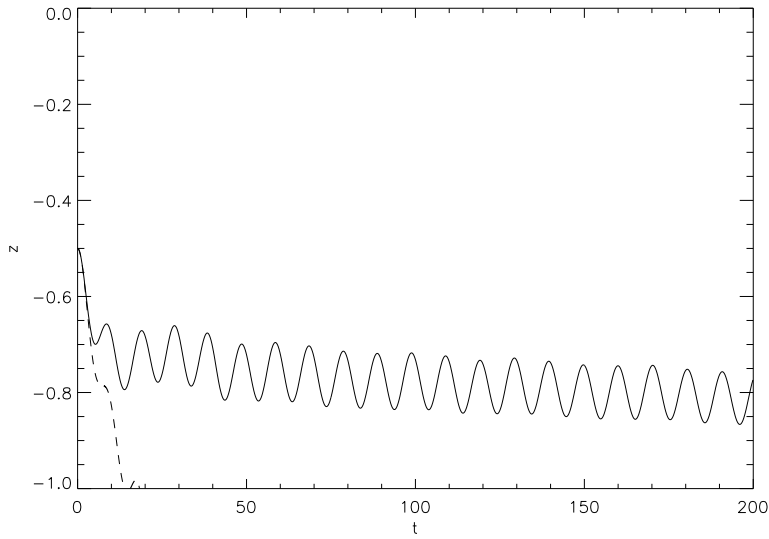
Figure 4.11: Vortex latitude as a function of time computed using contour dynamics (solid line) and $N = 50$ linear theory (dotted line) for a vortex with $\Gamma = -0.5$ and $z_{pv}(t = 0) = -0.5$ with interface $z_0 = 0$. The vorticity of the southern cap is $-1$.

'pulled down' towards the vortex and quickly wraps around it, halting its motion towards the pole. Also, in figure 4.13(b) it is seen that, owing to the large amplitude waves excited on the interface the azimuthal motion of the vortex is reversed (seen by the spiralling vortex trajectory) and then oscillates in time, a phenomenon not seen in linear calculations.

When the circulation of the vortex is reversed (figure 4.14), the vortex initially moves rapidly away from the pole and towards the interface demonstrating the instability of the vortex at the pole in this configuration. However, owing to the strength of the vortex the interface is then 'pulled down' and wrapped around the vortex and complicated non-linear behaviour ensues.
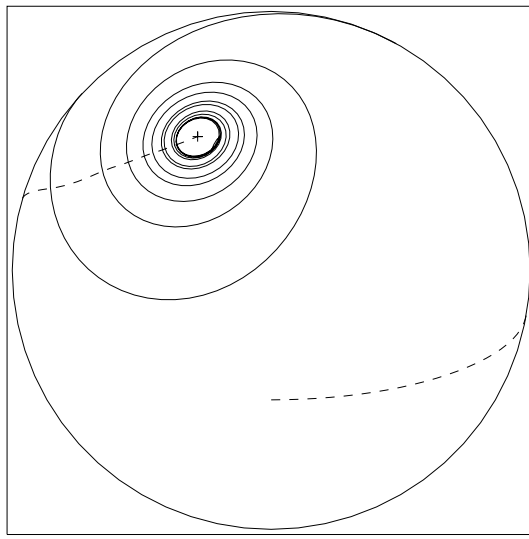
Figure 4.12: Contour dynamics results at $t = 9.5$ for a vortex with $\Gamma = 3$ with $z_{pv}(0) = -0.5$ and vorticity interface (solid line) initially at $z_0 = 0.5$ and $\omega_S = 1$. The dashed line indicates the vortex trajectory from $0 \leq t \leq 9.5$. The view is centred at $(0, 0)$.

## 4.6 Summary and applications to planetary vortices

The dynamics of a point vortex on a sphere with a single vorticity jump separating two caps of opposite sign constant vorticity have been considered. Linear theory has been used to derive a coupled system of ODEs describing the evolution of the vortex and modes along the interface. Analysis of the system showed that a point vortex in a region of same signed vorticity will initially move away from the interface while a vortex in a region of opposite signed vorticity will initially move towards it. Vortices with a sufficiently weak circulation at sufficient distance from the interface then undergo periodic meridional oscillation whilst precessing about the sphere. In

(a)                                                    (b)
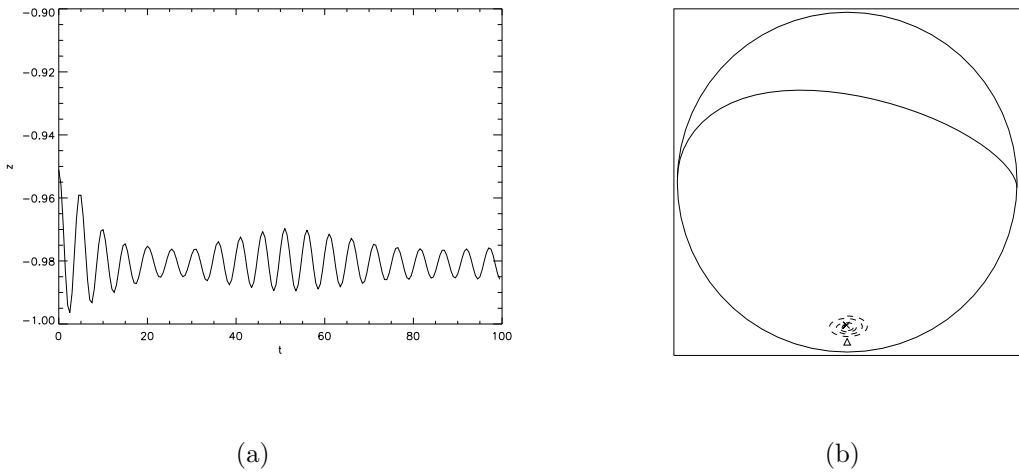
Figure 4.13: (a) Vortex meridional displacement as a function of time computed using contour dynamics for a vortex with $\Gamma = -10.0$, initially at $z_{pv}(0) = -0.95$ and the interface initially located at $z_0 = 0.0$. The vorticity is $-1$ in the southern cap. (b) A snapshot of the system at $t = 100$. The dashed line indicates the vortex trajectory from $0 \leq t \leq 100$ and the triangle indicates the location of the South Pole.
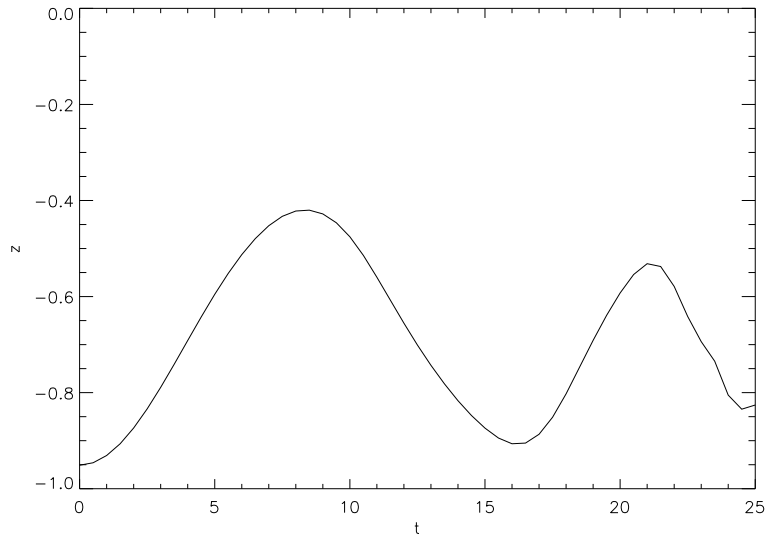


Figure 4.14: Vortex trajectory given by contour dynamics for a vortex with $\Gamma = 10.0$, initially at $z_{pv}(0) = -0.95$ and the interface initially located at $z_0 = 0.0$. The vorticity is $-1$ in the southern cap.

configurations where the vortex is initially closer to the interface, higher order modes are excited upon the interface and the point vortex no longer undergoes a constant meridional oscillation. In such systems, it is essential to truncate equations (4.16), (4.17), (4.29) and (4.32) at $n > 1$ in order to capture the motion of the system over even short time periods. The linear dynamics were largely insensitive to different levels of truncation after $n = 5$. Linear theory also predicts that a polar vortex in a region of same signed vorticity is at a stable equilibrium, whilst a polar vortex in a region of opposite signed vorticity is at an unstable equilibrium. This result is demonstrated to be true for non-linear systems, providing the interface can be written as a Fourier series.

The fully non-linear problem was studied using a contour dynamics algorithm for vortex dynamics on the surface of the unit sphere. The short time behaviour of systems examined using contour dynamics was in good agreement with linear theory. For highly linear configurations, contour dynamics and linear theory showed good agreement over large periods of time. In more non-linear configurations, contour dynamics was in good agreement with linear theory over short periods of time before more complicated non-linear behaviour dominated the motion of the interface.

Contour dynamics results also verified the existence of the stable equilibrium predicted by linear theory for a polar vortex in a region of same signed vorticity. Recent observations obtained by NASA's Cassini spacecraft (Dyudina et al. 2009) have revealed the existence of an intense polar storm at Saturn's South Pole. The storm is cyclonic and as noted in Polvani and Dritschel (1993), the system considered here may be, to first order, very relevant in studying the global dynamics of Saturn. B A Smith

(1982) points to evidence suggesting that on Saturn there exists a so called zonal 'ribbon' with a strong vorticity gradient near the equator. The global circulation is anticyclonic to the north of the ribbon and cyclonic to its south resulting in the mean winds at the equator being generally to the east. There is therefore the possibility that there exists a strong cyclonic storm surrounded by a cyclonic sea i.e. the polar storm has the same signed vorticity as its surrounding fluid. As discussed previously in this chapter, for a cyclonic southern cap, the South Pole would be a stable equilibrium for a cyclonic storm such as the one observed at Saturn's South Pole. This result therefore offers a possible dynamic explanation explaining the presence and stability of Saturn's polar storm.

Systems with moderate strength vortices displayed a variety of possible behaviour. One characteristic of such systems was that the vortex would generally drift away from the interface if surrounded by a sea of same signed vorticity and towards it if surrounded by a sea of opposite signed vorticity. For vortices surrounded by seas of same signed vorticity, the rate of drift away from the interface would decrease with distance from the interface and the vortex trajectory would slowly settle down into a meridional oscillation while precessing around the sphere. As mentioned above, vortices in seas of opposite signed vorticity drift towards the interface resulting in the amplitude of disturbances at the interface growing as the vortex gets closer. Generally, the vortex would get within close enough proximity of the interface to eventually induce wrapping, thus halting the meridional drift of the vortex.

# Chapter 5

# Finite area vortex motion on a sphere with impenetrable boundaries

Vortex motion in the presence of impenetrable boundaries is an important problem in vortex dynamics due to its relevance in modeling geophysical flows, especially oceanographic flows. Oceanic eddies frequently interact with topography such as ridges and coastlines, the resulting interactions can play an important role in ocean circulation and various other ocean processes. For example, With such motivation in mind, Pedlosky (1994) models the flow of the stratified abyssal ocean in the presence of a partial meridional (north-south) barrier, Sheremet (2001) the passage of a western boundary current across a gap and Nof (1995) the rotating exchange flow through a narrow gap between large-scale ocean basins. Since deep ocean vortices, observed to exist at depths up to 4km (McWilliams 1985), can propagate large distances they will

frequently encounter mid-ocean ridges occurring at similar depths (e.g. the Walvis Ridge in the South Atlantic). Due to their role in ocean circulation and the transport of tracers, understanding the circumstances in which they are able to penetrate gaps in ridges is important. In addition to deep ocean vortex-topography interactions, surface trapped vortex structures also frequently interact with complex topography. One such example is the collision of North Brazil Current Rings with the Lesser Antilles (Fratantoni et al. 1995). For large-scale vortex structures, the curvature of the Earth can play a significant role in the evolution of the system. Hence it is desirable to develop methods that accurately compute vortex behaviour on the surface of a sphere.

For problems involving vortex motion in planar bounded domains governed by the two-dimensional Euler equations with the vorticity distribution chosen such that it is a singular point in the domain (a point vortex), progress can be made using conformal mapping techniques. Provided a conformal mapping exists between the domain and a relatively simpler domain in which a vortex Hamiltonian (Kirchhoff-Routh path function) (Saffman 1992) can be constructed, this Hamiltonian along with information from the mapping gives the Hamiltonian in the original domain from which the vortex trajectory can be deduced. Such point vortex systems can give a good indication of the dynamics of a vortex patch with constant vorticity, especially when the boundary of a vortex remains close to circular since the velocity field exterior to a circular vortex patch is identical to that of a point vortex with the same circulation. However, in many geophysical systems it is of interest to consider cases in which the vorticity distribution is not singular but a finite region of vorticity which is able to deform, and

when in close proximity to solid objects or other regions of vorticity can filament or even split. The conformal mapping method is not directly applicable to such cases as a finite area vortex patch is governed by Poisson's equation which is not invariant under conformal mapping. The dynamics exterior to the vortex are, however, governed by Laplace's equation and are hence invariant under conformal mapping. Thus, provided the vorticity distributions being considered are piece-wise constant, contour dynamics (Dritschel 1989) along with the invariance of the irrotational exterior flow under conformal mapping can be utilized to examine such systems. Johnson and McDonald (2004a) consider the planar problem of a point vortex near a gap in a plate with and without ambient flows for which exact solutions of point vortex trajectories are obtained through deriving the appropriate vortex Hamiltonian. In the absence of ambient flows a vortex travelling towards the gap will pass through the gap and travel back along the other side of the plate if its far-field distance from the plate is less than half the gap width. Otherwise the vortex will leap across the gap. A method for computing the motion of finite area patches of constant vorticity near such a gap for which the invariance of the irrotational exterior flow under conformal mapping and the numerical method of contour dynamics are utilized are then presented. When the vortex boundary remains close to circular the centroid of the patch follows that of the point vortex trajectory very closely. Cases in which the vortex is 'pinched' against the gap edge can lead to filamentation and even vortex splitting can occur. This method is extended to study the motion of point vortices and vortex patches near two circular cylinders of arbitrary radii (Johnson and McDonald 2004b) and near a barrier with two collinear gaps (Johnson and McDonald 2005). For point vortices,

Crowdy and Marshall (2005) generalized the study of Johnson and McDonald (2004b) to domains of arbitrary connectivity, presenting a method for constructing a vortex Hamiltonian in a bounded or unbounded domain containing an arbitrary number of cylinders of arbitrary radii. The method of Crowdy and Marshall (2005) is used to study the motion of a point vortex through gaps in walls in Crowdy and Marshall (2006). Trajectories about gaps in a wall off a coastline and in an unbounded ocean are considered. Some results from Johnson and McDonald (2005) are reproduced and extended to domains of higher connectivity. In a recent study, Crowdy and Surana (2008) present a method for implementing contour dynamics in planar domains of arbitrary connectivity based on constructing the Green's function in a pre-image circular domain. Various examples are presented including the motion of a patch near an infinite wall, a gap in a wall and in a circular basin with multiple circular islands.

For planetary scale geophysical flows, it is clearly of interest to consider such problems on the surface of a sphere. As mentioned in chapter 4, moving from the plane to the sphere introduces new effects into the problem. The periodicity of the sphere introduces a 'feed back' effect and the curvature of the sphere can introduce 'shielding' effects. In the absence of topography on the sphere it is required that the total vorticity on the surface of the sphere is equal to zero: the Gauss integral constraint. Point vortex motion on the surface of the sphere in the presence of impenetrable boundaries is considered in the studies of Kidambi and Newton (2000) and Crowdy (2006). Kidambi and Newton (2000) use the method of images to derive exact point vortex trajectories for a spherical cap, longitudinal wedge, half-longitudinal wedge,

channel and rectangle. Due to limitations of the method of images, solutions for the wedge, half-wedge and rectangle are restricted to bounded geometries between the azimuthal angles of $\phi = 0$ and $\phi = \pi/m$ where $m$ is a positive integer. Crowdy (2006) presents a formulation based on a generalization of the Kirchhoff-Routh path function to the surface of a sphere, abandoning the need for special symmetries demanded by the method of images. The analog of the 'gap in a wall' problem of Johnson and McDonald (2004a) on the surface of a sphere is also considered. The impenetrable barrier considered lies along a great circle with longitude (or azimuthal angle) $\phi = 0, \pi$ except for a single, symmetrical gap centred about the south pole for $\theta \geq \theta_0$ where $0 \leq \theta \leq \pi$ is the co-latitude. For $\theta_0$ less than $0.6082\pi$ the south pole is an elliptic stationary point of the Hamiltonian in contrast to the planar case in which the centre of the gap is always a hyperbolic stationary point of the Hamiltonian (Johnson and McDonald 2004a). When $\theta_0$ exceeds this value a quantitative change in vortex behavior occurs and the Hamiltonian has a hyperbolic stationary point at the south pole and two symmetrical elliptic stationary points emerge at right angles to the plate. As $\theta_0$ is increased further the curvature of the spherical surface plays a lesser role in the dynamics in the vicinity of the gap and trajectories resemble those of the planar case close to the gap (Johnson and McDonald 2004a).

In the absence of impenetrable boundaries Dritschel (1988) extends the method of contour dynamics to the surface of a sphere. This method is has been used to model waves and vortices on a sphere (in the absence of boundaries) and compute steadily rotating vortex structures (Dritschel and Polvani 1992; Polvani and Dritschel 1993).

This chapter considers the motion of finite area patches of constant vorticity on

the non-rotating unit sphere with impenetrable boundaries. Techniques described in Johnson and McDonald (2004a) and Johnson and McDonald (2005) are extended to the surface of the sphere and used to examine vortex patch motion in bounded domains which is then compared to the exact point vortex trajectories (Crowdy 2006). The domains considered include the exterior to an ellipse of semimajor axis $a$ and semiminor axis $b$ in the stereographic plane, a longitudinal wedge and half-longitudinal wedge bounded between zero and an angle $\phi$ (where $0 < \phi < 2\pi$) and a thin barrier with two gaps. For the case when the semiminor axis of the ellipse is equal to zero (i.e. a gap in a plate, Crowdy 2006) the motion of the patch with compatible background flows is also considered.

As discussed above, Crowdy (2006) shows when the boundary is a gap in a plate, the point vortex Hamiltonian has an elliptic stationary point located symmetrically between the two plate edges (provided $\theta_0 < 0.6082\pi$). Thus, the possibility of stable steady vortices (V-states) located between the gap arises. Families of vortex equilibria for different gap widths are computed using a numerical method based on that of Pierrehumbert (1980) and their stability investigated.

Surana and Crowdy (2008) have also considered the motion of vortex patches on a sphere in the presence of boundaries using a modification of the method of Crowdy and Surana (2008). Their method also uses stereographic projection of the physical region of interest and also the patch itself (unlike in this work). They then conformally map to a canonical circular domain and use the results of Crowdy and Surana (2008) to show that a contour dynamics formulation exists.

The approach of presented in this chapter is complementary to that of Surana and

Crowdy (2008). It has the advantage of being straightforward to implement using a 'standard' contour dynamics routine on a sphere although here it is restricted (unlike Surana and Crowdy 2008) to singly and doubly connected domains. However, the method can, in principle, be used to tackle domains of any connectivity provided the region of interest can be mapped to a circular domain consisting of the unit disk with smaller circular disks excised in which the corresponding boundary value problem can be solved to obtain the appropriate irrotational flow field. The range of examples considered here complement those of Surana and Crowdy (2008). Additionally in this chapter background flows are considered, point vortex and patch trajectories are compared and a family of vortex equilibria residing in a gap are computed.

## 5.1   Contour dynamics in singly connected domains on a sphere

The system consists of a shallow layer of constant depth, incompressible and inviscid fluid in a simply connected bounded domain $\mathcal{D}$ on the surface of the unit sphere. Let $\Psi$ denote the total streamfunction due to a finite number of vortices (with piecewise constant vorticity) in the domain $\mathcal{D}$ such that the no-normal flow boundary condition

$$\Psi = 0 \text{ on } \partial\mathcal{D}, \tag{5.1}$$

is satisfied. Further, let $\psi_1$ be the streamfunction owing to the vortices in the absence of boundaries $\partial\mathcal{D}$, which gives

$$\tilde{u}_\theta = -\frac{1}{\sin\theta}\frac{\partial\psi_1}{\partial\phi}, \qquad \tilde{u}_\phi = \frac{\partial\psi_1}{\partial\theta}, \tag{5.2}$$

where $\phi \in [0, 2\pi)$ is the azimuthal angle and $\theta \in [0, \pi]$ is the latitudinal angle and $\tilde{u}_\phi$ and $\tilde{u}_\theta$ are the zonal and latitudinal velocities respectively. Velocities on $\partial \mathcal{D}$ owing to $\psi_1$ are computed using the method of contour dynamics (Dritschel 1988, 1989). Introduce an irrotational flow, with streamfunction $\psi_0$, defined throughout $\mathcal{D}$ such that

$$\Psi = \psi_1 + \psi_0. \tag{5.3}$$

The no-normal-flow condition on the boundary $\partial \mathcal{D}$ requires that

$$d(\psi_1 + \psi_0) = 0, \tag{5.4}$$

and hence from (5.2) the relationship between the irrotational flow field and that induced by the vortices in $\mathcal{D}$ on $\partial D$ is given by

$$\frac{\partial \psi_0}{\partial \theta}d\theta + \frac{\partial \psi_0}{\partial \theta}d\phi = -\left(\frac{\partial \psi_1}{\partial \theta}d\theta + \frac{\partial \psi_1}{\partial \theta}d\phi\right) = -\tilde{u}_\phi d\theta + \tilde{u}_\theta \sin\theta d\phi. \tag{5.5}$$

Introduce the stereographic projection into the complex $z$-plane such that

$$z = \cot\left(\frac{\theta}{2}\right) e^{i\phi}, \tag{5.6}$$

which conformally maps $\partial \mathcal{D}$ to $\partial \mathcal{D}_z$ with the north pole being mapped to $\infty$ and the south pole to the origin of the $z$-plane. Velocities in the projected $z$-plane related to those on the sphere can be obtained by direct differentiation of (5.6) giving

$$u^{(z)} - iv^{(z)} = -\frac{ir(1 + r^2)}{2z}(u_\phi - u_\theta), \tag{5.7}$$

where $r = |z|$. The following two results for a point vortex in the stereographic plane with zero net circulation are useful (Kidambi and Newton 2000)

1. The velocity field induced by a point vortex of strength $\Gamma$ in the stereographic plane is

$$u^{(z)} - iv^{(z)} = \frac{(1+r^2)^2}{4} \left[ -\frac{i}{2\pi} \frac{\Gamma}{z - z_\alpha} \right], \qquad (5.8)$$

where $r = |z|$ and $z_\alpha$ is the position of the point vortex in the stereographic plane.

2. The velocity field felt by the vortex in the stereographic plane is

$$u_\alpha^{(z)} - iv_\alpha^{(z)} = -\frac{i\Gamma}{8\pi}(1 + r_\alpha^2)\bar{z}_\alpha. \qquad (5.9)$$

Importantly, note that in (5.8), only the term in the square brackets is conformally invariant.

The first step in incorporating boundaries in the contour dynamics algorithm is to compute the velocities $\tilde{u}_\phi$ and $\tilde{u}_\theta$ on the boundary $\partial\mathcal{D}$ using a standard contour dynamics algorithm for a sphere (i.e. as if boundaries were not present). A contour dynamics algorithm formulated on the surface of the sphere (appendix A.1) is used to find the equivalent velocities on $\partial\mathcal{D}_z$, $\tilde{u}^{(z)} - i\tilde{u}^{(z)}$. Note that stereographic projection is conformal and so preserves the angle between the velocity vector and the tangent to the boundary: this property being important when constructing an irrotational flow field that when added to $\tilde{u}^{(z)} - i\tilde{v}^{(z)}$ gives zero normal flow on the boundary.

Next, a velocity field $u^{(z)} - iv^{(z)}$ is to be found, such that when added to $\tilde{u}^{(z)} - i\tilde{v}^{(z)}$ the normal component of the resulting velocity field vanishes on $\partial\mathcal{D}_z$ and, by conformality of the stereographic projection, on $\partial\mathcal{D}$. It is required that $u^{(z)} - iv^{(z)}$ is irrotational on the sphere so no extra vorticity is being added to the dynamics.

To determine $u^{(z)} - iv^{(z)}$, $\mathcal{D}_z$ is mapped to the exterior unit circle $\mathcal{D}_\zeta$ in the $\zeta$-plane using the map $\zeta = F(z)$. Importantly, the velocity data $\tilde{u}^{(z)} - i\tilde{v}^{(z)}$ on $\partial\mathcal{D}_z$ is divided by the factor $(1 + r^2)/4$ (see (5.8)) since it is required that the velocity field be conformally invariant under this map. Let the velocity field on $\partial\mathcal{D}_z$ be $\tilde{u}_c^{(z)} - i\tilde{v}_c^{(z)}$ after dividing by this factor. Requiring that the total component of $u_c^{(z)} - iv_c^{(z)}$ and $\tilde{u}_c^{(z)} - i\tilde{v}_c^{(z)}$ normal to $\partial\mathcal{D}_z$ vanishes gives

$$\Im[(u_c^{(z)} - iv_c^{(z)})dz]_{\partial\mathcal{D}_z} = -\Im[(\tilde{u}_c^{(z)} - i\tilde{v}_c^{(z)})dz]_{\partial\mathcal{D}_z}. \tag{5.10}$$

On $\partial\mathcal{D}_\zeta$, $\zeta = e^{i\sigma}$ ($0 \le \sigma < 2\pi$) and noting $dw = (u_c^{(z)} - iv_c^{(z)})dz$, (5.10) can be written as

$$\Im\left[\frac{dw}{d\sigma}\right]_{\partial\mathcal{D}_\zeta} = -\Im\left[\frac{i\zeta}{F'(z)}(\tilde{u}_c^{(z)} - i\tilde{v}_c^{(z)})\right]_{\partial\mathcal{D}_\zeta} = g(\sigma), \tag{5.11}$$

where $g(\sigma)$ is a known function on $\partial\mathcal{D}_\zeta$ and $w$ is the complex potential of the velocity field sought.

Let

$$w = iC\log\zeta + \sum_{k=1}^{\infty} a_k\zeta^{-k} \tag{5.12}$$

where $C \in \mathbb{R}$ and $a_k$ are complex constants. The constant $C$ determines the circulation around the obstacle and is arbitrary. Expressing $g(\sigma)$ as a Fourier series, $a_k$ can be determined efficiently by Fast Fourier Transforms. Thus (5.12) gives

$$u^{(z)} - iv^{(z)} = \frac{(1 + r^2)^2}{4}\frac{dw}{d\zeta}\frac{d\zeta}{dz} = \frac{(1 + r^2)^2}{4}\left[\frac{iC}{\zeta} + \sum_{k=1}^{\infty} -ka_k\zeta^{-k-1}\right]F'(z). \tag{5.13}$$

The velocity correction on the sphere is, using (5.7),

$$u_\phi - iu_\theta = \frac{2iz}{r(1 + r^2)}(u^{(z)} - iv^{(z)}). \tag{5.14}$$

Since $u^{(z)} - iv^{(z)}$ is irrotational in the $z$-plane it is possible to show by direct calculation that $u_\phi - iu_\theta$ given by (5.14) is indeed irrotational on the sphere.

Finally, to advect points on the contour the following three velocity fields are required:

(i) the self-induced velocity owing to the vorticity of the patch (or patches) itself.

(ii) the velocity correction $u_\phi - iu_\theta$ given by (5.14).

(iii) the velocity given by (5.9), where $z_\alpha$ is now $z_i$, the $i$th node of the patch boundary.

To compute (iii) it is necessary to compute $\Gamma = \omega A$ where $A$ is the patch area. This can be done efficiently using boundary data using the boundary integral expression

$$A = \oint_{\partial \mathcal{B}} (1 - z)d\phi, \tag{5.15}$$

where $z = r\cos\theta$ and $\partial \mathcal{B}$ is the patch boundary. Additionally, the patch centroid position given by

$$\mathbf{X} = \frac{\mathbf{T}}{|\mathbf{T}|}, \tag{5.16}$$

where $\mathbf{T} = \oint_{\partial \mathcal{B}} \mathbf{x} \times d\mathbf{x}$, is calculated for later use in comparison of patch trajectories with those of point vortices.

In practice the sum in (5.13) is truncated at some value $N$. Vortex patches in $\mathcal{D}$ are then advected using a fourth order Runge-Kutta method. The procedure presented in this section is then repeated at the beginning of each time step.

## 5.2   Examples

Several examples are now presented for which the dynamics of vortices in singly connected domains on the unit sphere are computed. In the following examples, initially a single finite area vortex $\mathcal{B}$ with piecewise constant vorticity and circulation $\Gamma$ and vortex boundary denoted $\partial\mathcal{B}$ moves in the domain $\mathcal{D}$. In all following computations the time step is set to $dt = 0.01$ and resolution parameter between vortex boundary nodes set to 0.01. Note that no contour surgery was implemented in the following examples.

### 5.2.1   Ellipse in the stereographic plane

The first example considered is that where the domain $\mathcal{D}_z$ is exterior to an ellipse in the stereographic plane such that $\partial\mathcal{D}_z$ is given by

$$\left(\frac{\Re(z)}{a}\right)^2 + \left(\frac{\Im(z)}{b}\right)^2 = 1, \tag{5.17}$$

where $a$ and $b$ are the semimajor and semiminor axis of the ellipse respectively. An illustration of the stereographic projection is given in figure 5.1. The boundary on the sphere, $\partial\mathcal{D}$, is recovered by mapping (5.17) to the sphere via the inverse of the stereographic map (5.6). In general $\partial\mathcal{D}$ is a closed curve centred about the south pole.

The conformal map from the region $\mathcal{D}_z$ to the region exterior to the unit circle $\mathcal{D}_\zeta$ is given by

$$\zeta = \frac{z + (z^2 - a^2 + b^2)^{\frac{1}{2}}}{a + b}, \tag{5.18}$$
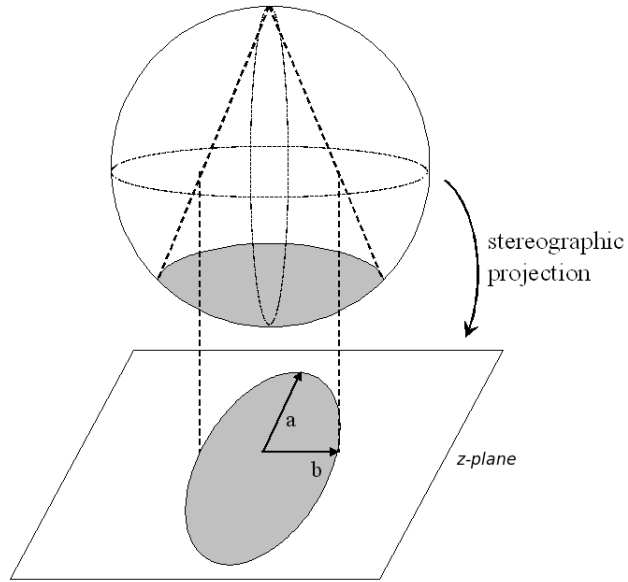
Figure 5.1: Schematic illustraiting the stereographic projection from the sphere to an ellipse in the complex $z$-plane.

with inverse

$$z = \frac{1}{2} \left( (a+b)\zeta + (a-b)\zeta^{-1} \right).$$  (5.19)

To ensure the vortex system on the sphere has zero net circulation the constant $C$ is set to be

$$C = -\frac{\Gamma}{2\pi}.$$  (5.20)

Velocities on $\partial \mathcal{B}$ in $\mathcal{D}$ are then computed as outlined in the previous section. The sum in equation (5.13) is truncated at $N = 400$.

For comparison purposes exact point vortex trajectories in the domain $\mathcal{D}$ in the case where the boundary is an ellipse in the stereographic plane in the absence of a background flow can be derived using the Kirchhoff-Routh path function for point vortices on a sphere (Crowdy 2006) and using the maps (5.19,5.20). The point vortex

trajectories are given by

$$\left| \frac{(1 + z_\alpha \overline{z}_\alpha)}{(\zeta(z_\alpha)\overline{\zeta(z_\alpha)} - 1)} \frac{2\zeta(z_\alpha)^2}{(a-b)\zeta(z_\alpha)^2 - a - b} \right| = \text{const}, \qquad (5.21)$$

where the subscript $\alpha$ indicates the location of the point vortex. Figure 5.2 shows the patch motion about an ellipse with $a = 0.2$ and $b = 0.1$ where patch is initially circular with $\Gamma \approx 0.774$ and vorticity $\omega = 10$ and centroid initially located at $(\phi_{co}, \theta_{co}) = (0, 2/3\pi)$. In this case the motion is contained within the Southern Hemisphere. The boundary in this case is a "short" obstacle where the north pole is an elliptic stationary point as determined by contours of (5.21) and thus the vortex patch dynamics will be more analogous to the motion about an isolated object in the plane and not the "gap in a wall" problem. The patch motion remains close to circular and thus the centroid motion of the vortex patch follows the point vortex trajectory very closely. This orbital motion persists for long times. Figure 5.3 (with $a = 4.0$, $b = 0.0$, $\Gamma \approx -3.075$, $\omega = -10$ and $(\phi_{co}, \theta_{co}) = (0.2\pi, 0.25\pi)$) shows the case for which the ellipse is collapsed so that it is a thin barrier around a portion of a great circle. The boundary in this case is a "long" barrier and is thus analogous to the planar problem of the "gap in a wall" (Johnson and McDonald 2004a). In this case, as the patch passes the edge of the barrier the patch and barrier are within closer proximity than in the case previously considered, thus a far greater degree of distortion of the patch is observed. Figure 5.3 shows that for this case, after the patch passes through the gap, the distortion induced from the interaction with the barrier results in filamentation. The vortex then proceeds in the expected way with a filament growing in time. Such filamentation is also typical in the planar case (Johnson and McDonald 2004a).
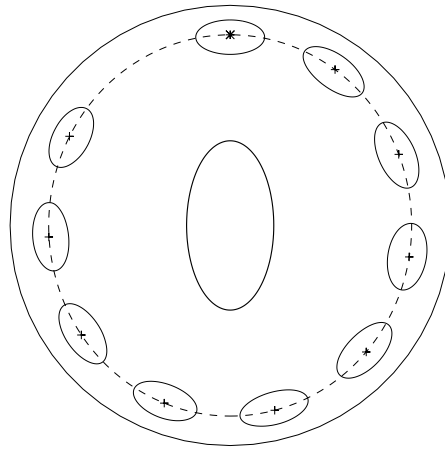
Figure 5.2: Southern Hemisphere view of a vortex patch with $\Gamma \approx 0.774$ and $\omega = 10$. The patch centroid is initially located at $\phi = 0, \theta = \frac{2}{3}\pi$, marked by the asterisk (*). The barrier is an ellipse with $a = 0.2$ and $b = 0.1$ in the stereographic plane. The dashed line represents the exact point vortex trajectory and the $+$ marks the vortex patch centroid location. The vortex patch location is shown in increments of 4 time units up to $t = 40$.
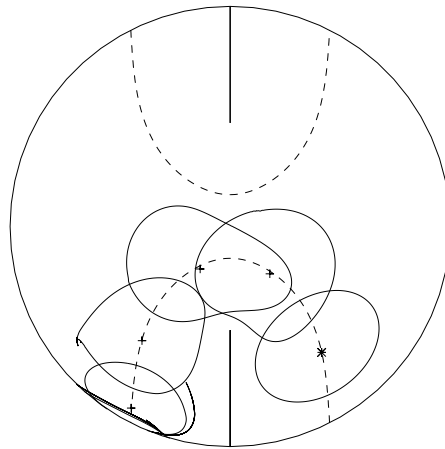


Figure 5.3: View centered at the north pole of a vortex patch with $\Gamma \approx -3.075209$ and $\omega = -10$. The patch centroid is initially located at $\phi = 0.2\pi$ and $\theta = 0.25\pi$, marked by the asterisk (*). The barrier is an ellipse with $a = 4.0$ and $b = 0.0$ in the stereographic plane i.e. a thin barrier. The dashed line represents the exact point vortex trajectory and the $+$ marks the vortex patch centroid location. The patch location is shown in increments of 1 time unit.

## 5.2.2   Thin barriers with background flows

Vortex motion can also be computed in the presence of a compatible background flow whose streamfunction is here denoted $\psi_B$. Compatible flows satisfy

$$\nabla^2 \psi_B = \text{const}, \tag{5.22}$$

so that the vorticity distribution remains piecewise constant, a necessary condition for implementing contour dynamics. The velocity field due to $\psi_B$ is given by

$$U_B - iV_B = \frac{\partial \psi_B}{\partial \theta} + i \frac{1}{\sin\theta} \frac{\partial \psi_B}{\partial \phi}, \tag{5.23}$$

where $U_B$ and $V_B$ are the zonal and meridional velocities respectively. Addition of this velocity field to that owing to $\psi_1$ and $\psi_0$ at the patch boundary $\partial\mathcal{B}$ prior to advection then gives the resultant motion of the patch in the domain $\mathcal{D}$ in the presence of a background flow.

For the case when the ellipse is collapsed to a thin barrier, a possible compatible flow is that due to a dipole located at the south pole with

$$\psi_B = R\cos\left(\phi + \frac{\pi}{2}\right)\cot\left(\frac{\pi - \theta}{2}\right), \tag{5.24}$$

and thus the constant in (5.22) is zero for this flow except at the south pole itself. Streamlines of this flow for a view from the north pole are shown in figure 5.4(a) and from the south pole in figure 5.4(b). $R$ in equation (5.24) is a constant that determines the strength and sense of the background flow. Using (5.23), the velocity field arising from (5.24) is given by

$$U_B - iV_B = \frac{R}{2}\frac{\cos\left(\phi + \frac{\pi}{2}\right)}{\sin^2\left(\frac{\pi - \theta}{2}\right)} - iR\sin\left(\phi + \frac{\pi}{2}\right)\frac{\cot\left(\frac{\pi - \theta}{2}\right)}{\sin\theta}. \tag{5.25}$$
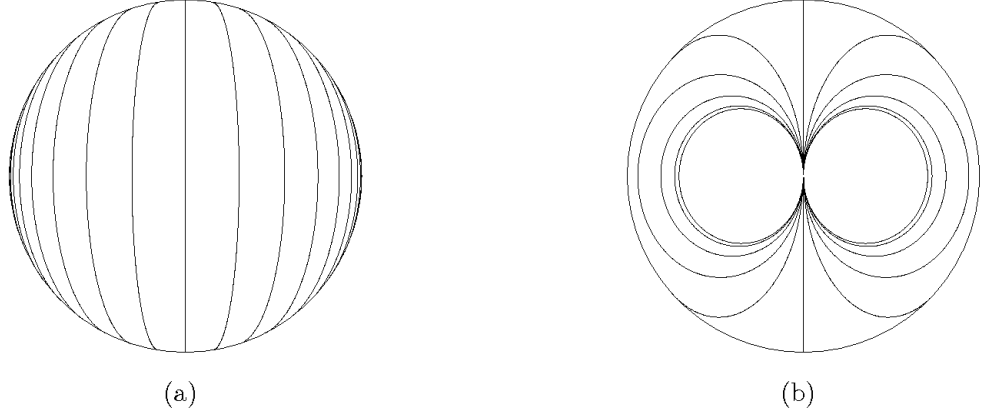
Figure 5.4: Streamlines of the background flow given by $\psi_B = R\cos\left(\phi + \frac{\pi}{2}\right)\cot\left(\frac{\pi-\theta}{2}\right)$ for a view (a) centred about the north pole $(0,0)$ and (b) centred about the south pole $(0,\pi)$.

A straightforward modification of the Kirchhoff-Routh path function for the sphere to account for background flows gives exact point vortex solutions in the presence of $\psi_B$ and in this case takes the form

$$-\frac{\Gamma}{4\pi}\log\left|\frac{(1+z_\alpha\overline{z}_\alpha)}{(\zeta(z_\alpha)\overline{\zeta(z_\alpha)}-1)}\frac{2\zeta(z_\alpha)^2}{a\zeta(z_\alpha)^2-a}\right| + R\cos\left(\phi_\alpha + \frac{\pi}{2}\right)\cot\left(\frac{\pi-\theta_\alpha}{2}\right) = \text{const.}$$

(5.26)

Here $\phi_\alpha$ and $\theta_\alpha$, the position of the point vortex in spherical polar co-ordinates have been maintained for the simplicity of expressing (5.26). Introducing a dipole at the south pole means that at this point fluid is effectively being 'sucked' in one side of the barrier and expelled on the other. Thus if the path of a vortex takes it into the region in which fluid is being 'sucked' into the barrier the vortex will also be sucked in and removed from the system. However, the flow in the vicinity of the gap is parallel to the barrier and hence, in this region at least, is of geophysical interest. Thus for

this system, the period of interest is when the vortex patch interacts with the gap and not the long term dynamics of the system. Note that in the equivalent planar problem the dipole driving uniform flow parallel to the barrier is at infinity.

The first example considered is one in which the patch is initially located in the gap of the barrier and to one side as shown in figure 5.5 ($a = 4.0$, $b = 0.0$, $\Gamma \approx -3.075$, $\omega = -10$, $(\phi_{co}, \theta_{co}) = (0.5\pi, 0.15\pi)$ and $R = 5\Gamma/4\pi$). The background flow is such that it is assisting the motion of the patch towards the barrier edge. Thus as the patch moves towards and about the plate it is 'pinched' against the barrier. This results in part of the patch being pushed to the 'left' of the barrier and part being pushed to its 'right'. (Where 'left' and 'right' are used in the sense of the orientation of figure 5.5.) Following this 'pinching', the flow is assisting the motion of the region of the patch to the left of the barrier and opposing the motion of the patch to its right. The patch is thus effectively split into two separate patches whose motion becomes less coupled as the separation between them increases. Recall that no surgery is implemented in this algorithm and thus the 'patches' remain connected via a thin filament. This results in the right hand patch having insufficient circulation to oppose the background flow and it remains in a quasi-steady state trapped against the barrier.

Another compatible flow for the thin barrier case is that due to two fixed point vortices with circulations $\Gamma_a$ and $\Gamma_b$ placed on the equator such that the line joining the two point vortices is perpendicular to the barrier i.e. the vortices' stereographically projected fixed positions are given by $z_a = i$ and $z_b = -i$ respectively. The stream-function due to a point vortex with circulation $\Gamma$ at the stereographically projected
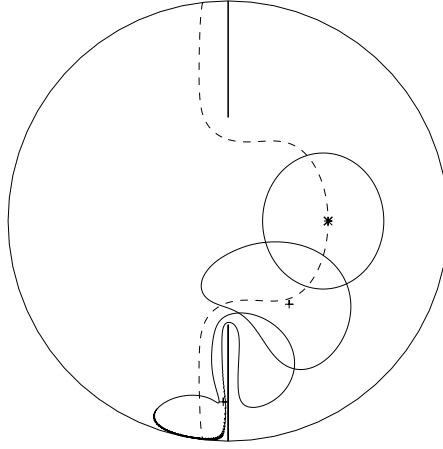
Figure 5.5: View centred at the north pole of a vortex patch with $\Gamma \approx -3.075209$ and $\omega = -10$. The patch centroid is initially located at $\phi = 0.5\pi$ and $\theta = 0.15\pi$, marked by the asterisk (*). The barrier is an ellipse with $a = 4.0$ and $b = 0.0$ in the stereographic plane. A background flow is present with streamfunction $\psi_B$ as in (5.24) with $R = 5\Gamma/4\pi$. The dashed line represents the exact point vortex trajectory given by (5.26) and the $+$ marks the vortex patch centroid location. The patch location is shown in increments of 1 time unit.

position $z_\alpha$ on a sphere is

$$\psi_{\text{pv}}(z, \bar{z}; z_\alpha, \bar{z}_\alpha) = -\frac{\Gamma}{4\pi} \log \left( \frac{(z - z_\alpha)(\bar{z} - \bar{z}_\alpha)}{(1 + z\bar{z})(1 + z_\alpha \bar{z}_\alpha)} \right), \tag{5.27}$$

(see, e.g. Kidambi and Newton 2000). The streamfunction due to two point vortices located at $z_a = i$ and $z_b = -i$ with circulations $\Gamma_a$ and $\Gamma_b$ respectively is thus given by

$$\psi_B = -\frac{\Gamma_a}{4\pi} \log \left( \frac{(z - i)(\bar{z} + i)}{2(1 + z\bar{z})} \right) - \frac{\Gamma_b}{4\pi} \log \left( \frac{(z + i)(\bar{z} - i)}{2(1 + z\bar{z})} \right). \tag{5.28}$$

When $\psi_B = \psi_B(z, \bar{z}; z_\alpha, \bar{z}_\alpha)$, the velocity field (5.23) can be found using

$$U_B - iV_B = \frac{2z}{\sin\theta} \frac{\partial \psi_B}{\partial z}, \tag{5.29}$$

(Crowdy and Cloke 2003), and hence

$$U_B - iV_B = -\frac{\Gamma_a z}{2\pi \sin\theta} \left( \frac{1}{z - i} - \frac{\bar{z}}{1 + z\bar{z}} \right) - \frac{\Gamma_b z}{2\pi \sin\theta} \left( \frac{1}{z + i} - \frac{\bar{z}}{1 + z\bar{z}} \right). \tag{5.30}$$

Exact point vortex trajectories are given by

$$\log \left| \frac{(1 + z_\alpha \bar{z}_\alpha)}{(\zeta(z_\alpha)\overline{\zeta(z_\alpha)} - 1)} \frac{2\zeta(z_\alpha)^2}{a\zeta(z_\alpha)^2 - a} \right| + \frac{\Gamma_a}{\Gamma} \log \left| \frac{(z - i)(\bar{z} + i)}{2(1 + z\bar{z})} \right| + \frac{\Gamma_b}{\Gamma} \log \left| \frac{(z + i)(\bar{z} - i)}{2(1 + z\bar{z})} \right| = \text{const.}$$

(5.31)

Figure 5.6 (with $a = 0.25$, $b = 0.0$, $\Gamma \approx -0.774 = -\Gamma_a = -\Gamma_b$, $\omega = -10$ and $(\phi_{co}, \theta_{co}) = (\pi/2, 3\pi/4)$) shows an example of a system with this background flow in which the thin barrier is short, its projected length in the $z$-plane is 0.5. The fixed point vortices located at $z_a = i$ and $z_b = -i$ are of equal circulation and thus their velocity fields oppose each other at the barrier giving zero net flow along $\phi = 0, \pi$. The circulation of these vortices is also opposite to that of the patch and their combined flow field opposes that due to the patch-barrier interaction. This has the effect of creating stagnation points either side of the plate. Figure 5.6 shows the patch beginning close the stagnation point between the barrier and $z_a = i$. The flow field in this area is very weak and the initial motion of the patch is slow. The flow field induced by the patch-barrier interaction then gradually accelerates the patch and it moves about the barrier entering the region of fluid where the fixed point vortex at $z_b = -i$ dominates the background flow. The patch is thus decelerated as it approaches the stagnation point in this region. The patch motion then reverses due to the effect of the fixed point vortex at $z_b$ and the patch circulates once about $z_b$ before returning to the stagnation point. The process then repeats. Very good agreement is seen between the path of the patch centroid and that of a point vortex except within close proximity to the stagnation points.

In Figure 5.7 ($a = 4.0$, $b = 0.0$, $\Gamma \approx -0.774$, $\omega = -10$, $\Gamma_a = 1.25\Gamma = -\Gamma_b$ and $(\phi_{co}, \theta_{co}) = (0.075\pi, 0.35\pi)$) the fixed vortices have opposite circulation and so
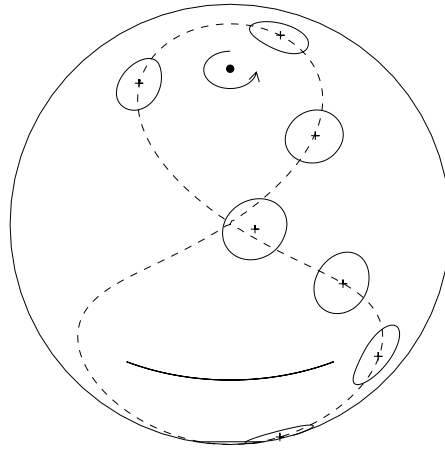
Figure 5.6: View centered at $(3\pi/2, 3\pi/4)$ of a vortex patch with $\Gamma \approx -0.773564$ and $\omega = -10$. The patch centroid is initially located at $\phi = \pi/2$ and $\theta = 3\pi/4$ (i.e. the bottom most centred patch of the figure). The barrier is an ellipse with $a = 0.25$ and $b = 0.0$ in the stereographic plane. A background flow is present with $\psi_B$ as in (5.28) with $\Gamma_a = \Gamma_b = -\Gamma$, the fixed point vortex locations are indicated by solid dots. The dashed line represents the exact point vortex trajectory and the $+$ marks the vortex patch centroid location. The patch location is shown at $t = 0, 15, 20, 22.5, 30, 40, 42.5$ and 45.

reinforce each other along the barrier assisting the initial patch movement towards the gap. The patch initially passes through the gap but the background flow field is sufficient to overcome the patch-barrier interaction effect and advects the patch away from the barrier. The patch then approaches the barriers opposite edge and the resulting patch-barrier interaction results in the patch passing back through the gap and travelling past and down the opposite edge of the barrier (on the same side of the gap as which it begun). The patch's interaction with the barrier results in a deformation of the patch followed by some filamentation. Such trajectories are typical to those seen in the planar case when a uniform background flow parallel to the barrier is present. Johnson and McDonald (2004a) give examples in which a patch initially passes through the gap but the background flow parallel to the barrier is sufficient to overcome the "image" effect and results in the vortex passing back through the gap as seen here in figure 5.7.

### 5.2.3    Longitudinal wedge

In Kidambi and Newton (2000) and example B of Crowdy (2006) an expression for the trajectories of a point vortex in a longitudinal wedge bounded by the longitudes $0$ and $\pi/m$ for $m$ a positive integer in Kidambi and Newton (2000) and for $m$ a positive real number in Crowdy (2006), were derived. Here the vortex patch motion in such a region (with arbitrary) is computed and compared to these trajectories. As in section 5.2.1 the region is stereographically projected into the complex plane and then mapped to the exterior of the unit disk. Here the sum in (5.13) is truncated to $N = 800$ and $C$ is set to zero. A greater value of $N$ is required in this (and the
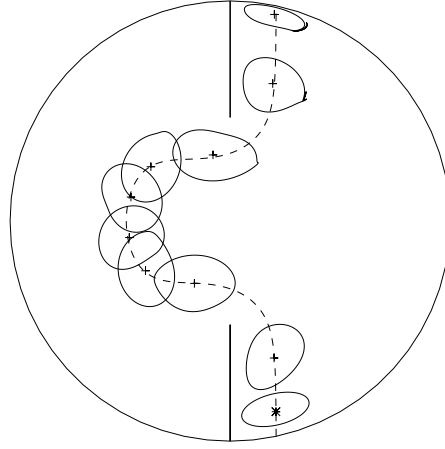
Figure 5.7: The motion of a vortex patch with $\Gamma \approx -0.773564$ and $\omega = -10$. The patch centroid is initially located at $\phi = 0.075\pi$ and $\theta = 0.35\pi$, marked by the asterisk (*). The barrier is an ellipse with $a = 4.0$ and $b = 0.0$ in the stereographic plane. A background flow is present with $\psi_B$ as in (5.28) with $\Gamma_a = 4\Gamma/5 = -\Gamma_b$. The dashed line represents the exact point vortex trajectory and the $+$ marks the vortex patch centroid location. The patch location is shown at $t = 0, 1, 3, 6, 9, 12, 15, 18, 19.5$ and $21$.

following) example to ensure the solution is convergent within the same numerical tolerance as in the previous examples. First note the longitudinal wedge maps to the infinite plane wedge in the stereographic plane. The infinite plane wedge in the $z$-plane is then mapped to the upper half of an intermediate $z_1$-plane using:

$$z_1(z) = z^m. \tag{5.32}$$

The conformal mapping from the upper half of the $z_1$-plane to the exterior of the $\zeta$ unit disk is given by

$$\zeta(z_1) = \frac{1 - iz_1}{1 + iz_1}, \tag{5.33}$$

and the composite of these two maps, the map from the $z$-projection of the infinite wedge to the exterior of the unit $\zeta$ disk is given by

$$\zeta(z) = \frac{1 - iz^m}{1 + iz^m}, \tag{5.34}$$

with inverse

$$z(\zeta) = \left[ i\frac{\zeta - 1}{\zeta + 1} \right]^{\frac{1}{m}}. \tag{5.35}$$

Note that $m$ here is an arbitrary positive real number. Vortex patch motion is then computed according to the procedure detailed in section 5.1. Figure 5.8 shows the motion of a vortex patch in a wedge with $m = 1.7$ (and $\Gamma \approx 0.774$, $\omega = 10$ and $(\phi_{co}, \theta_{co}) = (0.15\pi, \pi/2)$). In this example the patch does not come within close proximity to the wedge corners and remains close to circular. The trajectory of the patch centroid thus follows the exact point vortex trajectory very closely. Figure 5.9 shows the vortex motion within a much wider wedge than the previous example. Here $m = 0.55$ (and $\Gamma \approx 0.774$, $\omega = 10$ and $(\phi_{co}, \theta_{co}) = (0.075\pi, \pi/2)$). This is equivalent to the motion of the patch outside a thin wedge and is approaching the limiting case in which the wedge would become a thin barrier spanning half a great circle. In this example the vortex patch starts within close proximity to the wedge and initially travels down the wall towards the point of the wedge at the south pole. As the patch passes about the south pole it is deformed and some minor filamentation is observed around the patch edges as it travels back along the other side of the wedge. As a result of this the patch centroid begins to deviate slightly away from the exact point vortex trajectory.
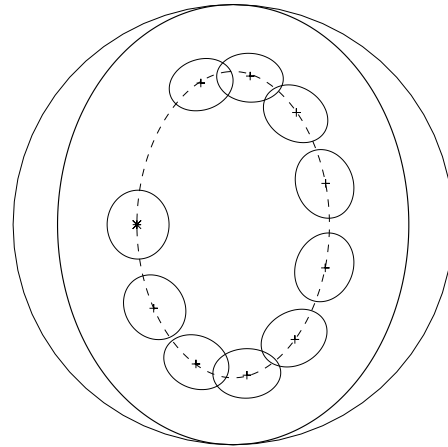
Figure 5.8: Motion of a vortex patch with $\Gamma \approx 0.773564$ and $\omega = 10$ within a wedge with $m = 1.7$. The patch centroid is initially located at $(0.15\pi, \pi/2)$, marked by the asterisk (*). The patch location is shown in increments of 4 time units. The solid line represents the wedge, the dashed line the exact point vortex trajectory and the + marks the patch centroid location.
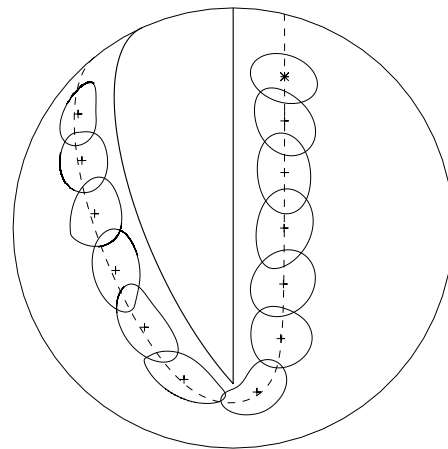


Figure 5.9: Motion of a vortex patch with $\Gamma \approx 0.773564$ and $\omega = 10$ within a wedge with $m = 0.55$. The patch centroid is initially located at $(0.075\pi, \pi/2)$, marked by the asterisk (*). The patch location is shown in increments of 1 time unit. The solid line represents the wedge, the dashed line the exact point vortex trajectory and the + marks the patch centroid location at each time interval.

## 5.2.4   Half-longitudinal wedge

Consider a spherical triangle domain $\mathcal{D}$ containing the south pole and the region bounded by the longitudes $0$ and $\pi/m$ and the equator. Point vortex motion in this geometry was also considered by Kidambi and Newton (2000) ($m \in \mathbb{Z}$) and, more generally, Crowdy (2006) ($m \in \mathbb{R}$). Thus the domain $\mathcal{D}_z$ will be the sector of the unit circle bounded by the lines $\arg(z) = 0$ and $\arg(z) = \pi/m$ and the arc defined by $|z| = 1$. $C$ is set to zero to ensure zero circulation about the half-wedge. Next the sector in the $z$-plane is mapped to the upper half of the intermediate $z_1$-plane using

$$z_1(z) = \left( \frac{1 + z^m}{1 - z^m} \right)^2, \tag{5.36}$$

followed by a map from the upper half of the $z_1$ plane to the exterior of the unit $\zeta$-disk (5.33). The composite of (5.33) and (5.36) gives

$$\zeta(z) = \frac{1 - i \left( \frac{1+z^m}{1-z^m} \right)^2}{1 + i \left( \frac{1+z^m}{1-z^m} \right)^2}, \tag{5.37}$$

with inverse

$$z(\zeta) = \left( \frac{\left[ i \frac{\zeta-1}{\zeta+1} \right]^{\frac{1}{2}} - 1}{\left[ i \frac{\zeta-1}{\zeta+1} \right]^{\frac{1}{2}} + 1} \right)^{\frac{1}{m}}. \tag{5.38}$$

Figure 5.10 gives an example of the motion of a vortex patch within a half-longitudinal wedge with $m = 0.7$ (and $\Gamma \approx 0.774$, $\omega = 10$ and $(\phi_{co}, \theta_{co}) = (0.15\pi, 0.75\pi)$) using $N = 800$. The patch in this case remains close to circular and as expected the motion of centroid matches that of a point vortex very closely.
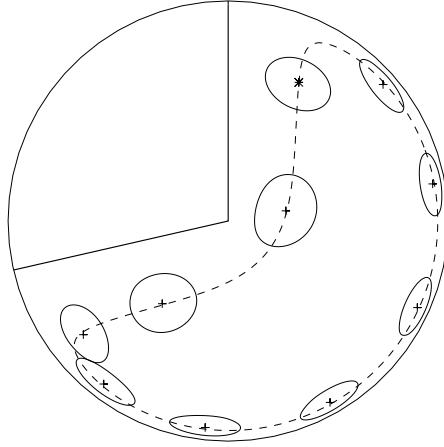
Figure 5.10: Motion of a vortex within a half-longitudinal wedge with $m = 0.7$. The vortex has $\Gamma \approx 0.773564$ and $\omega = 10$. The view is centred on $(0, \pi)$ and the patch location is shown at increments of 4 time units. The initial centroid of the vortex is indicated by the asterisk (*). The solid line represents the wedge boundary, the dashed line the exact point vortex trajectory and the + marks the patch centroid location at each time interval.

## 5.3   A doubly connected domain: Barrier with two gaps

In this section, the techniques of section 5.1 are extended to compute the motion of a vortex in a doubly connected domain $\mathcal{D}$, where the domain considered here is a thin barrier on the surface of the unit sphere with two gaps. Let the barrier lie along the great circle corresponding to $\phi = 0, 2\pi$ (where $\phi \in [0, 2\pi)$ is the azimuthal angle) except at two gaps $\mathcal{G}_1$ and $\mathcal{G}_2$ between $\theta_0^{(\mathcal{G}_1)}$ and $\theta_1^{(\mathcal{G}_1)}$ and between $\theta_0^{(\mathcal{G}_2)}$ and $\theta_1^{(\mathcal{G}_2)}$ respectively (where $\theta \in [0, \pi]$ is the latitudinal angle). The stereographic projection into the complex $z$-plane given in (5.6) maps $\mathcal{D}$ to $\mathcal{D}_z$. The barrier is projected to the line $\Im z = 0$ with gaps lying between $z_0^{(\mathcal{G}_1)}$ and $z_1^{(\mathcal{G}_1)}$ and between $z_0^{(\mathcal{G}_2)}$ and $z_1^{(\mathcal{G}_2)}$. Following Johnson and McDonald (2005) the domain is further decomposed into two

subdomains $\mathcal{D}_{1,2}$, with $\mathcal{D}_1$ denoting the upper half of the stereographically projected $z$-plane ($\Im z > 0$) and $\mathcal{D}_2$ the lower half. Let the streamfunction induced by the vortices in the region $\mathcal{D}_1$ satisfying the no-normal flow condition along $\Im z = 0$ be $\psi_1$ so that

$$\psi_1 = 0, \ \text{ on } \Im z = 0. \tag{5.39}$$

Similarly, let the streamfunction induced by the vortices in the region $\mathcal{D}_2$ satisfying the no-normal flow boundary condition on $\Im z = 0$ be $\psi_2$, so

$$\psi_2 = 0, \ \text{ on } \Im z = 0. \tag{5.40}$$

Denote the total streamfunction induced by all vortices in $\mathcal{D} = \mathcal{D}_1 \cup \mathcal{D}_2$ by $\Psi$ and introduce an irrotational flow field with streamfunction $\psi_0$ such that

$$\Psi = \begin{cases} \psi_1 + \psi_0 \text{ in } \mathcal{D}_1, \\[2mm] \psi_2 + \psi_0 \text{ in } \mathcal{D}_2. \end{cases} \tag{5.41}$$

Thus $\Psi$ is continuous across the gaps and $\psi_{1,2}$ vanish there, so $\psi_0$ is continuous across the gaps. The streamfunction $\psi_1$ is therefore that of a vortex distribution in $\mathcal{D}_1$ with a rigid wall along $\Im z = 0$ (or around the great circle corresponding to $\phi = 0, 2\pi$ on the unit sphere), and correspondingly, $\psi_2$ is the streamfunction owing to a vortex distribution in $\mathcal{D}_2$ with a rigid wall along $\Im z = 0$.

Velocity fields owing to $\psi_1$ and $\psi_2$ can then be directly computed on the surface of the sphere using a spherical contour dynamics algorithm. The velocity field owing to $\psi_1$ is that due to the vorticity distribution in $\mathcal{D}_1$, computed using a standard spherical contour dynamics algorithm (i.e. as if boundaries were not present), along with that due to its image in the 'rigid wall'. The velocity field due this image vorticity is again

computed using a standard spherical contour dynamics algorithm. The velocity field owing to $\psi_2$ is computed analogously for the distribution of vorticity within $\mathcal{D}_2$. The velocity fields in $\mathcal{D}_1$ and $\mathcal{D}_2$, owing to $\psi_1$ and $\psi_2$ respectively, are thus known and it remains to determine the streamfunction $\psi_0$. Once $\psi_0$ has been determined, $\Psi$ is known everywhere, solving the original problem.

In the stereographic $z$-plane, let the normal pointing from $\mathcal{D}_1$ to $\mathcal{D}_2$ be $\mathbf{n}_{12}$. The normal derivative of the streamfunction, $\partial \Psi^{(z)}/\partial n_{12}$ (where the superscript denotes the quantity in the stereographic plane) is continuous across the gaps. The jump in the quantity $\Psi^{(z)} - \psi_0^{(z)}$ in moving from $\mathcal{D}_1$ to $\mathcal{D}_2$ is given by

$$\left[ \frac{\partial}{\partial n_{12}} (\Psi^{(z)} - \psi_0^{(z)}) \right] = \frac{\partial \psi_2^{(z)}}{\partial n_{12}} - \frac{\partial \psi_1^{(z)}}{\partial n_{12}}. \tag{5.42}$$

(Note that here and in the remainder of this section, the notation $[.]$ is taken to mean the jump in the enclosed quantity in moving from $\mathcal{D}_1$ to $\mathcal{D}_2$). Therefore, the jump in $\psi_0^{(z)}$ across the gap must be given by

$$\left[ \frac{\partial \psi_0^{(z)}}{\partial n_{12}} \right] = -\frac{\partial \psi_2^{(z)}}{\partial n_{12}} + \frac{\partial \psi_1^{(z)}}{\partial n_{12}} = u_2^{(z)} - u_1^{(z)}, \tag{5.43}$$

where $u_2^{(z)}$ is the tangential velocity induced at a gap owing to $\psi_2^{(z)}$ and $u_1^{(z)}$ the tangential velocity at a gap owing to $\psi_1^{(z)}$. The velocity fields at the gaps on the unit sphere owing to $\psi_1$ and $\psi_2$ are computed as outlined above. Following the method detailed in section 5.1, these velocities are projected into the stereographic $z$-plane giving the required $u_1^{(z)}$ and $u_2^{(z)}$.

The around island vortex-induced circulations are evaluated according to

$$\Gamma_V^{(m)} = \int_{z_0^{(m)}}^{z_1^{(m)}} [u_V] |dz|, \tag{5.44}$$
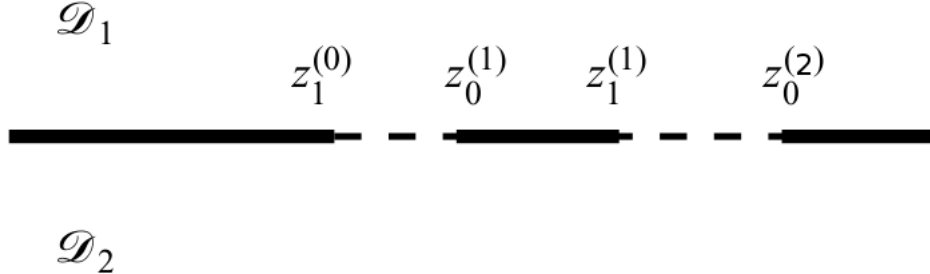
Figure 5.11: Stereographic projection of the collinear gaps and the islands of zero thickness. The island covering the north pole has edges $z_1^{(0)}$ and $z_0^{(2)}$ and the edges of the island placed within this islands 'gap' are labelled $z_0^{(1)}$ and $z_1^{(1)}$.

where the superscript $m$ denotes the island edges, as shown in figure 5.11, and $[u_V]$ is the jump in the $z$-plane tangential velocity across the island. The jump in tangential velocity is again calculated by computing velocities at the islands owing to $\psi_1$ and $\psi_2$ on the unit sphere using a standard spherical contour dynamics algorithm and then projecting these velocities into the stereographic $z$-plane. Denote the complex potential associated with $\psi_0$ by $w_0(z)$, and extend the complex velocity $u_0^{(z)} - iv_0^{(z)} = dw_0/dz$, analytic in the upper half-plane to the lower half-plane by

$$\frac{dw_0}{dz}(z) = -\overline{\frac{dw_0}{dz}}(\bar{z}), \qquad \Im z < 0. \tag{5.45}$$

The jump in tangential velocity across $\Im z = 0$ is therefore $2u_0$ and the condition on the tangential velocity of the irrotational flow can be written as

$$\Re\{dw_0\}/|dz| = \Re\{(u_0^{(z)} - iv_0^{(z)})dz\}/|dz| = u_0^{(z)} = -\frac{1}{2}[u_V], \qquad \text{on} \qquad \Im z = 0. \tag{5.46}$$

From (5.45) the horizontal velocity is odd about the imaginary axis and therefore the vortex-induced around island circulations, from (5.44) and (5.46), become

$$\Gamma_V^{(m)} = -2\int_{z_0^{(m)}}^{z_1^{(m)}} u_0^{(z)}|dz| = -2\Re\{w_0(z_1^{(m)}) - w_0(z_0^{(m)})\}. \tag{5.47}$$

Denote the through gap volume fluxes $\alpha_m$ $(m = 1, 2)$, given by the change in $\Im w_0$ across a gap. Using the around island circulation conditions of (5.44), the through-gap volume fluxes are determined as

$$\alpha_m = \Im\{w_0(z_0^{(m)}) - w_0(z_1^{(m-1)})\}. \tag{5.48}$$

To solve the harmonic problem and determine $w_0$, the problem is now mapped from the stereographically projected $z$-plane into a periodic rectangle, here denoted the $\tau$-plane. Fist, consider the case when the gaps are collinear with $\mathcal{G}_1$ located between $(\pi, \pi/2)$ and $(\pi, \theta_1)$ and $\mathcal{G}_2$ located between $(0, \pi/2)$ and $(0, \theta_1)$ where $\theta_1 \in (\pi/2, \pi)$ such that there is a gap between $|\Re z| < 1$ in the stereographic plane with the intervening 'island' centred about the south pole corresponding to $|\Re z| < k$ where $k = \cot(\theta_1/2)$ (giving $0 < k < 1$). As will be shown later, this configuration can then be mapped to the problem of two arbitrary placed gaps.

The map

$$\tau = \text{sn}^{-1}(z/k), \tag{5.49}$$

with inverse

$$z = k\text{sn}\tau, \tag{5.50}$$

and

$$\frac{d\tau}{dz} = \frac{1}{\sqrt{(k^2 - z^2)(1 - z^2)}}, \tag{5.51}$$

where sn denotes the elliptic function of modulus $k$, conformally maps the half-plane $\Im z > 0$ to the rectangle $-K < \Re\tau < K$, $0 < \Im\tau < K'$ in the $\tau$-plane, where

$$K(k) = \int_0^1 [(1 - t^2)(1 - k^2 t^2)]^{-1/2} dt, \quad K'(k) = K\sqrt{1 - k^2}. \tag{5.52}$$

(a)

| A | $\mathscr{D}_1$ | B | H | G | E | | F |
|---|---|---|---|---|---|---|---|
| C | $\mathscr{D}_2$ | $-1$ | $-k$ | $k$ | $1$ | | D |

(b)

$-K + iK'$ ............ $K + iK'$ ............ $3K + iK'$

| B | A, F | E | D, C | B |
|---|---|---|---|---|
| | $\mathscr{D}_1$ | | $\mathscr{D}_2$ | |
| H | | G | | H |

$-K$ ............ $K$ ............ $3K$
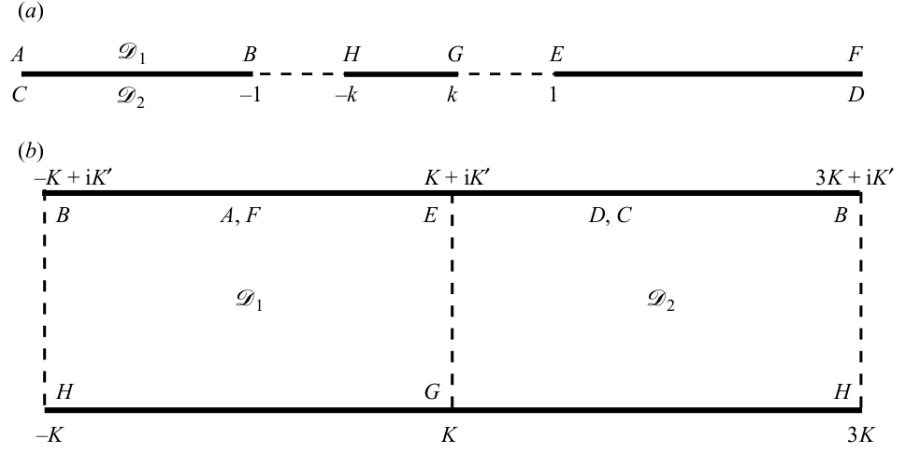
Figure 5.12: (a) Symmetric gaps in the $z$-plane with semi-infinite domains $\mathcal{D}_1$ and $\mathcal{D}_2$ in $\Im z > 0$ and $\Im z < 0$ respectively. (b) The periodic rectangle in the $\tau$-plane onto which the $z$-plane is mapped. The points A-H in figure (a) are mapped to their corresponding letters in figure (b).

Note that here, and in the rest of this section the prime does not denote the derivative.

An illustration of this mapping is given in figure 5.12. By reflecting the $\tau$-plane about $\Re\tau = K$, (5.49) is extended to cover the entire $z$-plane. Thus one real period of the $\tau$-plane rectangle, where $-K < \Re\tau < 3K$, corresponds to the entire $z$-plane. However, to determine $w_0$ it is sufficient to consider the rectangle $-K < \Re\tau < 3K$. The two points located at $z = \pm\infty$ now coincide at $\tau = iK'$ and thus the line $\Im\tau = K'$ corresponds to the barrier spanning half the great circle and $\Im\tau = 0$ to the small island centred about the South Pole.

In the $\tau$-plane, the velocity condition (5.46) becomes

$$\Re\{dw_0\}/|d\tau| = -\frac{1}{2}[u_V]|dz/d\tau| \quad \text{on} \quad \Re\tau = \pm K, \quad 0 < \Im\tau < K', \tag{5.53}$$

and (5.48), the through gap flux conditions, become

$$\Im w_0 = \alpha_1 = \alpha \quad \text{on} \quad \Im \tau = 0, \quad |\Re \tau| < K,$$

$$(5.54)$$

$$\Im w_0 = \alpha_2 = 0 \quad \text{on} \quad \Im \tau = K', \quad |\Re \tau| < K.$$

This condition is satisfied by a uniform stream in the $\Re \tau$-direction such that the tangential velocity condition (5.53) is not effected. Thus

$$w_0 = \alpha(K' - \tau)/K' + w_{00}, \tag{5.55}$$

where $w_{00}$ is the complex potential of an irrotational flow. A suitable expression for $w_{00}$ can be obtained through a further mapping of the $\tau$-plane rectangle to the upper half of an annulus $\delta_1 < |\sigma| < \delta_2$ in the complex $\sigma$-plane. This mapping is given by

$$\sigma = \exp(\pi \tau / K'), \tag{5.56}$$

such that

$$\delta_{2,1} = \exp(\pm \pi K / K'). \tag{5.57}$$

The complex potential $w_{00}$ then satisfies

$$\Im w_{00} = 0 \quad \text{on} \quad \phi = 0, \pi, \quad \delta_1 < |\sigma| < \delta_2,$$

$$(5.58)$$

$$\Re\{dw_{00}\}/|d\sigma| = -\frac{1}{2}[u_V]|dz/d\sigma| \quad \text{on} \quad |\sigma| = \delta_{1,2}, \quad 0 < \phi < \pi,$$

where $\phi = \arg \sigma$. Within the annulus $w_{00}$ is harmonic and can thus be written as

$$w_{00} = \sum{}' a_n \sigma^n, \tag{5.59}$$

where $n \in \mathbb{Z}$ and the prime indicates that the $n = 0$ term is omitted. Along with the $n = 0$ term the allowable $\log \sigma$ term is also omitted from (5.59). Both these

terms have been absorbed into the constant $\alpha$ in (5.55) and are thus absent in (5.59). Further, since $w_{00}$ can be extended in to the lower half of the $\sigma$-plane through

$$w_{00}(\bar{\sigma}) = \overline{w_{00}(\sigma)}, \tag{5.60}$$

the $a_n$ in (5.59) can be taken as real. On the $\sigma$-domain boundaries, $|\sigma| = \delta_{1,2}$, $d\sigma/|d\sigma| = ie^{i\phi}$ and thus (5.58) gives

$$\Re\{dw_{00}\}/|d\sigma| = \sum {}' n a_n \Re\{\sigma^{n-1} i e^{i\phi}\} = \sum_1^\infty b_n^{(1,2)} \sin n\phi, \tag{5.61}$$

where

$$b_n^{(1,2)} = -\frac{n}{\delta_{1,2}} (a_n \delta_{1,2}^n + \delta_{-n} \delta_{1,2}^{-n}), \qquad n \in \mathbb{Z}^+. \tag{5.62}$$

The $b_n^{(1,2)}$ are the Fourier Sine coefficients in the expansion of $-\frac{1}{2}[u_V]|dz/d\sigma|$ on $|\sigma| = \delta_{1,2}$, $0 < \phi < \pi$ and are given explicitly by

$$b_n^{(1,2)} = -\frac{K'}{2\pi^2 \delta_{1,2}} \int_0^\pi [u_V] \left( (k^2 - z_{1,2}^2)(1 - z_{1,2}^2) \right)^{\frac{1}{2}} \sin(n\phi) d\phi, \tag{5.63}$$

where, using the mappings (5.50) and (5.56)

$$z_{2,1} = k \mathrm{sn} \left[ \frac{K'}{\pi} \log \sigma \right] = k \mathrm{sn} \left[ \pm K + i K' \frac{\phi}{\pi} \right], \tag{5.64}$$

which correspond to purely real points lying within the gaps. The coefficients $b_n$ can now be determined numerically using discrete fast Fourier transforms evaluating the integral in (5.63) at points spaced evenly in $\phi$. The coefficients $a_n$ in (5.59) are given by

$$a_n = \frac{\delta_2 b_{|n|}^{(2)} \delta_1^{-n} - \delta_1 b_{|n|}^{(1)} \delta_2^{-n}}{|n|(\delta_1^n \delta_2^{-n} - \delta_2^n \delta_1^{-n})}, \qquad n = \pm 1, \pm 2, \pm 3, ... \tag{5.65}$$

Finally, to determine the velocity field owing to $w_0$ in the stereographic $z$-plane the through-gap volume flux $\alpha$ must be determined. The island edges, given ny $z = \pm k$

in the $z$-plane, correspond to $\tau = \pm K$ and $\sigma = \delta_{1,2}$ giving

$$\Re\{w_0|_{z=k} - w_0|_{z=-k}\} = -2\alpha\frac{K}{K'} + \sum{}' a_n(\delta_2^n - \delta_1^n), \tag{5.66}$$

where, again, $n \in \mathbb{Z}$ and the prime indicates that the $n = 0$ term is omitted. Thus, (5.66) along with (5.47) and (5.48) give the through-gap volume flux

$$\alpha = \frac{K'}{2K}\left[\frac{1}{2}\Gamma_V + \sum_1^{\infty}\frac{\delta_1 b_n^{(1)} + \delta_2 b_n^{(2)}}{2}\right]. \tag{5.67}$$

Using (5.55), (5.59), (5.65) and (5.3) the complex potential of the required irrotational velocity field $w_0$ is hence determined. The irrotational velocity field owing to $w_0$ in the $z$-plane is then given by

$$u_0^{(z)} - iv_0^{(z)} = \frac{dw_0}{d\sigma}\frac{d\sigma}{d\tau}\frac{d\tau}{dz} = \frac{\pi}{K'}\left[\frac{\alpha\sigma/K' + \sum{}' n a_n \sigma^n}{((k^2 - z^2)(1 - z^2))^{\frac{1}{2}}}\right], \tag{5.68}$$

where $\sigma = \exp[(\pi/K')\mathrm{sn}^{-1}(z/k)]$. These velocities are then projected back to the sphere and added to those owing to $\psi_1$ and $\psi_2$ to give the total velocity field on the surface of the sphere. Importantly, in this case the image of the vortex patch has been explicitly included when determining the velocity fields owing to $\psi_1$ and $\psi_2$. Thus the difference here to the examples previously considered is that when projecting velocities back to the sphere the velocity field arising due to the Gauss constraint (see (5.9)) is not added back on to the total velocity field. Points on the vortex contour are then advected as detailed in section 5.1.

## 5.3.1   Background flows

Note that in the formulation presented above, the circulation around the island is not necessarily zero, the circulation around the thin barrier extending to $\infty$ in the

$z$-plane will however be zero. Due to the topography of the sphere and the fact that it is an enclosed surface an additional term is required to ensure net zero circulation. In planar problems a vortex can initially be positioned at 'infinity' such that the fluid surrounding the island is initially stagnant i.e. there is initially no circulation about the island and owing to Kelvin's Circulation theorem this will remain so for all time. However, when considering the problems on the surface of the sphere such an assumption cannot be made. Thus to ensure a net zero circulation around the island in the spherical case it is required to place a point vortex of circulation $-\Gamma$ in the $\tau = \mathrm{sn}^{-1}(z/k)$ plane such that it maps to the centre of the island (i.e. the South Pole in the symmetric gap case) in the $z$-plane. Label this point $\tau_\infty$. Using equation (3.6) of Johnson and McDonald (2005), the background complex potential required to ensure zero circulation about the island is given by

$$w_B = \frac{-\Gamma}{2\pi i} \log \left( \frac{\theta_1[\pi(\tau - \tau_\infty)/4K]}{\theta_1[\pi(\tau - \tau'_\infty)/4K]} \right),  \qquad (5.69)$$

where $\tau'_\infty$ is the reflection of $\tau_\infty$ about the line $\tau = iK'$ i.e. $\tau'_\infty = \tau_\infty + 2(iK' - \Im\tau_\infty)$. The Hamiltonian associated with such background flows, required for the computation of point vortex trajectories, is then given by

$$H_B(\tau, \tau_\infty) = -\Gamma\Im[w_B].  \qquad (5.70)$$

Of course, this form of the complex potential is not restricted to imposing the net zero circulation case and can be used to impose an additional circulation around an object or a background flow due to fixed point vortices such as was done for a singly connected case in section 5.2.2. The velocity field owing to such a background flow

in the $z$-plane is given by

$$u_B^{(z)} - iv_B^{(z)} = \frac{dw_B}{d\tau}\frac{d\tau}{dz}. \tag{5.71}$$

Such velocity fields are added to (5.68) before projecting back to the sphere.

## 5.3.2 Point vortex trajectories

The vortex Hamiltonian for the planar analog of this problem is derived in Johnson and McDonald (2005). The relationship between a Hamiltonian on the sphere $H^s$ to a Hamiltonian in the complex $z$-plane $H^z$ is given by (Surana and Crowdy 2008)

$$H^s(\{\phi_{\alpha_i}\}, \{\theta_{\alpha_i}\}) = H^z(\{z_{\alpha_i}\}) + \frac{1}{4\pi}\sum_{j=1}^{N}\Gamma_j^2 \log \frac{1}{(1 + z(\alpha_j)\bar{z}(\alpha_j))}, \tag{5.72}$$

where $\alpha_i$ denotes the position of the $i$th vortex in a pre-image $\zeta$ domain. For the case of a single point vortex with circulation $\Gamma_1 = \Gamma$ located at $z = z_{\alpha_1}$ and when the two gaps in the barrier are collinear with $\mathcal{G}_1$ located between $(\pi, \pi/2)$ and $(\pi, \theta_1)$ and $\mathcal{G}_2$ located between $(0, \pi/2)$ and $(0, \theta_1)$ where $\theta_1 \in (\pi/2, \pi)$ such that the resulting island centred about the south pole corresponds to $|\Re z| < k$ where $k = \cot(\theta_1/2)$, the vortex Hamiltonian is given by

$$H^s(z, \bar{z}) = (\Gamma^2/4\pi)\log|(k^2 - z^2)^{1/2}(1 - z^2)^{1/2}\vartheta_1[i\pi(\Im\mathrm{sn}^{-1}(z/k) - K')/2K]|$$

$$\tag{5.73}$$

$$+ (\Gamma^2/4\pi)\log|1/(1 + z\bar{z})| - \Gamma\Im[w_B],$$

where $w_B$ is given in (5.69) and here $\tau_\infty = 0$. Vortex trajectories (and also finite area vortex motion) for the case when the island lies asymmetrically between the barrier spanning half a great circle can be deduced through mapping to the symmetric case. An island in the sterographically projected $\hat{z}$-plane located between $x_0 < \Im\hat{z} < x_1$

(with $-1 < x_0 < x_1 < 1$) within a gap corresponding to $-1 < \Im \hat{z} < 1$ is mapped back to the symmetric problem in the $z$-plane via the Mobius map given by

$$z = (-\alpha \hat{z} + 1)/(\hat{z} - \alpha), \tag{5.74}$$

leaving the gap of width of 2 unchanged but moving the island to lie along $|\Re z| \leq k < 1$ where

$$\alpha = \exp(\cosh^{-1}[(x_0 x_1 + 1)/(x_0 + x_1)]), \ \ k = \exp(\cosh^{-1}[(x_0 x_1 - 1)/(x_0 - x_1)]). \tag{5.75}$$

This mapping along with the transformation

$$H^{\hat{z}}(\{\hat{z}_\alpha\}) = H^z(\{z_\alpha\}) + (\Gamma^2/4\pi) \log |d\hat{z}/dz|_{\hat{z}_\alpha}, \tag{5.76}$$

and equation (5.73) give the appropriate vortex Hamiltonian in the $\hat{z}$-plane. Finally, it is simplest to obtain the vortex Hamiltonian for the case when $\mathcal{G}_1$ and $\mathcal{G}_2$ are located at arbitrary locations on the barrier by considering one of the islands to be centred about the north pole and the other to be located arbitrarily along the same great circle and then mapping to the case of two collinear gaps and applying the appropriate transformation to the Hamiltonian (5.72). This corresponds to the configuration in the $\mathcal{D}_{\tilde{z}}$ domain where the gap is located between $-r < \tilde{z} < r$ ($r \in \mathbb{R}^+$) with the island, whose edges are here denoted $\tilde{z}^{(\mathcal{L}_1)}$ and $\tilde{z}^{(\mathcal{L}_2)}$, contained within the gap such that $-r < \tilde{z}^{(\mathcal{L}_1)} < \tilde{z}^{(\mathcal{L}_2)} < r$. The map taking the $\tilde{z}$-plane to the $\hat{z}$ plane considered above is simply the contraction

$$\hat{z} = \frac{\tilde{z}}{r}. \tag{5.77}$$

The domain $\mathcal{D}_{\hat{z}}$ is then mapped to the domain $\mathcal{D}_z$ such that the gaps are now collinear using (5.74). Through a standard rotation on the surface of the sphere, the two islands can be placed such that they lie along arbitrary sections of a great circle.
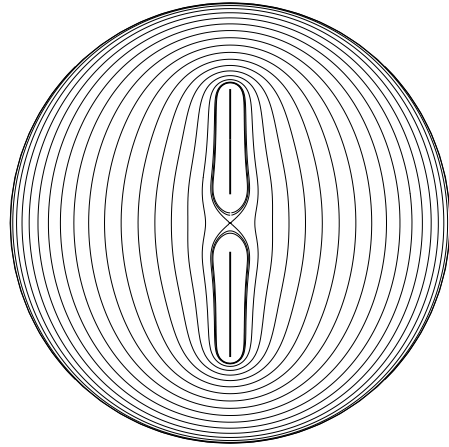
Figure 5.13: Point vortex trajectories for the case when both barriers span $\pi/12$ of a great circle and their centres are seperated by $\pi/4$.

Figures 5.13 shows the point vortex trajectories when each island spans $\pi/12$ of a great circle with the island centres separated by $\pi/4$. A hyperbolic point is placed symmetrically between the two islands through which the separatrix passes, separating the trajectories which orbit one island or the other, or both islands. Away from the islands, the trajectories begin to resemble those of the thin barrier seen in sections 5.2.1 and 5.2.2. In figure 5.14 trajectories are shown for the case when the gap is located between $|\tilde{z}| < 3/4$ and the island is located between $-1/5 < \tilde{z}^{(\mathcal{L}_1)} < \tilde{z}^{(\mathcal{L}_2)} < 1/2$. The effect of the island is to introduce elliptic points to either side of it, that is, if the island was not present there would exist a single elliptic point located at the South Pole. This indicates the possibility of steady vortex structures residing to either side of the island. Away from the island vortex trajectories resemble those of the single gap case.
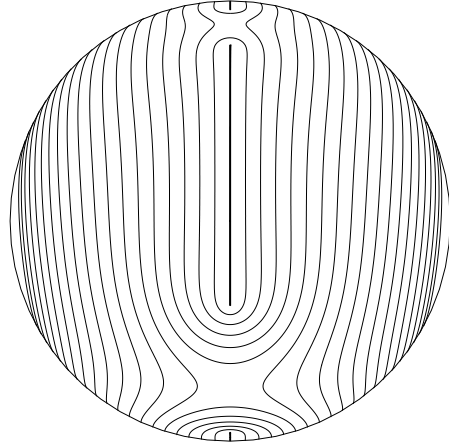
Figure 5.14: Point vortex trajectories for the case when the gap is located between $|\tilde{z}| < 3/4$ and the island is located between $-1/5 < \tilde{z}^{(\mathcal{L}_1)} < \tilde{z}^{(\mathcal{L}_2)} < 1/2$.

### 5.3.3   Vortex patch motion

Computations of vortex patch motion were carried out using a time step of $dt = 0.01$ and resolution parameter between boundary nodes set to 0.01. As noted in section 5.3, the coefficients $a_n$ of (5.65) are evaluated using discrete fast Fourier transforms evaluating the integral in (5.63) at points spaced evenly in $\phi$. Thus, along with using the spherical contour dynamics algorithm to calculate the required velocities at the nodes defining the patch boundary, tangential velocities are calculated at $N_I$ nodes spaced evenly along the island in the stereographically projected plane and at $N_G$ discrete points in the $z$-plane given by

$$z_m^{(1,2)} = k\mathrm{sn}\left[\pm K + \frac{imK'}{\pi N_G}\right] \qquad (m = 1, .., N_G). \qquad (5.78)$$

For the following examples both $N_I$ and $N_G$ were set to 200. Note that no surgery is implemented in the following examples. Also, in the following to examples the circulation about the island is not set to zero, i.e. the velocity field owing to (5.69)
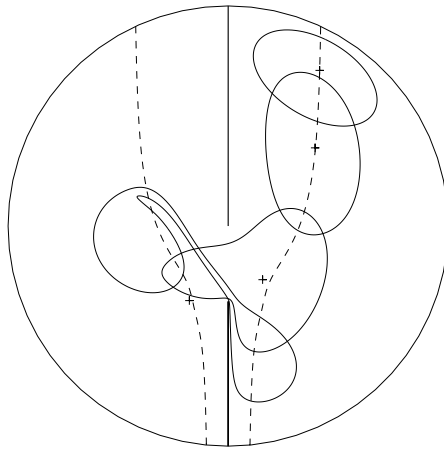
Figure 5.15: View centered at $(\phi, \theta) = (0, 0)$ of the motion of a vortex patch with $\Gamma = 1.5376$ and $\omega = 5$ with its centroid initially located at $(\phi_{co}, \theta_{co}) = (\pi/4, \pi/5)$. One barrier spans half a great circle and the island is placed symmetrically within the barrier such that $|\Re z| \leq 0.7$. The dashed line represents the exact point vortex trajectory and the $+$ marks the patch centroid location. The patch is shown at times $t = 0, 2, 4$ and $6$.

is not included. Figures 5.15 and 5.16 give examples of patch motion about a symmetrically placed and an asymmetrically placed island respectively. In figure 5.15 the through gap flux forces the patch close to the island and it is 'pinched' against the island edge. Up until the point where the patch is distorted by its interaction with the topography, as expected, the patch centroid follows the point vortex very closely. After being squeezed against the island edge, part of the patch passes through the gap whilst part does not. The through gap volume flux induced by the vortex then results in the vortex being 'torn apart'. Such motion is typical in the planar case when the patch is pinched against an edge of the island (Johnson and McDonald 2005). In figure 5.16 the patch remains relatively undistorted and thus the motion of its centroid follows that of a point vortex very closely.
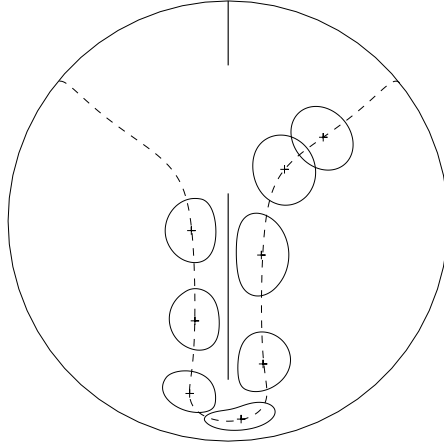
Figure 5.16: View centered at $(\phi, \theta) = (0, 3\pi/4)$ of the motion of a vortex patch with $\Gamma = 0.3867$ and $\omega = 5$ with its centroid initially located at $(\phi_{co}, \theta_{co}) = (\pi/6, 3\pi/5)$. One barrier spans half a great circle and the island is placed asymmetrically within the barrier such that $-0.1 \leq \Re \hat{z} \leq 0.7$. The dashed line and $+$ have the same meanings as in (a). The patch is position is shown in increments of 5 time units.

## 5.4   Vortex Equilibria in a gap

In this section the numerical method described in section 5.1 is used to compute vortex equilibria on a sphere in the presence of boundaries, in particular the case of a thin barrier. The Hamiltonian for a point vortex on a sphere in the presence of a thin barrier can have, depending on the length of the barrier, an elliptic stationary point at the centre of the gap (Crowdy 2006). This is in contrast to the planar case, where the stationary point at the centre of the gap is always hyperbolic (Johnson and McDonald 2004a). An elliptic stationary point is of significance since it suggests the possibility of constructing stable vortex patch equilibria (McDonald 2008). Such stable equilibria may be of interest geophysically since they persist for long times.

The thin barrier is positioned as in section 5.2. That is, a degenerate ellipse centred at the origin of the stereographic $z$-plane with semiminor axis $b = 0.0$, so that the gap

is centred about the north pole. For the north pole to be an elliptic stationary point of the point vortex Hamiltonian it is required that the semimajor axis $a \leq \sqrt{2}$ (Crowdy 2006). An initial 'guess' of the vortex patch shape is an ellipse in the stereographic plane laying symmetrically over the north pole. The patch boundary is discretized into $M$ nodes with co-ordinates $(\phi_i, \theta_i)$ for $i = 1, .., M$ where $\phi_i$ is discretized evenly between 0 and $2\pi$. The corresponding initial $\theta_i$ is given by

$$\theta_i = 2\tan^{-1}\left[\frac{a_p b_p}{a_p^2 \sin\phi_i + b_p^2 \cos\phi_i}\right], \tag{5.79}$$

where $a_p, b_p$ are set constants that initially determine the shape and area of the patch. Note that $a_p$ and $b_p$ are the semimajor and semiminor axes of an ellipse in the stereographic plane given by

$$z_p = \tan\left(\frac{\theta}{2}\right)e^{i\phi}. \tag{5.80}$$

Note that here $|z_p| = \tan(\theta/2)$ (not $\cot(\theta/2)$ as in equation (5.6)) as it is desirable to centre the patch at the origin in the stereographic plane. Also, note that $a_p$ must then be less than $1/a$ where $a$ is the semi major axis of the projected $z$-plane thin barrier. For this initial vortex shape the velocities on the boundary are computed using the method outlined in section 5.1, thus enabling the computation of the streamfunction $\psi_p(\phi_i, \theta_i)$ upon it. At $(\phi_1, \theta_1)$ the streamfunction is set so that $\psi_p(\phi_1, \theta_1) = 0$. The streamfunction is then evaluated at other nodes upon the boundary according to

$$\psi_p(\phi_{i+1}, \theta_{i+1}) \approx \psi_p(\phi_i, \theta_i) + u_{\theta_{i+\frac{1}{2}}}\sin(\theta_{i+\frac{1}{2}})\Delta\phi_i - u_{\phi_{i+\frac{1}{2}}}\Delta\theta_i, \tag{5.81}$$

where the subscript $i + \frac{1}{2}$ indicates the quantity has been averaged between its values at the nodes $i$ and $i + 1$. The iterative numerical method of Pierrehumbert (1980), adapted for the surface of a sphere, is then used to find an equilibrium state. This

involves fixing the position of nodes 1 and $M/2 + 1$ and holding $\phi$ constant at all other nodes whilst iterating their $\theta$ location until the boundary becomes a streamline. Owing to the symmetry of the problem, here only the nodes 1 to $M/2 + 1$ are considered, the location of remaining nodes, $M/2 + 2$ to $M$, are obtained through reflection of the boundary about the gap, i.e. $\theta_{M/2+2} = \theta_{M/2}$ and so forth. Figure 5.17 shows the initial set-up of the patch and nodes. Fixing $\phi_i$ and varying $\theta_i^T$ by $\delta\theta_i$, where the superscript $T$ has been introduced to indicate $T$th iteration of $\theta_i$, the streamfunction varies as

$$\psi_p(\phi_i, \theta_i^T + \delta\theta_i) \approx \psi_p(\phi_i, \theta_i^T) - u_{\phi_i}\delta\theta_i, \tag{5.82}$$

and thus the new $\theta_i$ location $\theta_i^{T+1}$ is given by

$$\theta_i^{T+1} = \theta_i^T + k\frac{\psi_p(\phi_i, \theta_i^T)}{u_{\phi_i}}, \tag{5.83}$$

where $k$ is a relaxation parameter introduced to ensure numerical convergence (Pierrehumbert 1980). Following each iteration the area $A$ and hence circulation of the vortex patch is recalculated using (5.15). The Gauss constraint on the surface of the sphere (i.e $\int\int \omega_s dS = 0$) is embedded in the equations of contour dynamics. Thus when the area of the vortex patch changes, here the vorticity jump, $\tilde{\omega}$, is kept constant and the vorticity of the patch, $\omega$, must be modified appropriately. Following each iteration the patch vorticity and circulation is given by

$$\omega = \frac{\tilde{\omega}}{4\pi}(4\pi - A), \tag{5.84}$$

and

$$\Gamma = \omega A. \tag{5.85}$$

Once the streamfunction becomes constant on the boundary of the patch (to within some numerical tolerance) a steady solution is realized. The patch area and circulation computed at each iteration are also monitored for convergence. For the results reported here vortex patches initially had $\omega = 1$, a resolution of 0.01 between adjacent nodes on the patch boundary was used and the number of nodes on the barrier was set to $N = 400$. The relaxation parameter was set to $k = 0.6$. The fixed boundary nodes were set as

$$(\phi_1, \theta_1) = \left( \frac{\pi}{2}, 2 \tan^{-1} \left[ \frac{a_p b_p}{a_p^2 \sin \pi/2 + b_p^2 \cos \pi/2} \right] \right) \tag{5.86}$$

and

$$(\phi_{M/2+1}, \theta_{M/2+1}) = \left( \frac{3\pi}{2}, 2 \tan^{-1} \left[ \frac{a_p b_p}{a_p^2 \sin 3\pi/2 + b_p^2 \cos 3\pi/2} \right] \right). \tag{5.87}$$

Convergence was generally realized within 50 iterations. Figures 5.18(a) and 5.18(b) show the family of vortex equilibria for the case where the gap-width $a = 1.0$ in the stereographic $z$-plane and on the sphere respectively. The patches were initially set with $a_p = 0.2$ in all cases and $b_p = 0.2, 0.4, 0.6, 1.0, 1.4$ and $2.0$ then iterated to the steady states observed in the figures. Figures 5.19(a) and 5.19(b) show the family of equilibria when $a = 1.4$ for the same initial patch configurations as figures 5.18(a) and 5.18(b).

The robustness of the computed equilibria was examined by using them as initial conditions in a time-dependent simulation using the algorithm detailed in section 5.1. Since there are inevitably small numerical errors inherent in the algorithm, unstable equilibria would be expected to diverge from their steady position within time, whereas stable equilibria would be expected to remain close to their equilibrium
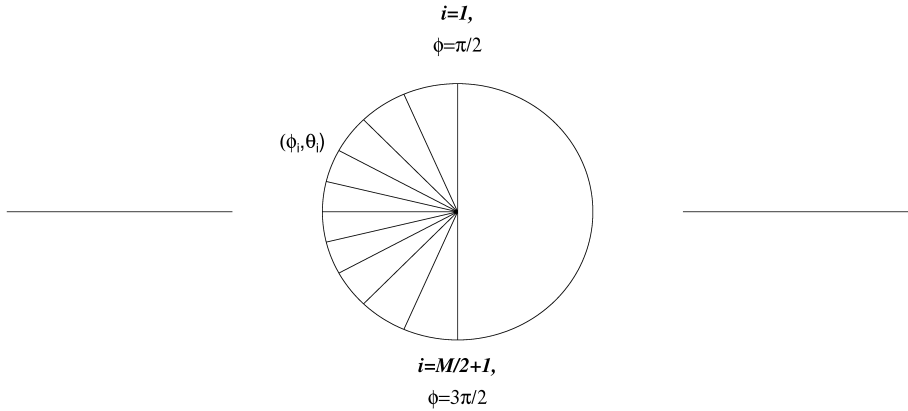
Figure 5.17: Schematic of initial patch setup between the thin barrier in the stereographic plane. The position of the fixed nodes, $i = 1$, and $i = M/2 + 1$ are indicated in the diagram.

position. Although this test does not prove stability/instability of the computed equilibria it gives an extremely good indication of their properties.

For smaller equilibria ($b_p \leq 0.6$) no significant deviation could be observed for times up to $t = 400$. Small oscillations about the equilibrium position were observed for larger equilibria for $t > 200$. Figure 5.20 shows the time evolution of a system with $a = 1.0$ and $\theta_{1,M/2+1} = 0.156\pi$. For this system, at $t = 100$ the deviation of the patch can not be seen by the naked eye. Equilibria were also computed for the case when the Hamiltonian has a hyperbolic point, $a \geq \sqrt{2}$. In contrast, when the robustness of these equilibria were tested and it was seen that generally the configuration would remain relatively steady up to $t \approx 25$, depending on the size of the patch, but afterwards small deviations from the steady state would rapidly grow and the patch moves away from its equilibrium position. Figure 5.21 shows the time evolution of a system with
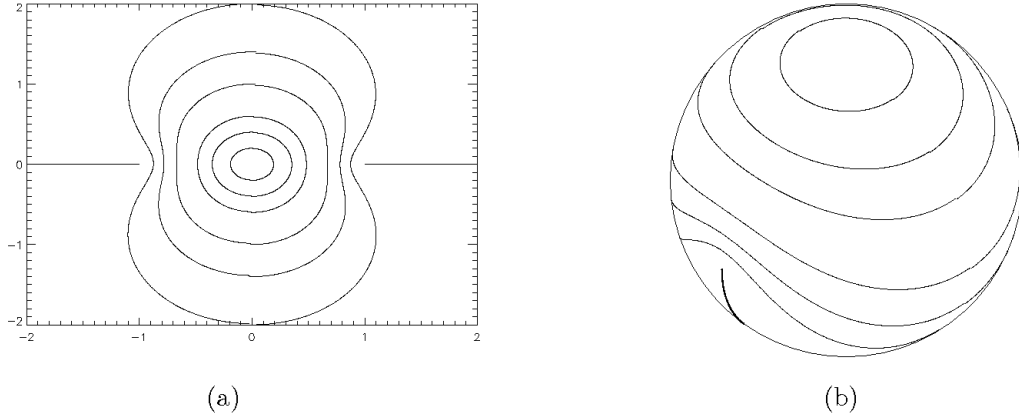
Figure 5.18: Vortex equilibria shapes in (a) the stereographic $z$-plane and (b) on the surface of the sphere, for $a = 1.0$ with initial $b_p = 0.2, 0.4, 0.6, 1.0, 1.4, 2.0$ and initial $a_p = 0.2$ in all cases.

$a = 2.41429$ and $\theta_{1,M/2+1} = 0.430\pi$. The patch considered in this computation is quite large with corresponding large velocities and once a small deviation away from the equilibrium occurs the system quickly diverges from the equilibrium. Thus the time-dependent computations lead to the expected conclusion that equilibria are stable for point vortex equilibria corresponding to the elliptic point of the Hamiltonian and unstable for point vortex equilibria corresponding to the hyperbolic point of the Hamiltonian.
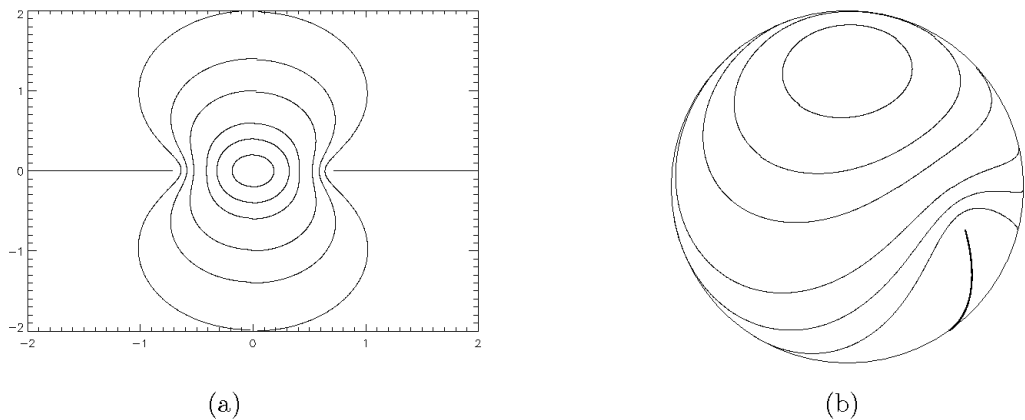
Figure 5.19: Vortex equilibria shapes in (a) the stereographic $z$-plane and (b) on the surface of the sphere, for $a = 1.4$ with initial $b_p = 0.2, 0.4, 0.6, 1.0, 1.4, 2.0$ and initial $a_p=0.2$ in all cases. Note that increasing $a$ results in a smaller gap c.f. (5.79) and (5.80).
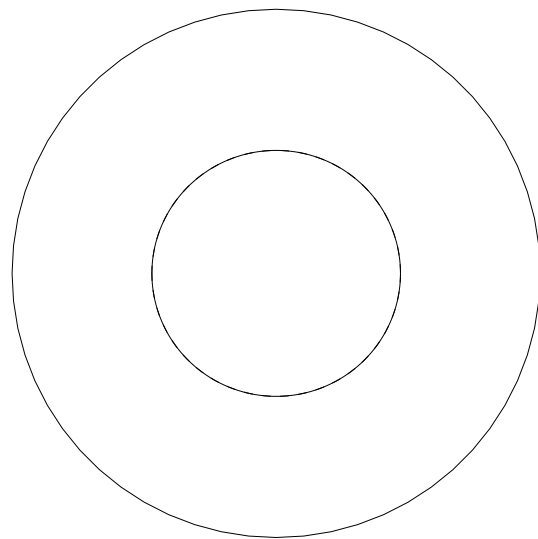
Figure 5.20: View centered at the North Pole of time evolution of the system with $a = 1.0$ and $\theta_{1,M/2+1} = 0.156\pi$. The solid line represents the initial vortex position and the dashed line the vortex position at $t = 100$. In this case, the patch position at $t = 100$ virtually overlays that of the patch at $t = 0$ and thus the dashed line cannot be seen with the naked eye.
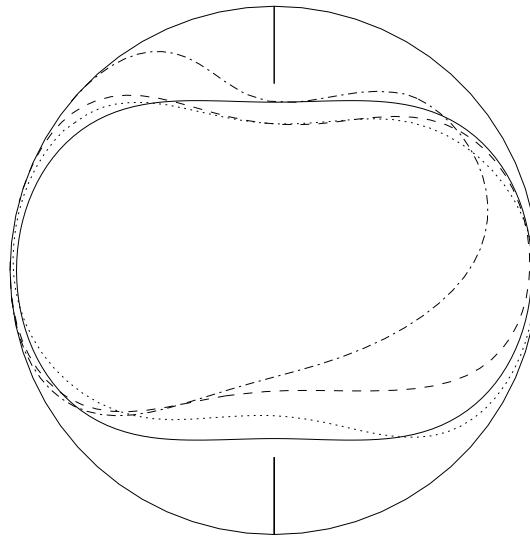
Figure 5.21: Time evolution of the system with $a = 2.41429$ and $\theta_{1,M/2+1} = 0.430\pi$. The thin solid line represents the initial vortex position, the dotted line its position at $t = 10$, the dashed line its position at $t = 20$ and the dot-dash line its position at $t = 23$. The slightly thicker solid line represents the barrier.

## 5.5   Conclusion

Vortex patch motion on the surface of the unit sphere in the presence of impenetrable boundaries has been numerically computed. The procedure first involves using the method of contour dynamics (Dritschel 1989), computing velocities on the sphere as if the boundaries were not present. An irrotational flow field which when added to the vortex induced velocities satisfies the no normal flow condition on the boundary is then computed by projecting the problem into the stereographic plane, mapping the problem to the exterior of the unit disk or to an annulus in the doubly connected case and solving the corresponding harmonic problem to find the complex potential of the irrotational flow. The irrotational flow field is thus known in the stereographic plane and then mapped back to the surface of the sphere. Addition of this flow field

to that given by the contour dynamics algorithm in the absence of boundaries gives the appropriate flow field for the boundaries being present and hence the resulting vortex patch motion on the surface of the sphere can be computed.

Singly-connected domains considered here included an ellipse in the projected $z$-plane, a longitudinal wedge and a half-longitudinal wedge. Patch trajectories about a thin barrier with a gap were computed with and without the presence of a background flow. Background flows caused by a dipole fixed in the centre of the barrier and for point vortices fixed at the equator were considered.

In cases in which the patch remained close to circular the path of the patch centroid followed that of the corresponding point vortex trajectory very closely even with the presence of a background flow. When the path of the centroid travelled within close proximity to the barrier's edge, deformation of the patch occurred often resulting in filamentation. Despite this, centroid paths still showed good agreement with exact point vortex solutions. Exceptions to this can be found when a background flow parallel to a "long barrier" in the vicinity of the gap is present, where a sufficiently strong background flow could result in a patch being "squeezed" against the barriers edge resulting in the vortex splitting. Such splitting occasionally resulted in a quasi-steady vortex being "trapped" against the barrier's edge.

Patch centroid motion in domains including the longitudinal and half-longitudinal wedge again demonstrated very good agreement with the corresponding point vortex motion. Minor filamentation could be observed in such domains in cases in which the patch is deformed when passing around an edge of the wedge or when the patch travels within close proximity of the boundary for some time, resulting from the shear

flow due to the "image" vorticity and the curvature of the sphere.

The doubly connected case of a thin barrier with two gaps was also considered. Good agreement is again seen between the motion of point vortices and patches which undergo little distortion. Behaviour typical to that seen in the planar case is seen resulting from the through gap fluxes generated by the vortex. New features, such as elliptic points of the Hamiltonian residing to either side of the island, are also observed.

This method can also be applied to other doubly connected domains, indeed, the method can in principle be applied to any domain for which a conformal mapping to an annulus exists. It is also in principle possible to apply the method to domains of higher connectivity by mapping to the unit disk with smaller circular disks excised and solving the corresponding Dirichlet problem to obtain the appropriate irrotational flow.

Vortex equilibria lying between the gap in the case of a "short barrier" were then computed. It was shown that a family of equilibria exist for each gap width. Such equilibria were shown to be stable by examining their robustness in a time-dependent code. Such stable equilibria do not exist in the corresponding planar case as the point vortex equilibrium midway between the gap corresponds to a hyperbolic point of the Hamiltonian for all gap widths.

# Chapter 6

# Vortex motion in periodic domains with impenetrable boundaries

Methods described in chapter 5 can also be adapted to compute the motion of finite area vortices in singly periodic domains with boundaries i.e. vortex motion on the surface of an infinite circular cylinder. The motion of vortices in periodic domains is of interest from both an atmospheric and oceanic perspective, for example, the Southern Ocean is an example of a periodic channel. Thus a periodic domain with boundaries, such as that later considered in section 6.3, could be thought of as a 'crude' model of the Southern Ocean. The steps presented here for computing the motion of vortices in periodic domains with boundaries are similar to those presented in chapter 5.1, the main difference being that the unbounded cylindrical contour dynamics algorithm described in appendix A is now used to compute the velocity field on the boundary. Similar to the previous chapter, an irrotational velocity field is sought such that, when added to the velocity field owing to the 'unbounded' vortex

178

generated flow, satisfies the no-normal flow condition on the boundary. The required irrotational flow is obtained through mapping the harmonic problem from the cylinder to a domain exterior to the unit circle and solving the resulting harmonic problem in this simpler domain. In this chapter, two examples will be considered. First, the case of a horizontal thin island in a periodic domain and second, a vertical semi-infinite barrier. In both cases numerically computed finite area patch motion will be compared to exact point vortex trajectories.

## 6.1   Problem formulation

The system consists of a shallow layer of constant depth, incompressible and inviscid fluid in a simply connected domain $\mathcal{D}$ on the surface of the unit cylinder (that is a $2\pi$-periodic domain). Let $\Psi$ denote the total streamfunction due to a finite number of vortices (with piecewise constant vorticity) in the domain $\mathcal{D}$ such that the no-normal flow boundary condition

$$\Psi = 0 \text{ on } \partial\mathcal{D}, \tag{6.1}$$

is satisfied. Further, let $\psi_1$ be the streamfunction owing to the vortices in the absence of boundaries $\partial\mathcal{D}$, which gives

$$\frac{d\hat{\phi}}{dt} = -\frac{\partial\psi_1}{\partial\hat{z}}, \qquad \frac{d\hat{z}}{dt} = \frac{\partial\psi_1}{\partial\hat{\phi}}, \tag{6.2}$$

where $\hat{\phi} \in [0, 2\pi]$ is the azimuthal angle and $\hat{z}$ is the vertical coordinate. Velocities on $\partial\mathcal{D}$ owing to $\psi_1$ are computed using an unbounded cylindrical contour dynamics algorithm (Dritschel 1989, and Appendix A.2). Now, introduce an irrotational flow,

with streamfunction $\psi_0$, defined throughout $\mathcal{D}$ such that

$$\Psi = \psi_1 + \psi_0. \tag{6.3}$$

The no-normal-flow condition on the boundary $\partial \mathcal{D}$ requires that

$$d(\psi_1 + \psi_0)|_{\partial \mathcal{D}} = 0. \tag{6.4}$$

Now, for ease of notation, let the azimuthal and vertical velocity fields owing to $\psi_1$ and $\psi_0$ be written as $(\tilde{u}_0, \tilde{v}_0)$ and $(u_0, v_0)$ respectively. Also, denote the periodic domain $\mathcal{D}_z$ in which the complex coordinate $z = \hat{\phi} + i\hat{z}$. Requiring that the total normal component of the velocity field owing to $\psi_1 + \psi_0$ vanishes on $\partial \mathcal{D}$ gives the relation

$$\Im[(u_0 - iv_0)dz]_{\partial \mathcal{D}_z} = -\Im[(\tilde{u}_0 - i\tilde{v}_0)dz]_{\partial \mathcal{D}_z}. \tag{6.5}$$

The steps in determining $(u_0, v_0)$ now mirror those detailed in chapter 5.1. On the unit circle in the $\zeta$-plane ($\zeta = \exp(i\sigma)$, $0 \leq \sigma < 2\pi$), noting that $dw = (u_\phi - iv_z)dz$, (6.5) can be written as

$$\Im \left[ \frac{dw}{d\sigma} \right]_{\partial \mathcal{D}_\zeta} = -\Im \left[ \frac{i\zeta}{F'(z)}(u_0 - iv_0) \right]_{\partial \mathcal{D}_\zeta} = g(\sigma), \tag{6.6}$$

where $g(\sigma)$ is a known function on $\partial \mathcal{D}_\zeta$, $w$ is the complex potential associated with the streamfunction $\psi_0$ and $F(z)$ is the mapping from $\mathcal{D}_z$ to the domain exterior to the unit circle $\mathcal{D}_\zeta$. Similar to chapter 5.1, the complex potential $w$ can again be written as (5.12), that is

$$w = iC \log \zeta + \sum_{k=1}^{\infty} a_k \zeta^{-k} \tag{6.7}$$

where $C \in \mathbb{R}$ and determines the circulation around the boundary $\partial \mathcal{D}_z$ and the $a_k$ are complex constants. Expressing $g(\sigma)$ as a Fourier series, $a_k$ can be determined

efficiently by Fast Fourier Transforms. The velocity field owing to $\psi_0$ in $\mathcal{D}$ is thus given by

$$u_0 - iv_0 = \left[ \frac{iC}{\zeta} + \sum_{k=1}^{\infty} -ka_k \zeta^{-k-1} \right] F'(z). \tag{6.8}$$

To advect the vortex in the periodic domain, (6.8) is added to the velocity field owing to $\psi_1$ (calculated using an unbounded cylindrical contour dynamics algorithm at discrete points on the contour defining the vortex patch) and time integration is carried out using a fourth order Runge-Kutta method. Nodes on the patch boundary are redistributed at the beginning of each time-step and the procedure presented above repeated. In practice, the sum in (6.8) is truncated at some $k = N$.

## 6.2   Periodic thin islands

Consider a horizontal thin island of length $r$ centred at the middle of a periodic domain of period $L$. The series of mappings given by

$$\zeta_1(\zeta) = \frac{r_I}{2} \left( \frac{1}{\zeta} + \zeta \right), \tag{6.9}$$

$$\zeta_2(\zeta_1) = \frac{i\zeta_1 - 1}{i\zeta_1 + 1}, \tag{6.10}$$

$$z(\zeta_2) = \frac{L}{2\pi i} \log \zeta_2, \tag{6.11}$$

where $r_I$ is related implicitly to $r$ through

$$r = L \left[ 1 - \frac{1}{\pi} \tan^{-1} \left( \frac{2r_I}{r_I^2 - 1} \right) \right], \tag{6.12}$$

maps the exterior of the unit $\zeta$-circle to the periodic $z$-domain exterior to a horizontal thin island of length $r$ centred in the periodic domain. It is useful to note that when $r_I = 1$, $r = L/2$ i.e. the thin barrier spans exactly half of the periodic domain. Also, as $r_I \to \infty$, $r \to L$, that is, the case of a period array of vortices above an infinite solid wall is recovered. The first of these maps, (6.9), takes the exterior of the unit $\zeta_2$-circle to the exterior of a thin island between $-r_I \leq \zeta_1 \leq r_I$. The second map takes this thin island to an arc on the unit circle between $\phi < \arg \zeta_2 < 2\pi - \phi$ where

$$\phi = \tan^{-1}\left(\frac{2r_I}{r_I^2 - 1}\right),\tag{6.13}$$

and finally, (6.11) takes this arc to a horizontal thin island between $(L - r)/2 < z < (L + r)/2$ in the periodic strip. The branch cut in (6.11) is taken to be along the positive real axis in $\mathcal{D}_{\zeta_2}$. The composition of these three maps can be written as

$$z(\zeta) = \frac{L}{2\pi i} \log\left(\frac{ir_I(1 + \zeta^2) - 2\zeta}{ir_I(1 + \zeta^2) + 2\zeta}\right).\tag{6.14}$$

Thus, the derivative of the map required for computing vortex patch trajectories is given by

$$z_\zeta = \frac{1}{F'(z)} = \frac{L}{2\pi i}\left[\frac{2ir_I\zeta - 2}{ir_I(1 + \zeta^2) - 2\zeta} - \frac{2ir_I\zeta + 2}{ir_I(1 + \zeta^2) + 2\zeta}\right]\tag{6.15}$$

Point vortex trajectories in the periodic $z$-domain are derived by considering the vortex Hamiltonian in the unit circle and performing the appropriate transformation. For the mapping into the periodic domain the standard transformation rule for the Hamiltonian can be used as all the information about the images of vortices in the periodic domain are encoded in the transform. This can be verified by mapping the problem of a single vortex within the unit disk to a row of periodic vortices located near a horizontal barrier. It can be shown that the velocity field at a vortex obtained

through the mapping is identical to that of the double vortex street considered in Acheson (1990). The vortex Hamiltonian for a single vortex at position $\alpha$ in the unit circle $\rho$-domain is given by

$$H^{(\rho)}(\alpha, \bar{\alpha}) = \frac{\Gamma^2}{4\pi} \log(1 - \alpha\bar{\alpha}). \tag{6.16}$$

The map from the interior of the unit circle to the periodic $z$-domain exterior to a horizontal thin island is also given by (6.14) (with $\rho$ now replacing $\zeta$) and thus the derivative required in the transformation (5.76) is given by (6.15) (with $\rho$ again replacing $\zeta$). Additionally, the map (6.11) has two logarithmic singularities within the unit $\zeta$-circle located at

$$\rho = \pm \frac{i}{r_I} \left( \sqrt{1 + r_I^2} - 1 \right) = \pm is. \tag{6.17}$$

Inserting (6.17) into (6.11) shows that these two points map to $\Im z = \pm\infty$ in $\mathcal{D}_z$. For the case when the circulation about the island in the domain $\mathcal{D}_z$ is zero it is therefore necessary to impose an additional background flow by placing two point vortices, each of circulation $-\Gamma/2$, at the points $\rho = \pm is$. The complex potential associated a point vortex of unit circulation located at $\eta_0$ in the upper-half $\eta = x + iy$ plane is given by

$$W(\eta) = -\frac{i}{2\pi} \log \left[ \frac{\eta - \eta_0}{\eta - \bar{\eta}_0} \right]. \tag{6.18}$$

This, along with the map from the interior of the unit circle to the upper half $\eta$-plane given by

$$\eta = i \frac{1 - \rho}{1 + \rho}, \tag{6.19}$$

results in a contribution to the Hamiltonian for the background flow due to vortices of strength $-\Gamma/2$ and $\Gamma/2$ at $\rho = \pm is$ given by

$$\Psi(\alpha, \bar{\alpha}) = \Gamma \Im W = \frac{\Gamma^2}{4\pi} \log \left| \frac{\alpha^2 + s^2}{1 + \alpha^2 s^2} \right|. \tag{6.20}$$

Using (6.16), (6.20) and (5.76) the $z$-plane Hamiltonian is therefore given by

$$H^{(z)}(z_\alpha, \bar{z}_\alpha) = H^{(\rho)}(\alpha, \bar{\alpha}) + \Psi(\alpha, \bar{\alpha}) + \frac{\Gamma^2}{4\pi} \log |z_\rho(\alpha)|, \qquad (6.21)$$

where $z_\rho$ is given by replacing $\zeta$ with $\rho$ in (6.15).

Point vortex trajectories for cases when $r_I = 0.5$ and $r_I = 2.0$ are shown in figures 6.1 and 6.2 respectively. $L = 2\pi$ in both cases. Vortices initially located close to the plate orbit the plate in a closed trajectory. Vortices further away from the plate propagate around the cylinder (cross the periodic domain) whilst oscillating up and down. As the length of the plate increases the oscillation of the vortices decreases.

For each of these possible behaviours, a corresponding vortex patch trajectory is shown in figure 6.3 ($r_I = 0.5$, $r = 1.855$) and 6.4 ($r_I = 2.0$, $r = 4.429$). In both contour dynamics computations, $C = 0$ and the sum in (6.8) is truncated at $k = N = 400$. The resolution parameter between patch boundary nodes is set to 0.005 and $dt = 0.01$. In both simulations the patch remains close to circular and thus the patch centroid follows the point vortex trajectory extremely well. Only cases in which $L = 2\pi$ have been shown here as this is the natural case for an algorithm formed on the surface of the unit cylinder. Cases with different periodicities could equally be considered by 'stretching' the domain into one of a different period as was done for the periodic configurations of chapter 3.

## 6.3   Periodic semi-infinite vertical barriers

Another example of a periodic domain is that of a 'picket' fence of semi-infinite pickets. This may be thought of as a crude model of the Southern Ocean in which the
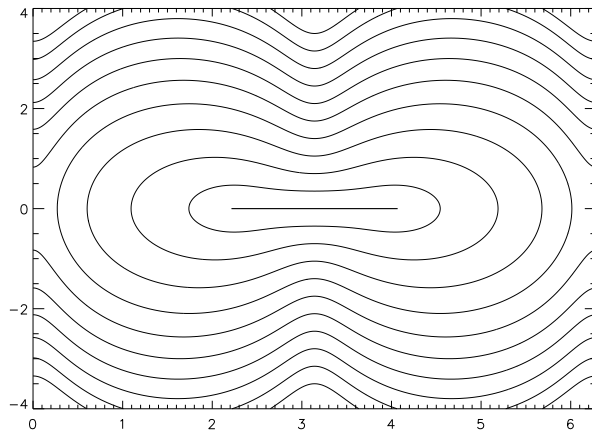
Figure 6.1: Point vortex trajectories in a $2\pi$ periodic domain containing a horizontal thin island. Here, $r_I = 0.5$ and $r = 1.855$.
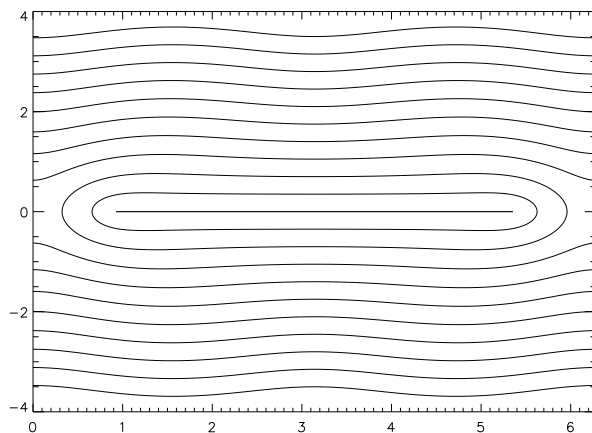


Figure 6.2: Point vortex trajectories in a $2\pi$ periodic domain containing a horizontal thin island. Here, $r_I = 2.0$ and $r = 4.429$.
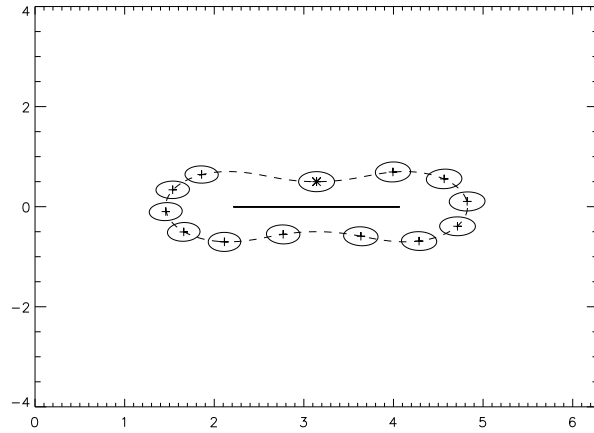
Figure 6.3: Circular vortex patch trajectory in a $2\pi$ periodic domain with a horizontal island (see figure 6.1). Here, $r_I = 0.5$ and $r = 1.855$, the patch has $\Gamma = 1.257$ and is initially located at $z = \pi + 0.5i$ (marked by the asterisk). The solid line represents the island, the dashed line the exact point vortex trajectory, and the $+$ marks the patch centroid.
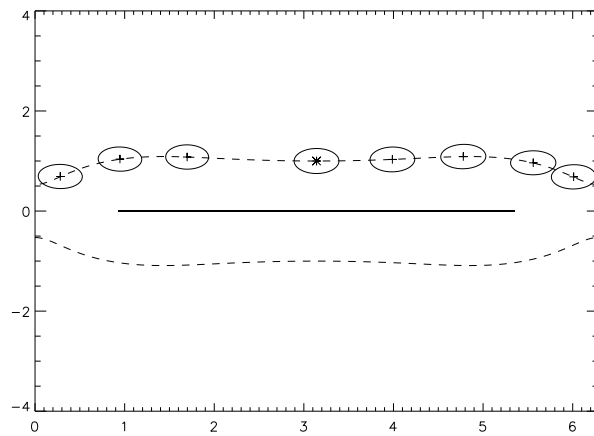


Figure 6.4: Circular vortex patch trajectory in a $2\pi$ periodic domain with a horizontal island (see figure 6.2). Here, $r_I = 2.0$ and $r = 4.429$, the patch has $\Gamma = 1.963$ and is initially located at $z = \pi + i$ (marked by the asterisk). The solid line represents the island, the dashed line the exact point vortex trajectory, and the $+$ marks the patch centroid.

bottom tip of the South American continent penetrates into the (periodic) Southern Ocean. To construct the appropriate mappings consider in the $\zeta$-domain exterior to the unit circle the series of mappings given by

$$\zeta_1(\zeta) = i\frac{\zeta - 1}{\zeta + 1}, \tag{6.22}$$

$$\zeta_2(\zeta_1) = \zeta_1^2, \tag{6.23}$$

$$\zeta_3(\zeta_2) = -(\zeta_2 + 1), \tag{6.24}$$

$$z(\zeta_3) = \frac{L}{2\pi i}\log\zeta_3, \tag{6.25}$$

where $L$ is the period of $\mathcal{D}_z$. The first of these maps takes the exterior of the unit $\zeta$-circle to the upper half of the $\zeta_1$-plane. The second map doubles the angle of the boundary along $\Re\zeta_2 < 0$, thus mapping the $\zeta_1$-domain to the domain exterior to the semi-infinite barrier along $\Re\zeta_2 > 0$. (6.24) then takes $\mathcal{D}_{\zeta_2}$ to the domain exterior to the barrier extending from $-\infty < \Re\zeta_3 < -1$. Finally, (6.25) takes $\mathcal{D}_{\zeta_3}$ to the periodic $z$-strip exterior to the semi-infinite barrier with $\Re z = \pi$ and complex coordinate extending from $-\infty < \Im z < 0$. The composition of the maps (6.22)-(6.23) can be written as

$$z(\zeta) = -i\log\left[\frac{-4\zeta}{(1 + \zeta)^2}\right]. \tag{6.26}$$

As in section 6.2, point vortex trajectories and the motion of a vortex patch are now computed. In computing point vortex trajectories the starting point is again the vortex Hamiltonian of a single point vortex within the unit circle $\rho$-domain. The

sequence of mappings to the $z$-plane is similar to the sequence given above, the difference being that the map from the interior of the unit circle to the upper half plane, given by

$$\zeta_1 = i\frac{1-\rho}{1+\rho},$$ (6.27)

replaces (6.22). Thus, (6.16) along with the sequence of maps given by (6.27), (6.23), (6.24) and (6.25) along with the transformation rule for the Hamiltonian (5.76) give

$$H^{(z)}(z_\alpha, \bar{z}_\alpha) = H^{(\rho)}(\alpha, \bar{\alpha}) + \frac{\Gamma^2}{4\pi}\log\left[\frac{a}{2\pi}\frac{1-\alpha}{\alpha(1+\alpha)}\right].$$ (6.28)

Point vortex trajectories are shown in figure 6.5 for the case when $L = 2\pi$. In a 'shell' around the barrier, vortex trajectories are similar to those seen in planar semi-infinite barrier case, that is, vortices move around a single barrier. Further away from the barrier, the influence of the periodicity plays a more predominant role in the motion and trajectories move around the surface of the unit cylinder (i.e. through the $2\pi$ periodic domain) whilst oscillating up and down, the maximum of the oscillation being directly above the plate.

An example of a vortex patch trajectory is shown in figure 6.6. The resolution parameter between patch boundary nodes is set to 0.01, $dt = 0.01$ and the sum in (6.8) is truncated at $k = N = 200$. Good agreement is seen between the point vortex and patch centroid trajectory except for a slight difference when the vortex is above the plate. This is however expected due to the finite size of the vortex patch.
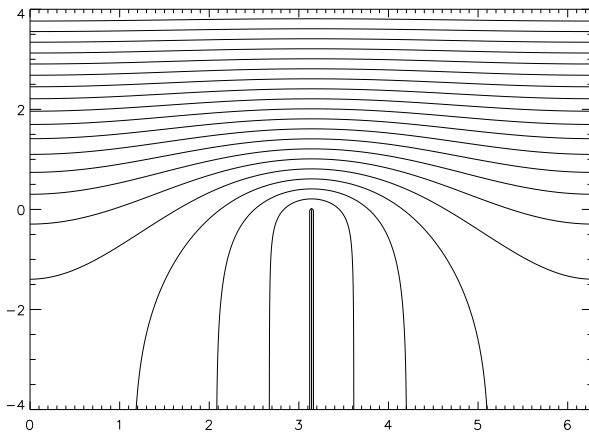
Figure 6.5: Point vortex trajectories in a $2\pi$ periodic domain containing a vertical semi-infinite barrier. Here, $L = 2\pi$.
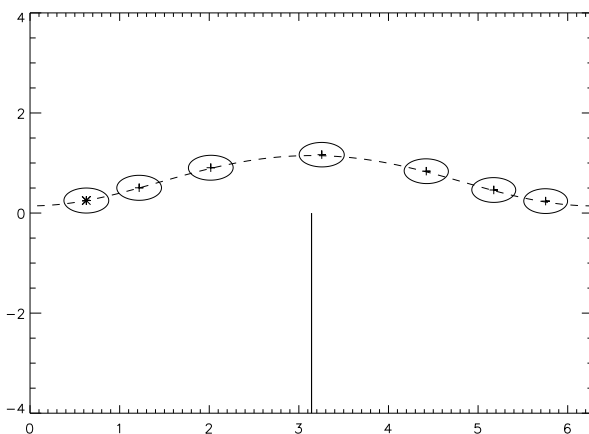


Figure 6.6: Circular vortex patch trajectory in a $2\pi$ periodic domain with a vertical semi infinite barrier. The patch has $\Gamma = 0.796$ and is initially located at $z = 1/5\pi + 1/4i$ (marked by the asterisk). The solid line represents the island, the dashed line the exact point vortex trajectory, and the + marks the patch centroid.

## 6.4   Summary

In this chapter, a method for computing the motion of vortices in periodic strips (or on the surface of the unit cylinder) with boundaries has been presented. The methods for computing these motions are similar to those presented in chapter 5. Here, two singly connected domains were considered, an array horizontal thin islands and an array of semi-infinite vertical barriers. Vortex trajectories close to the boundaries were, in both cases, similar to the planar cases involving a single vortex and an isolated boundary. Further away from the boundaries the periodicity of the configuration plays a predominant role in the dynamics.

Good agreement is seen between contour dynamics and point vortex trajectories in cases when the patch remains close to circular. Again, the principle of the method presented here can be extended to doubly connected periodic domains, using the methods of chapter 5.3, and potentially domains of a higher connectivity. Although, in such cases, the required mappings may not be as straightforward as for non-periodic cases in domains of a higher connectivity.

# Chapter 7

# Conclusions and future work

Analytical and numerical methods have been applied to a number of problems involving two dimensional, inviscid and incompressible flows with regions of constant vorticity. Broadly speaking, the work has considered three types of problem. In chapters 2 and 3 the shapes of equilibria for point vortices near a vorticity interface were found analytically in the linear limit of small amplitude interfacial waves and numerically for fully non-linear systems respectively. Chapter 4 considered the time-dependent problem of a vortex-wave interaction on the surface of the sphere and chapters 5 and 6 considered the motion of vortices in bounded domains on the surface of the sphere and in a $2\pi$-singly-periodic strip respectively.

For the systems considered in chapter 2 the vorticity was generated by a shear flow. The first system considered was the planar problem of two point vortices of opposite signed circulations either side of the vorticity interface, that is, the anti-symmetric analogue of that considered in McDonald (2004). In contrast to McDonald (2004) it was shown in the linear limit it is not possible to construct such an equilibrium. A

non-linear analogue of this equilibrium could also not be found.

A series of periodic configurations were then considered. The configurations included a periodic array of vortices located near an interface in the irrotational region of the flow, a periodic array of vortices located near an interface in the rotational region of the flow and an array of anti-symmetrically placed vortices of opposite signed circulation either side of the interface. A range of equilibria shapes were found for these configurations. When vortices were placed in the irrotational region of the flow there tended to be a peak in the interface placed directly above the point vortex. In contrast, when the vortices were placed in the rotational region of the flow the maximum height of the interface was in between the vortices and the minimum located above the vortices. For the anti-symmetric periodically placed vortex case, equilibrium shapes were found to be dominated by the primary mode, that is, they resembled a full sine wave per period. However, surprisingly, the interface tended to 'sink' towards vortices with a positive circulation and be 'pushed away' from vortices with a negative circulation. This behaviour is contrast to what is generally observed in many non-periodic systems.

In chapter 3 a combination of contour dynamics and Newtonian iteration was used to compute the corresponding non-linear equilibria to those found in chapter 2. Computational equilibria shapes generally agreed very well with those found in the linear limit. The computed equilibria were also shown to be robust by using them as initial conditions in a time dependent contour dynamics code. Small amplitude equilibria would remain largely unchanged over very long periods of time while larger amplitude equilibria in which much higher velocity fields were present would remain

relatively stationary for reasonable periods of time before slowly deforming.

In chapter 4 the time evolution of a system consisting of single point vortex on the surface of the unit sphere interacting with an initially flat vorticity interface was examined. A system of first order ODEs was derived in the linear limit of small amplitude waves at the interface. This system of ODEs was integrated numerically to examine the behaviour of the system. Further approximations yield analytical solutions governing the initial movements of the system. Such approximations also give insight into the stability of vortices located at the two poles. The main results predicted by linear theory indicate that a point vortex in a sea of same signed vorticity will initially move away from the vorticity interface whilst a vortex in a sea of opposite signed vorticity will move towards it. This result leads to the conclusion that a vortex placed at a pole in a sea of same signed vorticity is at a stable equilibrium and vice versa. This result is confirmed by an analytical, non-linear, stability analysis.

Evolution of the fully non-linear system is again explored using contour dynamics. In highly linear cases or over short time periods contour dynamics is in very good agreement with linear theory. Computations also show that 'intermediate' strength vortices exhibit a drift away from the interface when surrounded by a sea of same signed vorticity and towards the interface when surrounded by a sea of opposite signed vorticity. Intermediate is used here in the sense that the system cannot be described by linear theory over long periods of time but where the vortex is sufficiently strong to induce rapid contour wrapping. As discussed in Polvani and Dritschel (1993) this model is, to first order, relevant to studying the dynamics in Saturn's atmosphere and may provide a dynamical explanation behind the location of Saturn's polar storm

discovered in recent observations (Dyudina et al. 2009).

The final two chapters investigate the motion of vortices in domains with impenetrable boundaries. Vortex motion on the surface of the unit sphere is considered in chapter 5 and motion on the unit cylinder or, equivalently, $2\pi$-singly-periodic domain in chapter 6. The methodology employed in each chapter is similar. Contour dynamics algorithms formulated in their respective topographies are used to calculate the flow in the required domain as if boundaries are not present. Utilizing the invariance of Laplace's equation under conformal mapping, the boundary value problem is mapped to the exterior of the unit circle and an irrotational flow field found, such that, when added to that owing to the vortices in the absence of boundaries satisfies the boundary conditions in the original domain. The main difference in computing motion in the respective domains (apart from the different contour dynamics algorithm) is that the spherical problem is projected into the stereographic plane and requires careful consideration of the quantities conserved under projection while the periodic problem makes use of a log map to map the plane into the periodic domain.

On the sphere, vortex motion in a number of singly connected domains is presented. Further doubly connected examples of a barrier with two gaps are also presented. In cases where the vortex remained close to circular, the centroid of the patch followed the corresponding point vortex trajectories very closely. This is as expected as the velocity field exterior to a circular vortex patch is identical to that of a point vortex of same circulation. In cases where background flows were included and in the doubly connected case, some examples of vortex splitting were observed. In the periodic problems considered on the surface of the unit cylinder, patch centroid and

point vortex trajectories are again in very good agreement. An alternative procedure for computing the motion of vortices in domains of potentially arbitrary connectivity on a spherical shell is presented in Surana and Crowdy (2008).

An obvious problem to now consider is that of adapting the algorithm presented in chapters 5 and 6 to work in domains of higher connectivity. To do this, a method such as that discussed in Bird and Steele (1992) could be employed. Preliminary work to this end has already begun. It would also be desirable to have a 'contour surgery' algorithm working on the sphere and cylinder, thus allowing long time integration of systems in which vortex splitting phenomenon occur. Such an algorithm has already been completed but requires some 'fine tuning' to have it working correctly in all cases.

Other problems of interest include the vortex flushing problem and the motion of vortices in the presence of moving boundaries. An example of a vortex flushing problem is that, if a vortex in the open ocean passes by close to a bay, without actually entering the bay, what is the rate of mixing between the fluid in the bay with that of the open ocean? The central idea and challenge here is to compute the motion of irrotational (i.e. passive) fluid and to quantify the mixing between different regions. Literature on the aforementioned topics is currently sparse but both problems are of interest to oceanographers. Additionally, for certain problems such as the vortex flushing problem, an interesting exercise would be to compare results given by vortex dynamics to those obtained from a general circulation model such as ICOM. More 'direct' comparisons between fundamental and general circulation models could help clarify the interplay between various parameters in a general circulation models.

# Appendix A

# Implementation of spherical and cylindrical contour dynamics algorithms

Details on the implementation of a 2D contour dynamics algorithm are given in Dritschel (1989). Below, details on implementing contour dynamics algorithms on the surface of the unit sphere and on the surface of the unit cylinder with no boundaries present are outlined. The following is based on Dritschel (1989), while the actual construction of the associated numerical routines was done by the author.

## A.1   Spherical contour dynamics

In general, to follow the motion of a distribution of vorticity is it necessary to invert the Green's function in the domain in question and use the resulting velocity

field to advect the the fluid. The Green's function for the motion of an inviscid, incompressible fluid on the surface of the unit sphere is given by

$$G(\theta, \phi; \theta', \phi') = \frac{1}{4\pi} \log(1 - \cos \Theta), \tag{A.1}$$

where $\theta$ is the co-latitude, $\phi$ the longitude and $\cos \Theta = (\cos \theta \cos \theta' + \sin \theta \sin \theta' \cos(\phi - \phi')$ is the inner product of the Cartesian coordinate vectors $\mathbf{x} = (\sin \theta \cos \phi, \sin \theta \sin \phi, \cos \theta)$ and $\mathbf{x}' = (\sin \theta' \cos \phi', \sin \theta' \sin \phi', \cos \theta')$. On the surface of the sphere, the Gauss constraint requires that the vorticity $\omega$ satisfies

$$\int_0^{2\pi} \int_0^{\pi} \omega d\theta d\phi = 0. \tag{A.2}$$

The constraint (A.2) is built into (A.1) and the streamfunction is therefore given by

$$\psi(\theta, \phi) = \frac{1}{4\pi} \int \int \omega(\theta', \phi') \log(1 - \cos \Theta) d\Omega', \tag{A.3}$$

where $d\Omega' = \sin \theta' d\theta' d\phi'$ is the incremental solid angle area.

The equations of contour dynamics will now be formulated for a single piecewise constant patch of vorticity whose boundary is denoted $\mathcal{C}$. Identical equations can then be applied to any additional distributions of vorticity within the domain. Whilst traversing the contour $\mathcal{C}$ in the anti-clockwise direction, label the change in vorticity between the left hand and right hand sides of the contour by $\tilde{\omega}$.

The azimuthal and longitudinal velocities in spherical polar coordinate can be written as

$$\frac{d\theta}{dt} = u_\theta = -\frac{1}{\sin \theta} \frac{\partial \psi}{\partial \phi}, \tag{A.4a}$$

$$\sin \theta \frac{d\phi}{d\theta} = u_\phi = \frac{\partial \psi}{\partial \theta}. \tag{A.4b}$$

Substitution of (A.3) in (A.4a) and using Green's theorem gives

$$u_\theta = -\frac{\tilde{\omega}}{4\pi} \int_{\mathcal{C}} \log(1 - \cos\Theta) \sin\theta' d\theta'. \tag{A.5}$$

Now, instead of deriving a similar equation for $u_\phi$, consider the following. In terms of Cartesian coordinates, $|\mathbf{x}| = 1$ and $|\mathbf{x}'| = 1$ giving $1 - \cos\Theta = \frac{1}{2}|\mathbf{x} - \mathbf{x}'|^2$. Then, noting that $-\sin\theta d\theta = dz$, (A.5) can be written as

$$\frac{dz}{dt} = -\frac{\tilde{\omega}}{2\pi} = \int_{\mathcal{C}} \log|\mathbf{x} - \mathbf{x}'| dz'. \tag{A.6}$$

Thus, by symmetry, the three Cartesian velocities must be given by

$$\frac{d\mathbf{x}}{dt} = -\frac{\tilde{\omega}}{2\pi} = \int_{\mathcal{C}} \log|\mathbf{x} - \mathbf{x}'| d\mathbf{x}'. \tag{A.7}$$

The contour $\mathcal{C}$ is represented as a number of discrete nodes where interpolation between nodes takes the form of a cubic spline. The shape of the contour between adjacent nodes, say $i$ and $i + 1$, can be written as

$$\mathbf{x}(p) = \mathbf{x}_i + p\mathbf{t}_i + \eta(p)\mathbf{n}_i + \zeta(p)\mathbf{s}_i, \tag{A.8a}$$

$$\mathbf{t}_i = \mathbf{x}_{i+1} - \mathbf{x}_i, \tag{A.8b}$$

$$\mathbf{n}_i = \mathbf{x}_i \times \mathbf{x}_{i+1}, \tag{A.8c}$$

$$\mathbf{s}_i = (\mathbf{x}_i + \mathbf{x}_{i+1})/2, \tag{A.8d}$$

$$\eta(p) = \alpha_i p + \beta_i p^2 + \gamma_i p^3, \tag{A.8e}$$

$$\zeta(p) = \frac{1}{2}e_i^2 p(1-p), \tag{A.8f}$$

where $0 \leq p \leq 1$ is the fractional distance between the nodes and $e_i = |t_i| = (dx_i^2 + dy_i^2 + dz_i^2)^{\frac{1}{2}}$. The coefficients $\alpha_i$, $\beta_i$ and $\gamma_i$ are calculated according to

$$\alpha_i = -\frac{1}{3}e_i k_i - \frac{1}{6}e_i k_{i+1}, \tag{A.9a}$$

$$\beta_i = -\frac{1}{2}e_i k_i, \tag{A.9b}$$

$$\gamma_i = \frac{1}{6}e_i(k_{i+1} - k_i), \tag{A.9c}$$

where $k_i$ is the curvature at the $i$th node and is given explicitly by

$$k_i = \frac{2\mathbf{x}_i \cdot (\mathbf{t}_i \times \mathbf{t}_{i-1})}{|\mathbf{t}_i e_{i-1}^2 + \mathbf{t}_{i-1}e_i^2|}. \tag{A.10}$$

Additionally, using (A.10) the local density of nodes then takes the form

$$\rho_i = (\mu)^{-1}(1 + k_i)^{\frac{a}{2}}, \tag{A.11}$$

where $\mu$ is a small non-dimensional number and $a$ is the resolution parameter between nodes. The resolution parameter $a$ controls how sharply the local node density $\rho_i$ increases with curvature $k_i$.

Substituting (A.8a) into (A.7) the velocity field $\mathbf{u} = d\mathbf{x}/dt$ at a point $\mathbf{x}$ can be represented as the the sum of contributions to the velocity field from contour segments ($\Delta\mathbf{u}_i$) adjoining all adjacent nodes, that is

$$\mathbf{u} = \frac{1}{2\pi}\sum_i \tilde{\omega}\Delta\mathbf{u}_i, \tag{A.12}$$

where, to first order (supressing the subscript $i$)

$$\Delta\mathbf{u} = T\mathbf{t} + N\mathbf{n} + S\mathbf{s},$$

$$T = 1 - dr - (1 - d)r' - \hat{c}^2 h_0 + c(\alpha h_1 + \beta h_2 + \gamma h_3) + b(h_1 - h_2),$$

$$N = \alpha q_1 + \beta q_2 + \gamma q_3, \qquad S = \frac{1}{2}e^2(q_1 - q_2), \qquad a = |\mathbf{x} - \mathbf{x}_i|^2/e^2,$$

$$b = \frac{1}{2}\mathbf{s}\cdot(\mathbf{x} - \mathbf{x}_i), \qquad c = \frac{\mathbf{n}\cdot(\mathbf{x} - \mathbf{x}_i)}{e^2}, \qquad d = \frac{\mathbf{t}\cdot(\mathbf{x} - \mathbf{x}_i)}{e^2}, \tag{A.13}$$

$$\hat{c} = \frac{|\mathbf{t}\times(\mathbf{x} - \mathbf{x}_i)|}{e^2}, \qquad e = |\mathbf{t}|, \qquad h_0 = \frac{1}{\hat{c}}\left[\tan^{-1}\left(\frac{1-d}{\hat{c}}\right) + \tan^{-1}\left(\frac{d}{\hat{c}}\right)\right],$$

$$h_1 = r' - r + dh_0, \qquad h_n = \frac{1}{n-1} + 2dh_{n-1} - ah_{n-2} \qquad (n > 1),$$

$$q_n = h_{n+1} - dh_n, \qquad r = \log|\mathbf{x} - \mathbf{x}_i|, \qquad r' = \log|\mathbf{x} - \mathbf{x}_{i+1}|.$$

In principle, analytical equations for higher order terms can also be derived but this turns out to be unnecessary as contributions from higher order terms are of a similar magnitude to the errors arising from interpolation (Dritschel 1989).

Finally, if $d > a$ (corresponding to when the evaluation point, projected onto the plane perpendicular to $\mathbf{s}_i$, lies within the circle in the plane whose diameter connects

$\mathbf{x}_i$ with $\mathbf{x}_{i+1}$) the following modifications to (A.13) are required

$$a = |\mathbf{x} - \mathbf{x}_i|^2/e^2 - \eta(d)[2c - \eta(d)],$$

$$c = \frac{\mathbf{n} \cdot (\mathbf{x} - \mathbf{x}_i)}{e^2} - \eta(d), \tag{A.14}$$

$$T = 1 - dr - (1 - d)r' - \hat{c}^2 h_0 + c(\alpha h_1 + \beta h_2 + \gamma h_3) + b(h_1 - h_2) - ch_0\eta(d),$$

where

$$\eta(d) = \alpha_i d + \beta_i d^2 + \gamma_i d^3 \quad (0 < d < 1). \tag{A.15}$$

These adjustments are required as the assumptions made in evaluating (A.13) no longer hold for evaluation points sufficiently close to the node over which integration is taking place (Dritschel 1989). Details on the redistribution of nodes are presented in Dritschel (1989) and this redistribution closely mirrors that of the planar case (with the 2D Cartesian vectors replaced by 3D vectors). Additionally, following each time step nodes are restricted to the surface of the sphere through a radial adjustment and insisting $|\mathbf{x}_i| = 1$.

To verify the routine presented above, velocity fields given by the contour dynamics code were tested qualitatively against exact solutions for spherical cap distributions and velocity fields exterior to a vorticity distribution were also tested against those owing to point vortices at arbitrary locations on the sphere. In all cases excellent agreement was seen.

## A.2 Cylindrical or singly periodic contour dynamics

The adjustments required to the spherical algorithm presented in A.1 in order to compute the motion of vortices on the surface of the unit cylinder are now discussed. Let $z$ be the vertical coordinate on the cylinder and $\phi$ be the azimuthal angle such that $x = \cos\phi$ and $y = \sin\phi$. Laplace's equation takes the form

$$\nabla^2\psi = \frac{\partial^2\psi}{\partial\phi^2} + \frac{\partial^2\psi}{\partial z^2} = \omega(\phi, z), \qquad (A.16)$$

which has the same form as for a planar flow, expect the $\phi$ coordinate is now periodic. The Green's function takes the form (Lamb 1932)

$$G(\phi, z; \phi', z') = \frac{1}{4\pi}\log\{4\sin^2[(\phi - \phi')/2] + 4\sinh^2[(z - z')/2]\}, \qquad (A.17)$$

so that the azimuthal and vertical velocities can be written as

$$\frac{d\phi}{dt} = -\tilde{\omega}\int_{\mathcal{C}} G(\phi, z; \phi', z')d\phi', \qquad (A.18a)$$

$$\frac{dz}{dt} = -\tilde{\omega}\int_{\mathcal{C}} G(\phi, z; \phi', z')dz', \qquad (A.18b)$$

where $\tilde{\omega}$ is the vorticity of the region of fluid whose boundary is the contour $\mathcal{C}$. The equations of contour dynamics will again be formulated for a single region of vorticity on the surface of the cylinder. Additional regions of vorticity are easily taken into account through summing the velocity field contributions owing to each vorticity contour. Also, note that, using (A.17) the streamfunction for a point vortex

of circulation $\Gamma$ on the surface of the unit cylinder can be written as

$$\psi_{\mathrm{pv}} = \int \int \Gamma \delta(\phi - \phi_{\mathrm{pv}}, z - z_{\mathrm{pv}}) dz d\phi$$

(A.19)

$$= \frac{\Gamma}{4\pi} \log\{4\sin^2[(\phi - \phi_{\mathrm{pv}})/2] + 4\sinh^2[(z - z_{\mathrm{pv}})/2]\}.$$

This result is used in chapters 2 and 3.

To avoid the problem of $\phi$ jumping discontinuously the contour dynamics equations are formulated in terms of the Cartesian velocities along the $x$ and $y$ coordinates. These velocities are related to the azimuthal velocity $\Omega = d\phi/dt$ through

$$\frac{dx}{dt} = \frac{d\cos\phi}{dt} = -\sin\phi\frac{d\phi}{dt} = -y\Omega,$$

(A.20a)

$$\frac{dy}{dt} = x\Omega.$$

(A.20b)

The differential angle needed for the evaluation of $\Omega$ is given by $d\phi' = x'dy - y'dx'$ and in terms of Cartesian coordinates the Green's function (A.17) can be written as

$$G(\mathbf{x}; \mathbf{x}') = -\frac{1}{4\pi} \log[|\mathbf{x} - \mathbf{x}'|^2 + H(z - z')],$$

(A.21)

where $H(\zeta) = \exp(\zeta) + \exp(-\zeta) - 2 - \zeta^2$. When $|\mathbf{x} - \mathbf{x}'|^2$ is small, $H(z - z')$ is far smaller as $H(\zeta) = \frac{1}{12}\zeta^4 + \mathcal{O}(\zeta^6)$ for small $\zeta$. The Green's function (A.21) can thus be split into parts

$$G_a = -\frac{1}{4\pi} \log|\mathbf{x} - \mathbf{x}'|^2,$$

(A.22a)

$$G_b = -\frac{1}{4\pi} \log\left[1 + \frac{H(z - z')}{|\mathbf{x} - \mathbf{x}'|^2}\right],$$

(A.22b)

to ensure the Green's function is well behaved for small $|\mathbf{x} - \mathbf{x}'|^2$. Integrals involving $G_a$ can then be integrated explicitly to obtain equations similar to those for the sphere (A.13). Denote the velocity owing to this singular part of the Green's function $\mathbf{u}_a$. Integrals involving $G_b$ are evaluated using numerical quadrature and denote the velocity field owing to this non-singular part of the Green's function $\mathbf{u}_b$.

As mentioned above, the explicit velocity field owing to integrals involving $G_a$ yields very similar results to (A.13). The required modifications to the spherical algorithm are detailed below. For the shape of the contour between adjacent nodes, some minor modifications are required. In (A.8) $\mathbf{s}_i = (\frac{1}{2}(x_i + x_{i+1}), \frac{1}{2}(y_i + y_{i+1}), 0)$ replaces (A.8d) (i.e. the $z$-component is set to zero owing to the lack of curvature in the $z$-direction), $\mathbf{n}_i = \mathbf{s}_i \times \mathbf{t}_i$ replaces (A.8c) and $\hat{e}_i^2 = dx_i^2 + dy_i^2$ is used in place of $e_i^2$ in (A.8f) only. Similarly, $\hat{\mathbf{x}}_i = (x_i, y_i, 0)$ replaces $\mathbf{x}_i = (x_i, y_i, z_i)$ in (A.10).

Substituting the modified version of (A.8) into (A.18) and noting that $dz'/dp = dz_i + (d\eta/dp)n_{zi}$ and $d\phi'/dp = n_{zi} - (d\eta/dp)dz_i + [\zeta - (p - \frac{1}{2})d\zeta/dp]n_{zi}$ (to first order in $\eta$ and $\zeta$), the singular part of the Green's function $G_a$ yields

$$\Omega_a = \frac{1}{2\pi} \sum_i \omega_i[(T_i + S_i)n_{zi} - N_i dz_i], \tag{A.23a}$$

$$w_a = \frac{1}{2\pi} \sum_i \omega_i[T_i dz_i + N_i n_{zi}], \tag{A.23b}$$

where $u = -y\Omega$ and $v = x\Omega$. $T_i$ and $N_i$ in (A.23) have the same form as in (A.13) and $S_i$ is modified to

$$S_i = \frac{1}{4}\hat{e}^2(q_1 - q_2 + \frac{2}{3}q_3). \tag{A.24}$$

It now remains to determine $\mathbf{u}_b$, the velocity field owing to the non-singular part of the Green's function, $G_b$. $\Omega_b$ and $w_b$ can be evaluated using three-point Gaussian

quadrature,

$$\Omega_b = \frac{1}{2\pi} \sum_i \omega_i \sum_{l=1}^{3} \sigma_l G_b(\mathbf{x}; \mathbf{x}'(p_l)) \frac{d\phi'}{dp}(p_l), \qquad (A.25a)$$

$$w_a = \frac{1}{2\pi} \sum_i \omega_i \sum_{l=1}^{3} \sigma_l G_b(\mathbf{x}; \mathbf{x}'(p_l)) \frac{dz'}{dp}(p_l), \qquad (A.25b)$$

where $p_1 = 0.112701665379...$, $p_2 = 0.5$ and $p_3 = 1 - p_1$, $\sigma_1 = 5/18$, $\sigma_2 = 8/18$ and $\sigma_3 = \sigma_1$ (Abramowitz and Stegun 1965). The total velocity field is then given by

$$\mathbf{u} = \mathbf{u}_a + \mathbf{u}_b. \qquad (A.26)$$

Similar to in the spherical case, nodes tend to displace slightly from the cylinder due to numerical errors and thus following time step the $x$ and $y$ coordinates at each node are rescaled such that $x_i^2 + y_i^2 = 1$. Again, to verify the algorithm, quantitative tests in which velocity fields exterior to small patches were tested against those owing to point vortices were carried out. Excellent agreement was seen.

# Appendix B

# The generation of potential vorticity gradients by step topography

For simplicity, consider the motion of a 2D, homogeneous, inviscid fluid governed by the shallow water equations

$$\frac{D\mathbf{u}}{Dt} = -\nabla p, \tag{B.1a}$$

$$\frac{\partial H}{\partial t} + \nabla \cdot (H\mathbf{u}) = 0, \tag{B.1b}$$

where $\mathbf{u} = (u, v)$ are the horizontal velocity components, the material derivate is given by $D/Dt = \partial_t + \mathbf{u} \cdot \nabla$ and $p$ is the pressure owing to the change in depth $H = h - h_B$ where $h$ is the fluid surface height and $h_B$ is the height at the fluid base. Note that $(B.1a)$ and $(B.1b)$ represent the shallow water equations in a non-rotating frame and thus the effect of the Earth's rotation has been neglected. A more complete treatment

of the shallow water equations (with rotation included) is given in Pedlosky (1987). The vertical component of vorticity is given by

$$\omega = (\nabla \times \mathbf{u}) \cdot \mathbf{k} = u_x - u_y.$$  (B.2)

Taking the curl of (B.1a) gives

$$\omega_t + \mathbf{u} \cdot \nabla \omega + \omega \nabla \cdot \mathbf{u} = 0,$$  (B.3)

and, from using (B.1b)

$$\frac{Dq}{Dt} = 0,$$  (B.4)

where $q = \omega/H$ is the potential vorticity. The potential vorticity $q$ associated with each fluid parcel is thus a constant of the motion, i.e. if a fluid particle moves from deep to shallow water, its vorticity must decrease.

# Bibliography

Abramowitz, M. and I. A. Stegun, 1965: *Handbook of Mathematical Functions*. Dover, New York.

Acheson, D. J., 1990: *Elementary Fluid Dynamics*. Oxford University Press.

Aref, H., 2007: Vortices and polynomials. *Fluid Dynamics Research*, **39**, 5–23.

Aref, H., P. K. Newton, M. A, Stremler, T. Tokieda, and D. L. Vainchtein, 2003: Vortex Crystals. *Advances in Appl. Mech.*, **39**, 1–79.

Armi, L., D. Hebert, N. Oakey, J. F. Price, P. L. Richardson, H. T. Rossby, and B. Ruddick, 1989: Two years in the life of a Mediterranean salt lens. *J. Phys. Oceanogr.*, **19**, 354.

Atassi, O. V., 1998: Analytical and numerical study of the nonlinear interaction between a point vortex and a wall-bounded shear layer. *J. Fluid Mech.*, **373**, 155–192.

B A Smith, t., 1982: A new look at the Saturn system: the Voyager 2 images. *Science*, **215**, 504–537.

Bell, G. I., 1990: Interaction between vortices and waves in a simple model of geophysical flow. *Phys. Fluids A*, **2**, 575–585.

Bird, M. D. and C. R. Steele, 1992: A Solution Procedure for Laplace's Equation on Multiply Connected Circular Domains. *J. Appl. Mech.*, **59**, 398.

Crowdy, D., 1999: A class of exact multipolar vortices. *Phys. Fluids*, **11**, 2556–2564.

— 2002a: Exact solutions for rotating vortex arrays with finite-area cores. *J. Fluid Mech.*, **469**, 209–235.

— 2002b: The construction of exact multipolar equilibria of the two-dimensional Euler equations. *Phys. Fluids*, **14**, 257–267.

— 2006: Point vortex motion on the surface of a sphere with impenetrable boundaries. *Phys. Fluids*, **18**, 036602.

Crowdy, D. and M. Cloke, 2003: Analytical solutions for distributed multipolar vortex equilibria on a sphere. *Phys. Fluids*, **15**, 22–34.

Crowdy, D. and J. Marshall, 2004: Growing vortex patches. *Phys. Fluids*, **16**, 3122.

Crowdy, D. and A. Surana, 2008: Contour dynamics in complex domains. *J. Fluid Mech.*, **593**, 235–254.

Crowdy, D. G. and J. S. Marshall, 2005: The motion of a point vortex around multiple circular islands. *Phys. Fluids*, **17**.

— 2006: The motion of a point vortex through gaps in walls. *J. Fluid Mech.*, **551**, 31–48.

Deem, G. S. and N. J. Zabusky, 1978: 'V-states', interactions, recurrence and breaking. *Phys. Rev. Lett.*, **40**, 859–862.

DeFelice, T. P., J. D. Meyer, G. Xian, J. Christopherson, and R. F. Cahalan, 2000: Landsat 7 reveals more than just surface features in remote areas of the globe. *Bull. Amer. Meteor. Soc.*, **81**, 1047–1049.

Domm, U., 1956: Über die Wirbelstaßen von geringster Instabilität. *Zeitschrift für Angewandte Mathematik und Mechanik*, **36**, 367–371.

Dritschel, D. G., 1988: Contour dynamics/surgery on the sphere. *J. Comput. Phys.*, **79**, 477–483.

— 1989: Contour dynamics and contour surgery: Numerical algorithms for extended, high-Resolution modelling of vortex dynamics in two-dimensional, inviscid, incompressible flows. *Computer Physics Reports*, **10**, 77–146.

Dritschel, D. G. and L. M. Polvani, 1992: The roll-up of vorticity strips on the surface of a sphere. *J. Fluid Mech.*, **234**, 47–69.

Dunn, D. C., N. R. McDonald, and E. R. Johnson, 2001: The motion of a singular vortex near an escarpment. *J. Fluid Mech.*, **448**, 335–365.

Dyudina, U. A., A. P. Ingersoll, S. P. Ewald, A. R. Vasavada, R. A. West, K. H. Baines, T. W. Momary, A. D. D. Geino, J. M. Barbara, C. C. Porco, R. K. Achterberg, F. M. Flasar, A. A. Simon-Miller, and L. N. Fletcher, 2009: Saturn's south polar vortex compared to other large vortices in the Solar System. *Icarus*, **202**, 240–248.

Fratantoni, D., W. Johns, and T. Townsend, 1995: Rings of the North Brazil Current. *J. Geophys. Res.*, **100**, 10633–10654.

Gascard, J. C., A. J. Watson, M. Messias, K. A. Olsson, T. Johannessen, and K. Simonsen, 2002: Long-lived vortices as a mode of deep ventilation in the Greenland Sea. *Nature*, **416**, 525–527.

Gradshteyn, I. S. and I. M. Ryzhik, 1965: *Table of integrals series and products*. Academic Press, New York and London.

Hughes, T. J. R., 2003: *The Finite Element Method*. Dover Publications Inc.

Johnson, E. R. and N. R. McDonald, 2004a: The motion of a vortex near a gap in a wall. *Phys. Fluids*, **16**, 462–469.

— 2004b: The motion of a vortex near two circular cylinders. *Proc. R. Soc. Lond. A*, **460**, 939–954.

— 2005: Vortices near barriers with multiple gaps. *J. Fluid Mech.*, **531**, 335–358.

Juckes, M. N. and M. E. McIntyre, 1987: A high-resolution one-layer model of breaking planetary waves in the stratosphere. *Nature*, **328**, 590.

Kelvin, L., 1878: Floating magnets (illustrating vortex systems). *Collected works*, **IV**, 135–40.

Kidambi, R. and P. K. Newton, 2000: Point vortex motion on a sphere with solid boundaries. *Phys. Fluids*, **12**, 581–588.

Lamb, H., 1932: Hydrodynamics. *Cambridge Univ. Press.*.

McDonald, N. R., 1998: The motion of an intense vortex near topography. *J. Fluid Mech.*, **367**, 359–377.

— 2002: Steady, nonradiating geophysical flow past a cylinder with circulation. *Phys. Fluids*, **14**, 3018–3027.

— 2004: A new translating quasigeostrophic V-state. *European Journal of Mechanics B/Fluids*, **23**, 633–644.

— 2008: Vortex equilibria in flow past a plate. *ANZIAM J.*, **49**, 347–359.

McWilliams, J. C., 1985: Submeoscale, coherent vortices in the ocean. *Rev. Geophys.*, **23**, 165–182.

Meleshko, V. V. and G. J. F. V. Heijst, 1994: On Chaplygin's investigations of two-dimensional vortex structures in an inviscid fluid. *J. Fluid Mech.*, **272**, 157–182.

Nelson, R. B. and N. R. McDonald, 2009a: Finite area vortex motion on a sphere with impenetrable boundaries. *Phys. Fluids*, **21**, 016602.

— 2009b: Vortex motion on a sphere: barrier with two gaps. *Theor Comp Fluid Dyn*.

Newton, P. K. and T. Sakajo, 2007: The $N$-vortex problem on a rotating sphere. III. Ring configurations coupled to a background flow. *Proc. R. Soc. A*, **463**, 961–977.

Nof, D., 1995: Choked flows from the Pacific to the Indian Ocean. *J. Phys. Oceanogr.*, **25**, 1369–1383.

Pedlosky, J., 1987: *Geophysical Fluid Dynamics*. Springer.

— 1994: Stratified abyssal flow in the presence of fractured ridges. *J. Phys. Oceanogr.*, **30**, 403–417.

Pierrehumbert, R. T., 1980: A family of steady, translating vortex pairs with distributed vorticity. *J. Fluid Mech.*, **99**, 129–144.

Polvani, L. M. and D. G. Dritschel, 1993: Wave and vortex dynamics on the surface of a sphere. *J. Fluid Mech.*, **225**, 35–64.

Saffman, P. G., 1992: *Vortex Dynamics*. Cambridge University Press, Cambridge.

Scullen, D. and E. O. Tuck, 1995: Nonlinear free-surface flow computations for submerged cylinders. *J. Ship Res.*, **39**, 185.

Sheremet, V. A., 2001: Hysteresis of a western boundary current leaping across a gap. *J. Phys. Oceanogr.*, **31**, 1247–1259.

Smith, G. D., 1985: *Numerical Solution of Partial Differential Equations: Finite Difference Methods*. Clarendon Press.

Stern, M. E. and G. R. Flierl, 1987: On the interaction of a vortex with a shear flow. *J. Geophys. Res.*, **92**, 10,733–10,744.

Surana, A. and D. Crowdy, 2008: Vortex dynamics in complex domains on a spherical surface. *Journal of Computational Physics*, **227**, 6058–6070.

Thomson, J. J., 1883: A treatise on the motion of vortex rings. *Macmillan*.

Versteeg, H. and W. Malalasekra, 1995: *An Introduction to Computational Fluid Dynamics: The Finite Volume Method*. Prentice Hall.

von Karman, T. and H. L. Rubach, 1913: Uber den Mechanismus des Flussigkeitsund Luftwidertands. *Phys. Z*, **13**, 49–59.

Webster, R., 2006: Stability of Navier-Stokes discretizations on collocated meshes of high anisotropy and the performance of algebraic multigrid solvers. *Int. J. Numer. Meth. Fluids*, **51**, 14191438.

White, A. J. and N. R. McDonald, 2004: The Motion of a Point Vortex near Large-Amplitude Topography in a Two-Layer Fluid. *J. Phys. Oceanogr.*, **34**, 2808–2824.

Wu, H. M., E. A. Overman, and E. A. Zabusky, 1984: Steady state solutions of the Euler equations in two dimensions. Rotating and translating V-states with limiting cases. *J. Comput. Phys.*, **53**, 42–71.